

**X-RAY ABSORPTION SPECTROSCOPY AS A TOOL FOR CHARACTERIZING
SULFUR BASED REACTIVE INTERMEDIATES**

by

VLAD MARTIN-DIACONESCU

B.Sc., The University of British Columbia, 2003

**A THESIS SUBMITTED IN PARTIAL FULFILLMENT OF
THE REQUIREMENTS FOR THE DEGREE OF
DOCTOR OF PHILOSOPHY**

in

**THE FACULTY OF GRADUATE STUDIES
(Chemistry)**

**THE UNIVERSITY OF BRITISH COLUMBIA
(Vancouver)**

August 2009

© Vlad Martin-Diaconescu, 2009

Abstract

Sulfur K-edge X-ray absorption spectroscopy (XAS) has proven to be a great tool for the investigation of sulfur oxidation states and sulfur-metal ligand bonding. In this thesis, XAS has been applied in the detection and characterization of sulfur-based reactive intermediates and products of photo-reacted sulfur species, with applications in both bioinorganic and inorganic chemistry.

Low molecular weight thiols and their derivatives have important protein modulation, signal transduction and antioxidant activities. This includes glutathione (GSH), nitrosogluthathione (GSNO), and lipoic acid (LA), which are involved in complex redox pathways resulting in a variety of intermediates and products that can be difficult to characterize. These compounds have been used as models for thiol nitrosation and oxidation reactions, and their reactivity was probed with sulfur K-edge XAS, which has been developed into a valuable tool for the investigation of sulfur-containing radical species and related non-radical intermediates.

XAS was also applied to investigate the reactivity of p-toluene sulfonyl chloride, an initiator in metal catalyzed living radical polymerization, to explore the effect of hyperconjugation on the reactivity of the S-Cl bond. A series of model compounds of the form RSO_2G ($\text{G} = -\text{Cl}, -\text{OH}, -\text{alkyl}$) were used to evaluate the effect of aryl versus alkyl R groups on the photo-reactivity and orbital mixing of the S-G bond.

Table of Contents

Abstract	ii
Table of Contents.....	iii
List of Tables.....	v
List of Figures	vi
List of Schemes	ix
List of Equations.....	x
List of Abbreviations	xi
Acknowledgements	xli
Chapter 1: X-ray Absorption Spectroscopy (XAS).....	1
1.1 The Synchrotron Light Source (X-ray Source)	1
1.2 Sulfur K-edge X-ray Absorption Spectroscopy.....	4
1.3 Applications of XAS	7
1.4 Thesis Overview	9
Chapter 2: Implications of Thiol Oxidation	10
2.1 Low Molecular Weight Sulfur Species <i>In Vivo</i>	10
2.2 Mechanism and Control of Thiol Oxidation	13
2.3 Experimental Rationale.....	18
Chapter 3: Experimental Section.....	21
3.1 X-ray Absorption Spectroscopy (XAS).....	21
3.2 Density Functional Calculations	24
3.3 Nuclear Magnetic Resonance Spectroscopy (NMR).....	25
3.4 Electron Paramagnetic Resonance Spectroscopy (EPR)	25
3.5 Materials	26
Chapter 4: Sulfur K-edge XAS as a Probe of Sulfur Centered Radical Intermediates	27
4.1 Background.....	27
4.2 Results and Discussion.....	28
4.3 Conclusion	37
Chapter 5: Perthiyl Radical and Disulfide Bond Formation in Photo-irradiated Nitrosoglutathione and Lipoic Acid.....	38
5.1 Background.....	38
5.2 Results and Discussion.....	43

5.3 Conclusion	54
Chapter 6: Effects of Hyperconjugation on the Electronic Structure and Photo-reactivity of Organic Sulfonyl Chlorides	55
6.1 Background.....	55
6.2 Results.....	58
6.3 Discussion	71
6.4 Conclusion	74
Chapter 7: Concluding Remarks and Outlook.....	77
References	80
Appendix 1 ADF Input Files	88

List of Tables

Table 2.1.1 Biologically important low molecular weight sulfur species	11
Table 4.2.1 Principal component analysis of UV irradiated GSH XAS spectra	31
Table 4.2.2 TD-DFT calculated sulfur K-edge bound transitions for thiyl and perthiyl radicals	36
Table 5.2.1 Half power saturation values for the EPR of LA	45
Table 6.2.1 TD-DFT and Δ SCF of p-toluene sulfonyl chloride	66
Table 6.2.2 TD-DFT and Δ SCF of methane sulfonyl chloride	66
Table 6.2.3 TD-DFT and Δ SCF of p-toluene sulfonic acid	67
Table 6.2.4 TD-DFT and Δ SCF of methane sulfonate	67
Table 6.2.5 TD-DFT and Δ SCF of ethyl phenyl sulfone	68
Table 6.2.6 TD-DFT and Δ SCF of methionine sulfone	68

List of Figures

Figure 1.1.1 Schematic diagram of the main components found in a synchrotron	2
Figure 1.1.2 Schematic diagram of the main components found in a beamline.....	4
Figure 1.2.1 XAS model spectra of possible S_{1s} transitions	5
Figure 1.3.1 XAS fingerprint spectra of varying sulfur oxidation states	7
Figure 2.1.1 Thiol oxidation and cell life cycle.....	10
Figure 2.2.1 Thiol oxidation pathways.....	15
Figure 2.2.2 Reduction pathways of oxidized sulfur species.....	17
Figure 3.1.1 XAS experimental setup at SSRL beamline 6-2	23
Figure 4.2.1 X-band EPR of UV irradiated glutathione.....	29
Figure 4.2.2 Power saturation study of UV irradiated glutathione	30
Figure 4.2.3 Sulfur K-edge XAS of UV irradiated GSH	32
Figure 4.2.4 Difference XAS spectra of UV irradiated GSH	33
Figure 4.2.5 Time evolution of features at 2468.8eV and 2470.5eV in UV irradiated GSH	34
Figure 4.2.6 DFT density contour maps of thiyl and perthiyl radicals.....	35
Figure 4.2.7 Peak fitting of XAS features due to thiyl and perthiyl radicals	37

Figure 5.1.1 GSNO sulfur K-edge XAS spectrum	40
Figure 5.1.2 DFT density contour maps of $\text{CH}_3\text{CH}_2\text{SNO}$	40
Figure 5.1.3 LA sulfur K-edge XAS spectrum	42
Figure 5.2.1 LA sulfur K-edge XAS spectra under photo-irradiation	43
Figure 5.2.2 EPR spectra of irradiated LA	45
Figure 5.2.3 EPR power saturation spectra of irradiated LA	46
Figure 5.2.4 GSNO sulfur K-edge XAS spectra under photo-irradiation	48
Figure 5.2.5 Time evolution of features at 2470.2 and 2471.6 in irradiated GSNO.....	49
Figure 5.2.6 EPR spectra of irradiated GSNO	51
Figure 5.2.7 NMR of irradiated GSNO and GSSG	52
Figure 5.2.8 EPR spectra of irradiated GSSG	53
Figure 5.2.9 EPR power saturation study of irradiated GSSG	54
Figure 6.2.1 Structure of sulfonyl model compounds	59
Figure 6.2.2 Geometries of ethyl phenyl sulfone used for TD-DFT	60
Figure 6.2.3 XAS and simulated spectra of sulfonyl chlorides	61
Figure 6.2.4 XAS and simulated spectra of sulfonates	62

Figure 6.2.5 XAS and simulated spectra of sulfones	63
Figure 6.2.6 Molecular orbitals of benzene	65
Figure 6.2.7 Time evolution of the sulfur K-edge features due to the S-Cl bond with in-situ irradiation	69
Figure 6.2.8 XAS with <i>in situ</i> irradiation of sulfonyl chlorides	70
Figure 6.3.1 Mixing of $\Phi^4_{\pi^*}$ and $\Phi^5_{\pi^*}$ into SCl_{σ^*}	72
Figure 6.3.2 Effect of turning off $\Phi^4_{\pi^*}/\text{SCl}_{\sigma^*}$ mixing	73
Figure 6.4.1 Fitted XAS of p-toluene sulfonyl chloride	75
Figure 7.1.1 XAS and complementary techniques	77

List of Schemes

Scheme 5.1.1 GSNO photo-reactivity induced reaction pathways	39
Scheme 5.1.2 LA photo-reactivity induced products	41
Scheme 6.1.1 Metal catalyzed polymerization with p-toluene sulfonyl chloride as an initiator	56
Scheme 6.1.2 Sulfonyl chloride photo-cleavage reaction	58

List of Equations

Equation 1.1.1 Bragg's law	3
Equation 1.2.1 Heisenberg uncertainty principle.....	6
Equation 6.4.1 Percent excited state hyperconjugation in p-toluene sulfonyl chloride	75

List of Abbreviations

Å	Angstrom
°C	Degrees Celsius
CysS	Cysteine
CysSSCys	Cystine
DFT	Density Functional Theory
DHLA	Dihydrolipoic Acid
DNA	Deoxyribonucleic Acid
EPR	Electron Paramagnetic Resonance Spectroscopy
eV	Electron Volt
<i>f</i>	Oscillator Strength
GPx	Glutathione Peroxidase
GR	Glutathione Reductase
Grx	Glutaredoxin
GSH	Glutathione
GSNO	Nitrosoglutathione
GSSG	Glutathione Disulfide
hr	Hours
K	Kelvin
LA	Lipoic Acid
m	Multiplet
MIN	Minutes
NMR	Nuclear Magnetic Resonance Spectroscopy
$P_{1/2}$	Power of Half Saturation (of EPR signal)
Prx	Peroxyredoxin
RF	Radio Frequency
RNR	Ribonucleotide Reductase
RS [•]	Thiyl Radical
RSNO	Nitrosothiol
RSS [•]	Perthiyl Radical
ΔSCF	Slater Transition State Self-consistent Field Method
SSRL	Stanford Synchrotron Radiation Lightsource
t	Triplet
TD-DFT	Time Dependent Density Functional Theory
Trx	Thioredoxin
TrxR	Thioredoxin Reductase
UV-VIS	UV-Visible Spectroscopy
XANES	X-ray Absorption Near Edge Structure
XAS	X-ray Absorption Spectroscopy
Z_{eff}	Effective Nuclear Charge

Acknowledgements

First and foremost I would like to thank Dr. Pierre Kennepohl, my supervisor and mentor, whose encouragement, patience and support, have not only made this work possible but have made my time as a graduate student a wonderful experience. His door has always been open and his help was always gladly given no matter the circumstance. Secondly, I would like to thank my lab mates, in particular Anusha Karunakaran with whom I have spent countless hours acquiring data, Mario Delgado with whom I have argued endlessly about everything under the sun and Kendra Getty who still holds the record for the number of straight hours of beamline data acquisition. Needless to say that I consider the fore mentioned people my friends and they will be sorely missed.

I would also like to thank Dr. Serena DeBeer George, who has always been ready to help at any time and who was of great help during our data acquisition trips at the Stanford Synchrotron Radiation Lightsource (SSRL). From experimental setup and running the data acquisition, to sample preparation, Dr. S. George was always there when needed. On a related note, I would also like to thank Dr. Matthiew Latimer for his help with experimental setup for our photo-irradiation studies.

Last but not least I would like to thank the UBC Chemistry department support staff, in particular Maria Ezhova for her help with NMR data acquisition, Jane Cua for her help with running and maintaining the ADF program, John Ellis for his help with acquisition orders, Ken Love and Razvan Neagu for their help over the years with equipment trouble shooting, and Pat Olsthoorn for his help with sample shipments to SSRL.

1 X-ray Absorption Spectroscopy (XAS)

This thesis relies heavily on the application of X-ray absorption spectroscopy (XAS) at the sulfur K-edge to investigate and characterize the bonding, electronic configuration, and reactivity of a series of biologically relevant low molecular weight thiols and their derivatives, as well as sulfur species with applications in inorganic polymer chemistry. Photochemistry was employed to follow the reactivity of these species, and investigate their reactive intermediates and products. XAS proved to be a useful technique in the detection and characterization of the elusive thiyl radical in UV irradiated glutathione. The perthiyl radical intermediate was detected in irradiated samples of lipoic acid and glutathione, as well as from irradiated nitrosogluthathione where formation of the perthiyl radical was a two step process. To perform the irradiation experiments, new methodologies of *in situ* photo-irradiation coupled with XAS spectra acquisition allowed the photo-reactivity to be observed. Last but not least, the relevance of excited state hyperconjugation was identified and its effect on the reactivity of p-toluene sulfonyl chloride explained as it pertains to the initiation step in the metal catalyzed polymerization of olefins. In each case, XAS was essential in the detection and characterization of these products.

1.1 THE SYNCHROTRON LIGHT SOURCE (X-RAY SOURCE)

X-ray absorption spectroscopy was the primary method used in these investigations. The intensities and the wide energy ranges used for the X-rays in the following experiments require a synchrotron source. A synchrotron light source consists of a circuit of accelerated electrons that give off electromagnetic radiation in the form of X-rays. All electrons when accelerated give off energy, and this has many applications in everyday life, such as radio signal transmission. In a synchrotron, however, electrons are accelerated to speeds approaching the speed of light (99.9% speed of light). These *relativistic* electrons give off electromagnetic radiation in a parallel path to the direction of propagation of the *relativistic* electron.

A synchrotron light source usually consists of a booster ring where electrons are accelerated to near the speed of light, from which they are injected into the storage ring (figure 1.1.1). Magnetic fields from “bend magnets” change the direction of the

electrons in the storage ring allowing them to maintain a closed path. The velocity of electrons is maintained by constructively interfering radiofrequency (RF) waves which takes place in the cavity. The RF waves are generated by a klystron (RF amplifier) similar to those used in TV broadcasting stations. The RF waves are guided to the cavity by a wave guide and timed to “synchronize” with the electrons entering the cavity. At various positions in the straight sections on the storage ring there are wigglers and undulators. These are a series of magnets with alternating polarities that cause the electrons to have small deviations in their linear trajectory, in a sense causing them to wiggle and undulate. Since the emitted X-rays have no charge they are not affected by the magnets and their trajectory is linear. X-rays emitted during a “wiggle” have a path that comes out of the storage ring and it can be delivered to various work stations (hutches) using beamlines. On any one storage ring there can be several wigglers and undulators allowing for multiple work stations or hutches.

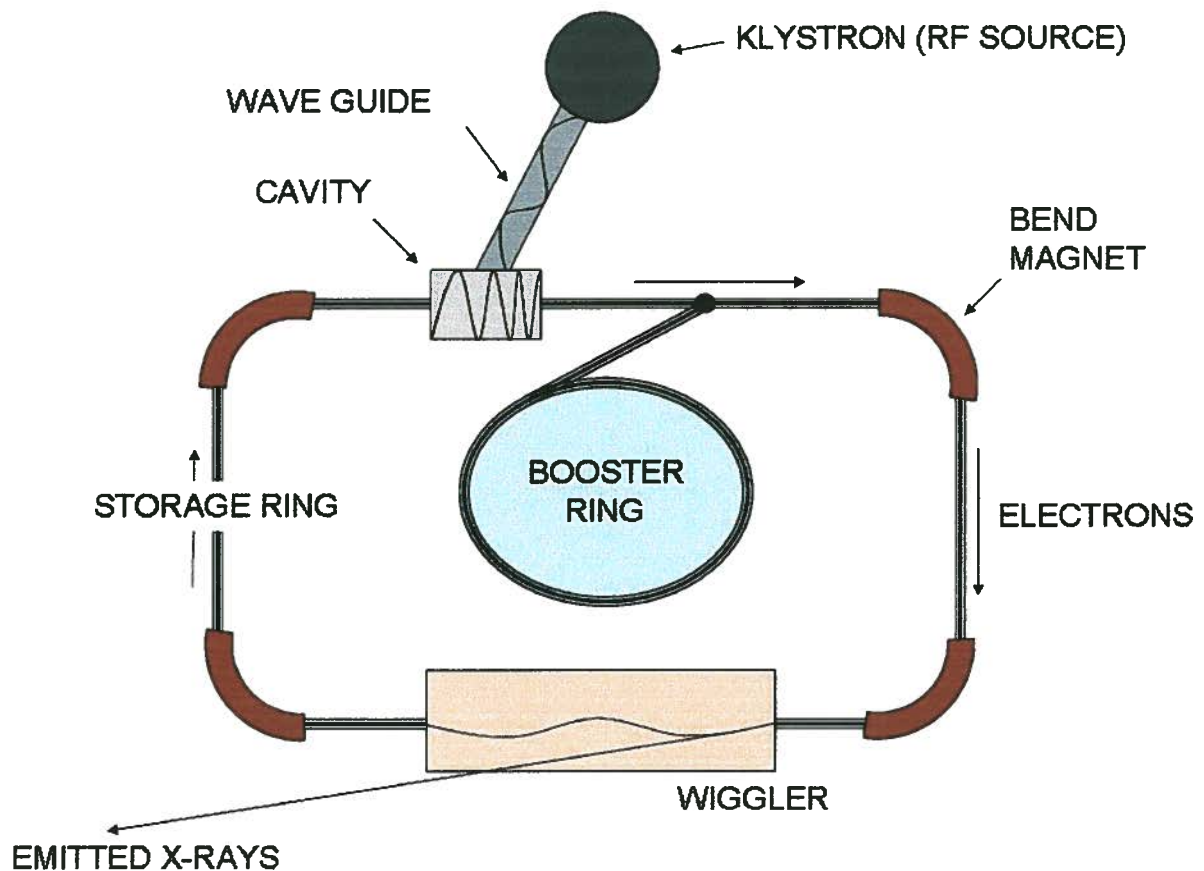


Figure 1.1.1 Schematic diagram of the main components found in a synchrotron.

Beamlines screen the broad range of radiation energies (from radio frequencies to γ -rays to X-rays) coming from the wiggler and select those needed for the particular experiment. They also shape the beam to suit the sample size and help control flux. This is achieved with the help of beamline optics as shown in figure 1.1.2. As the X-ray beam leaves the wiggler it may pass through a series of slits that shape it to have the needed dimensions. X-rays with the required experimental energies are then selected using a double crystal monochromator. X-rays of various energies are selected based on their wavelengths using Bragg diffraction. Bragg diffraction occurs when the incoming X-rays are scattered by the periodic structure of the crystal lattice according to equation 1.1.1.

$$n\lambda = 2d \sin \theta$$

Equation 1.1.1

n = harmonic (integer > 1)
 λ = wavelength
 d = distance between lattice layers
 θ = angle of diffraction

Therefore the crystal monochromators can be used to modulate the energies being diffracted to the experimental hutch by varying the angle of incidence of the X-rays and by changing the type of crystal used (lattice structure). If only one crystal was used scanning over a range of X-ray energies would mean moving the sample to match the angle of diffraction of the incoming beam. In practice, two crystal monochromators are used and moved in concert so that the diffracted beam is parallel to the incident beam. It is also evident from Bragg's equation that a series of harmonics or X-ray wavelengths can satisfy the equation for a particular angle of diffraction and crystal lattice structure. Therefore beamlines can be equipped with harmonic rejection mirrors which can efficiently refract X-rays of a certain energy range, but not those of its harmonics. These mirrors are coated with elements of higher atomic number because the refraction of X-rays of a particular energy is dependent on the material density of the coating. Mirrors can also be used to focus both the incident X-ray beam and the diffracted beam used for experiments. Once X-rays of the correct energy are isolated they are allowed to pass into the hutch. This is where the experimental setup for the various experiments is located (see Chapter 3 Methodology).

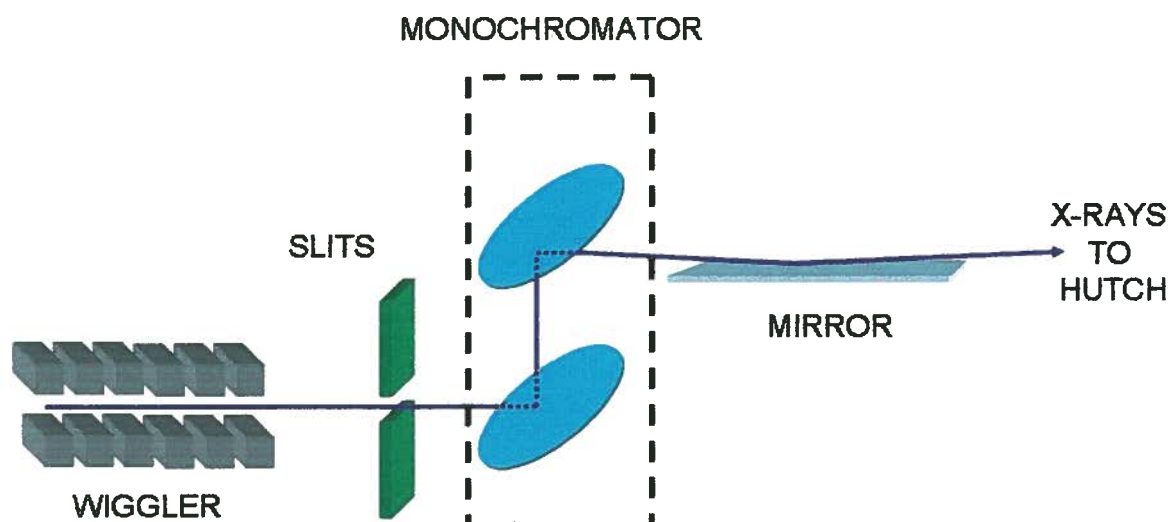


Figure 1.1.2 Schematic diagram of the main components found in a beamline.

1.2 SULFUR K-EDGE X-RAY ABSORPTION SPECTROSCOPY

Sulfur K-edge (S K-edge) XAS involves detection and characterization of sulfur core electron excitations, specifically those from the $1s$ core level (S_{1s}). Features due to these excitations, as well as electron ionizations from the S_{1s} core, fall in the 2400-2600eV energy range. The sulfur K-edge spectra is dominated by an ionization edge or “edge jump” due to excitations from the core $1s$ orbital to the continuum ($\infty \leftarrow S_{1s}$), resulting in ionization (figure 1.2.1 S^{2-}). Features due to S_{1s} excitations into unoccupied (figure 1.2.1 RS^-) or partially unoccupied (figure 1.2.1 RS^+) acceptor orbitals with sulfur character appear as absorption peaks. They fall within what is termed the X-ray Absorption Near Edge Structure (XANES) region of the spectrum. The intensities of these transitions are governed by Fermi’s Golden Rule which states that the intensity of a transition is proportional to the probability of it occurring¹. The probability of a transition occurring is dependent on the coupling between the ground state and the final state, therefore transitions resulting from atomic core excitations can only involve excitations to other orbitals in the same atom. Furthermore, dipole allowed ($s \leftarrow p$; $p \leftarrow d$) transitions have a higher probability of occurrence. This means that excitations of $1s$ sulfur core electrons into acceptor orbitals with a higher S_{3p} character will be more

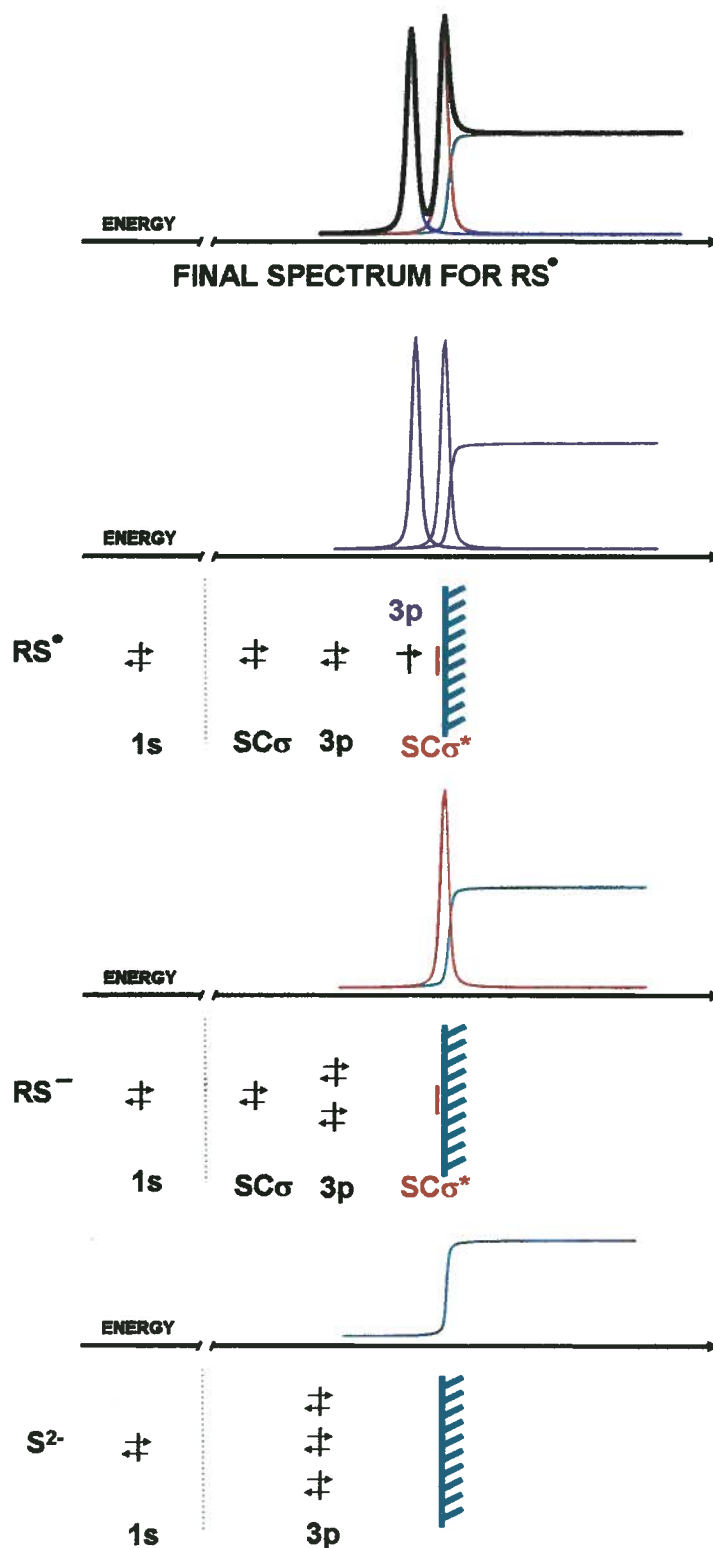


Figure 1.2.1 XAS model spectra showing the possible transitions and resulting XAS features from S^{2-} (only ionization is possible), thiolate (ionization and bound transitions to unoccupied molecular orbitals is possible) and the thiyl radical (ionization and bound transitions to both unoccupied and half occupied orbitals possible).

intense than transitions to acceptor orbitals having lower S_{3p} character. In addition, the probability of a transition is also dependent on the number of ways it can occur. At its simplest this means that a transition to a half occupied acceptor orbital should be half as intense as a similar transition to a fully unoccupied acceptor orbital. These acceptor orbitals are usually the antibonding counterparts of each of the chemical bonds sulfur is involved in, within the species being investigated. The intensities of these bound-state transitions can provide information regarding the amount of sulfur character in a particular bonding scheme, as well as the electronic configuration.

Equation 1.2.1

$$\Delta E \Delta t \geq \frac{\hbar}{2}$$

The spectral linewidth of the transitions is dependent on the resolution of the monochromator as well as the core-hole lifetime resulting from the particular transition. The core-hole lifetime is dependent on the energy of the transition according to the Heisenberg uncertainty principle (Equation 1.2.1). Therefore high energy transitions result in short core-hole lifetimes and broad features or linewidths, while low energy transitions such as those found at the sulfur K-edge result in long core-hole lifetimes and relatively sharp features. The line shapes for each of the transitions are a combination of a gaussian component as a result of the resolution of the monochromator and a lorentzian component due to the core-hole lifetime and can be described by a pseudo-voigt function which is a linear combination of the two components.

Another important feature of XAS transitions is the energy at which they occur. This is dependent on both the energy level of the core electrons, as well as that of the acceptor orbital. The energy level of the core electrons can be a measure of effective charge on the sulfur atom, while the energy of the acceptor orbital can give information about bond strengths. For example, in the study of perthiyl radicals (RSS^{\bullet}) there are two transitions from each of the sulfurs to the same SS_{π^*} acceptor orbital. If the two sulfurs were equivalent only one feature should be present because the two transitions would be overlapping. However, two transitions are visible corresponding to the difference in effective nuclear charge (Z_{eff}) between the sulfurs which lowers the core electron energies in one of the sulfurs versus the other.

1.3 APPLICATIONS OF XAS

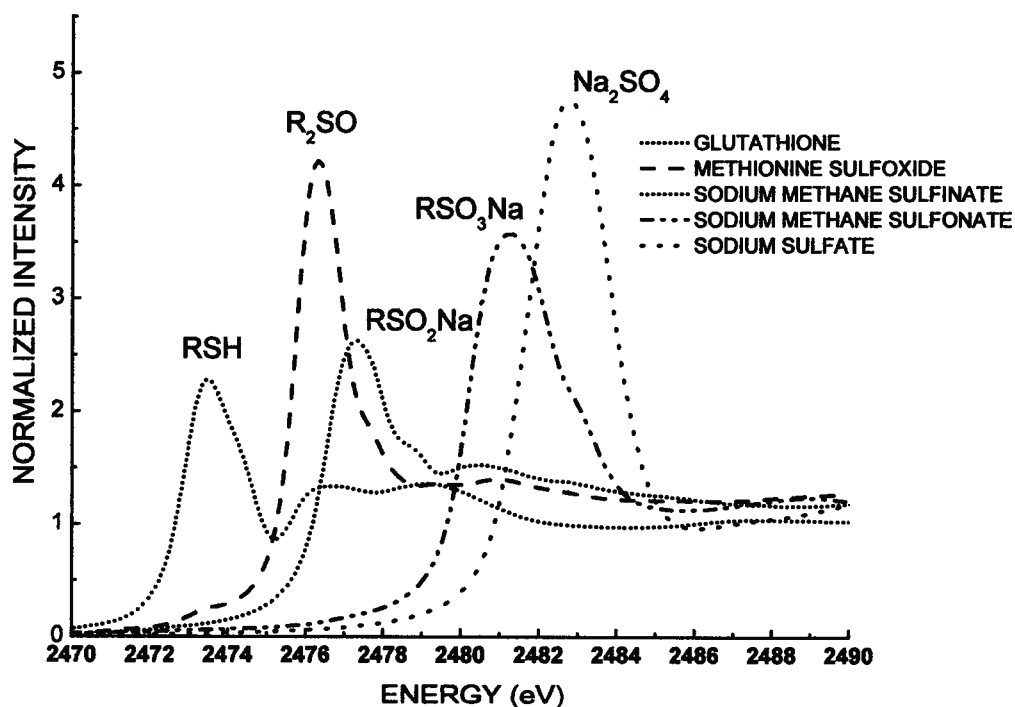


Figure 1.3.1 XAS fingerprint spectra of sulfur species with varying oxidation states.

The nature of the transitions observed in sulfur K-edge XAS make this technique sensitive to the various oxidation states of sulfur (figure 1.3.1). In fact, much of the literature involving sulfur K-edge XAS use the “fingerprint” method to investigate sulfur speciation. In this approach, the composition of the sulfur K-edge spectrum from a particular sample is determined by fitting and summing up spectra from similar samples containing 100% of a particular sulfur oxidation state^{2,3}. This method can be applied to both non-biological and biological systems.

For example, sulfur speciation as it pertains to the effectiveness of different coal desulfurization methods was investigated using least square fitting of the XANES region of spectra from various coal samples that were desulfurized using either biological, chemical or caustic leaching methods⁴. Sulfur K-edge XAS was also used to assess the impact of land use by characterizing sulfur oxidation in soil samples from natural forest, tea plantations and cultivated fields from various locations in Ethiopia. Natural forest were found to have the most reduced sulfur species, followed by plantations with cultivated fields being most oxidized⁵. Most notably, oxidation of reduced sulfur species in the seventeenth-century Swedish warship, Vasa, was found to be catalyzed by iron

from corroded iron bolts, leading to the formation of sulfate salts which threaten the preservation of the ship⁶.

Researchers have also collected the spectra for a variety of biologically relevant sulfur species. The distinct features differentiating between thiol groups and disulfides were used in a number of studies investigating the thiol redox couple responsible for redox homeostasis, in blood, and separated plasma and erythrocyte samples^{2, 3}. Extracellular cysteine was found to be mostly in its oxidized cystine form while intracellular cysteine was found to be more reduced^{2, 3}. Increased oxidation state of sulfurs in transthyretin investigated with sulfur K-edge XAS is seen in amyloid fibrils, the main component of amyloid deposits present in such disorders as Alzheimer's disease and Creutzfeldt-Jakob disease⁷. Features due to S-H bonds ($\text{SH}_{\sigma^*} \leftarrow \text{S}_{1s}$), S-C bonds ($\text{SC}_{\sigma^*} \leftarrow \text{S}_{1s}$), and S-S bonds ($\text{SS}_{\sigma^*} \leftarrow \text{S}_{1s}$), in samples were identified by comparing the XANES features from H_2S , H_2S_2 and reduced and oxidized cysteine^{2, 8}. Investigation of the dependence of the cysteine spectra on pH shows a dramatic change in the spectral features with deprotonation^{2, 9}.

Another advantage of this technique is its ability to tolerate a broad range of sample types and preparation techniques. For example, the studies discussed thus far have included solid samples in the form of coal, soil, and wood; liquid samples in the form of blood, plasma and buffered cysteine, and H_2S and H_2S_2 gas samples. It is not surprising then, that samples consisting of various sulfur accumulating bacteria were prepared and quantitative sulfur speciation studies were carried out. At least three different forms of sulfur were found in bacterial sulfur globules with cyclooctasulfur being prevalent in *Beggiatoa alba*, polythionates in *Acidithiobacillus ferrooxidans* and sulfur chains in green and purple sulfur bacteria¹⁰.

XAS becomes an even more powerful experimental technique when coupled with simulations of the electron excitation transitions along with calculations of the orbitals of the donor and acceptor states involved in the transitions. This was first recognized and explored in chlorine K-edge XAS spectroscopy¹¹ and then extended to sulfur K-edge XAS where the metal-ligand covalency was measured in transition metal tetrathiolate complexes¹². XAS coupled with density functional calculations (DFT) were used in the characterization of the Cu-S bond in the active sites of blue copper proteins which was found to have a high covalency (38% S_{3p} character) and a unique single π -bond between the copper and the sulfur¹³. The methodology was then applied to the

investigation of oxidation, reduction, and bonding of iron sulfur clusters in ferredoxins and rubredoxins¹³. XAS and DFT were further used to assign the spectral features for S-nitroso proteins where transitions to SC_{σ^*} , $S-NO_{\sigma^*}$ and $S-NO_{\pi^*}$ acceptor orbitals were identified¹⁴. The dependence of XAS spectra of disulfides on the dihedral angle was investigated by comparing the experimental and simulated spectra of oxidized lipoic acid to those of less conformationally strained disulfides. The results showed distinct differences in both the intensity and peak width of the $SS_{\sigma^*} \leftarrow S_{1s}$ and $SC_{\sigma^*} \leftarrow S_{1s}$ transitions, emphasizing the importance of accounting for molecular conformations when analyzing spectra using the fingerprint method¹⁵.

1.4 THESIS OVERVIEW

The above discussion is meant to show the range of applicability of this experimental technique. It has been shown that sulfur K-edge XAS is sensitive to sulfur oxidation regardless of sample preparation. Sulfur speciation and electronic structure can be gained from the XANES region of the spectra encompassing bound transitions to low-lying molecular orbitals with S_{3p} character. A combination of the fingerprint method and density functional calculations can be used in the assignment of spectral features and characterization of the sulfur bonding manifold. The current study investigated *in situ* photo-reactivity of both biological and non-biological samples. In each case DFT calculations were applied to better assign the spectral features and understand the electronic configuration. Additional spectroscopic techniques were used in the characterization of starting materials, intermediates and products. Particularly electron paramagnetic resonance (EPR) spectroscopy was essential in the detection and characterization of radical intermediates generated during the photo-reactivity studies. The following chapters cover a discussion of the experimental setups used throughout the thesis, a brief overview of the importance of low molecular weight sulfur based antioxidants in redox homeostasis, followed by the studies involving the main representatives of these species chosen for their relevance, reactivity and interesting electronic structure. Last but not least, is the investigation of the bonding and electronic configuration of p-toluene sulfonyl chloride as it pertains to its role as an initiator in the metal catalyzed polymerization of styrene, methacrylates, and acrylates.

2 Implications of Thiol Oxidation

Low molecular weight sulfur species are involved in a variety of processes that maintain the oxidative balance *in vivo*. These compounds (table 2.1.1) are known to have antioxidant properties which come into play particularly in times of oxidative stress, when increases in oxidizing species disrupt regular cell function. Their interaction with reactive oxygen (ROS) and nitrogen (RNS) species not only have antioxidative consequences but are also important in signaling pathways. Low molecular weight thiols and their derivatives could be described both as “middle men” and, due to their antioxidant functions, as modulators of these signaling pathways. Their antioxidant properties also make low molecular weight sulfur compounds potential therapeutic agents in various diseases with symptoms of oxidative stress. Of these the most important and abundant is glutathione (GSH), which behaves as a redox buffer within the cell¹⁶. Outside the cell the most important thiol for maintaining redox homeostasis is cysteine (CysS)¹⁶.

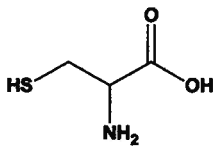
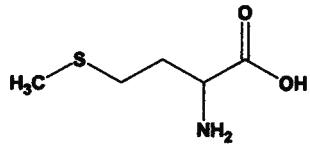
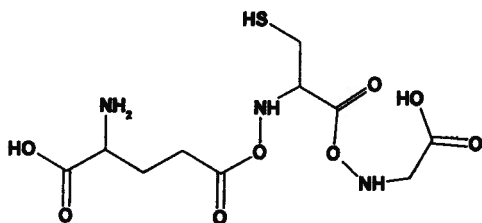
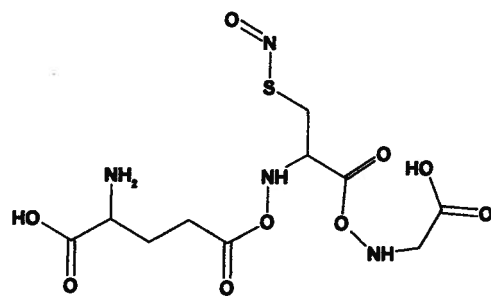
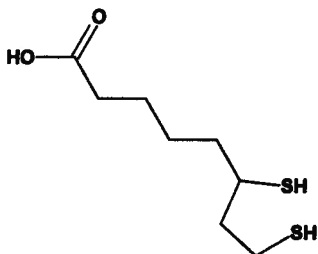
2.1 LOW MOLECULAR WEIGHT SULFUR SPECIES IN VIVO

	PROLIFERATION	DIFFERENTIATION	APOPTOSIS	
INTRACELLULAR (GSH)	-260/-230 mV	-220/-190 mV	-170mV	
[RSH] > [RSSR]				→ [RSH] < [RSSR]
EXTRACELLULAR (CysS)	< -80 mV	-80 mV	> -80 mV	

Figure 2.1.1 Intracellular and extracellular disulfide/thiol redox state at various stages in the lifecycle of the cell as described by the GSSG/2GSH couple (intracellular) and CysSSCys/2CysS couple (extracellular)^{16, 17}.

Thiol oxidation has been linked to several cellular processes with implications ranging from cell signaling to progression of disease. Both the glutathione (GSSG/2GSH) and cysteine (CysSSCys/2CysS) redox states vary over the life cycle of the cell (figure 2.1.1). One can see a progression to a more oxidized state going from proliferation to apoptosis^{16, 17}. The extent of oxidation has been explored in several systems by induction of differentiation in proliferating cells. Application of the differentiating agent sodium butyrate to a HT29 cell line caused a +60mV shift (from -260mV in the proliferating cells to -200mV in the differentiating cells)¹⁸. Exposure of slime mold to differentiation stimuli resulted in a decrease in GSH

Table 2.1.1 Biologically important low molecular weight sulfur species.

LOW MOLECULAR WEIGHT SULFUR SPECIES	
<p>Cysteine (CysS)</p> <p>Precursor to GSH and the major extracellular thiol redox buffer^{16, 19}.</p>	
<p>Methionine</p> <p>In addition to being used for cysteine synthesis, methionine oxidation/reduction is involved in metal ion channel gating and neurodegenerative diseases²⁰.</p>	
<p>Glutathione (GSH)</p> <p>The most abundant low molecular weight thiol, has antioxidant properties, modulates protein function through S-glutathionylation and maintains redox homeostasis²¹.</p>	
<p>Nitrosoglutathione (GSNO)</p> <p>Used in the storage, transport and delivery of NO* a molecule important in cell signaling²².</p>	
<p>Dihydrolipoic acid (DHHLA)</p> <p>Lipoic acid (LA) is the oxidized form, has a redox couple of LA/DHHLA (-320mV) and can directly reduce GSH²³. Can chelate metal ions and prevent lipid peroxidation²⁴. It is an antioxidant in both hydrophilic and lipophilic environments²⁵.</p>	

and an increase in the antioxidant enzyme manganese superoxide dismutase (MnSOD), indicating a shift to a more oxidized environment during differentiation²⁶.

Variation of thiol oxidation states also occurs within the cell. Compartmentalization allows a more reduced environment within the nucleus where the GSH pool is implicated in protection from oxidative stress of DNA²⁷ and DNA binding motifs²⁸, regulation of gene transcription²⁹, DNA synthesis³⁰, and DNA repair^{31, 32}. In the endoplasmic reticulum on the other hand, the thiol redox couple favors the more oxidized state. Here the redox state of the GSSG/2GSH couple is approximately -180mV³³, as opposed to -260mV in the nucleus¹⁶. This facilitates disulfide bond formation and isomerization of incorrectly formed disulfide bonds³⁴, a process modulated in part by protein disulfide isomerase (PDI), a thiol disulfide oxidoreductase^{34, 35}.

The disulfide/thiol redox state can also be affected by external factors such as disease. A prime example is the oxidative pressures associated with HIV (Human Immunodeficiency Virus). In HIV there is a systemic decrease in reduced GSH³⁶⁻³⁹ and GSH synthesis⁴⁰ along with a decrease in total cysteine and cystine amounts ($[CysS] + 2[CysSSCys]$)³⁸. Chronic increase in thioredoxin (Trx, a family of proteins involved in the reduction of disulfides) concentrations can further compromise the innate immune response by inhibition of lipopolysaccharide induced chemotaxis, resulting in shorter life expectancy of AIDS victims⁴¹. Addition of NAC (N-acetylcysteine) increases survival¹⁶ and *in vitro* addition of GSH and NAC inhibits viral replication⁴², indicating the potential for therapeutic applications of low molecular weight thiols.

Last but not least, thiol oxidation can also affect signaling pathways. Protein tyrosine phosphatase (PTP) has a catalytically active cysteine residue which can be inhibited if oxidized to a sulfenic acid by H_2O_2 ⁴³. Increased thiol oxidation and GSSG/GSH ratios also seem to stimulate the activity of several kinases such as the mitogen activated protein kinases (MAPK), JNK (c-Jun N-terminal kinase) and p38,⁴⁴ required for tumor necrosis factor (TNF- α) induced apoptosis⁴⁵. Nuclear transcription factors can also be affected by GSH oxidation. For example, Nrf 2 (NE-F2 related factor) which regulates expression of several genes involved in antioxidant response^{46, 47}, is translocated to the nucleus when its Keap-1 subunit dissociates from the main complex due to oxidation and conjugation of its cysteine residues⁴⁸. However, within the nucleus, DNA binding activity is controlled by Trx⁴⁹, which maintains Nrf 2's

DNA binding cysteine residue in its reduced form⁵⁰, highlighting the importance of compartmentalization, as discussed earlier.

2.2 MECHANISM AND CONTROL OF THIOL OXIDATION

Reactive Oxygen (ROS) and Nitrogen (RNS) Species and Thiol Oxidation

Thiol oxidation can be driven by the reactive oxidant pathways of ROS and RNS coupled with disulfide reduction systems such as those of the thioredoxins (figure 2.2.1). Comprehensive reviews on the formation and consequences of reactive oxygen species (ROS) and reactive nitrogen species (RNS) are available⁵⁰⁻⁵³. These reactive species can arise endogenously from cellular processes or be mediated by external factors such as chemotherapeutic agents, UV irradiation, and other environmental stimuli⁵⁰⁻⁵³. At low concentrations, ROS and RNS can be beneficial and many are involved in signaling pathways⁵⁰, gene transcription²⁹ and host defenses against infection. Examples are leukocyte release of ROS to attack infecting bacteria⁵⁴, NO[•] induction of smooth muscle relaxation^{55, 56}, and NO[•] inhibition of platelet aggregation⁵⁷. Thiols and thiol redox pathways play important roles both as antioxidants to maintain ROS and RNS at homeostatic levels and as intermediary mediators in some of the ROS/RNS signaling pathways.

In eukaryotes reactive oxygen species arise mainly in mitochondria from aerobic respiration^{58, 59} or enzymatic reactions of NADP(H) oxidases in leukocytes⁵⁴. The product of such reactions is the superoxide anion (O₂^{•-}) which is not membrane permeable and thus reacts within whichever cellular compartment it is created⁶⁰. O₂^{•-} is converted to hydrogen peroxide (H₂O₂) by superoxide dismutase (SOD)⁶¹. H₂O₂ is membrane permeable and can act as a signaling molecule^{50, 62}. In the presence of redox-active metal ions, H₂O₂ is rapidly converted to the hydroxyl radical (HO[•]) via the Fenton reaction⁶³⁻⁶⁵. HO[•] is highly reactive and unselective towards a host of biological molecules. H₂O₂ can also oxidize thiols, and in high enough concentrations, it can lead to the generally irreversible sulfur oxidation states of RSO₂H and RSO₃H⁶⁶. Three main enzyme systems are employed in H₂O₂ removal: catalases (CAT)⁶⁷, glutathione peroxidase (GPx)⁶⁸ and peroxyredoxins (Prx)⁶⁹ will degrade H₂O₂ to yield H₂O and O₂. The latter two, GPx and Prx involve intermediate oxidation of thiols. GPx reduction of H₂O₂ results in GSH dimerization to GSSG⁶⁸. Prx is initially oxidized to sulfenic acid

(RSOH), which in the case of 1-CysS Prx can be reduced by vitamin C⁷⁰. In 2-CysS Prx (Prx containing two cysteines in its active site) the initial oxidation to RSOH is followed by internal disulfide bond formation which can be later reduced by thioredoxins⁷¹. Prx can also be further oxidized by H₂O₂ to give sulfinic acid (RSO₂H), which can be reduced back to the active form by sulfiredoxin⁷¹⁻⁷³.

NO[•] production from arginine is facilitated by nitric oxide synthase and similar to O₂⁻, it is the first product in the RNS chain⁷⁴. NO[•] can further react with O₂ to give N₂O₃, a nitrosylating agent, and with O₂⁻ to give peroxynitrite (ONOO⁻)⁵². The reaction of NO[•] with thiols is generally considered too slow to have biological relevance, however N₂O₃ can nitrosylate a variety of substrates including thiols to give S-nitrosothiols⁷⁵. ONOO⁻ contributes to oxidative stress and is scavenged by thiols resulting in disulfide bonds⁷⁶. Denitrosation is facilitated by dihydrolipoic acid (DHLA) and Trx, which undergo oxidation resulting in release of a free thiol and HNO⁷⁷. Similar to the denitrosation mechanism of DHLA and Trx, transnitrosation reactions, followed by S-thiolation and disulfide bond formation modulate protein activity as is the case of creatine kinase⁷⁸. Release of NO[•] can also be achieved by decomposition of two nitrosothiols or nitrosothiol reduction of metals such as copper. Both cases result in formation of a disulfide^{79, 80}.

Disulfide formation via reduction of metals such as vanadium, copper and iron is also possible and reported to proceed through a thiyl radical intermediate^{65, 81-83}. Thiols such as glutathione and dihydrolipoic acid can ligate metal ions and are involved in both metal detoxification⁸⁴ and delivery⁸⁵. Reduced metal ions such as arsenic (III), chromium (IV) and chromium (V), copper (I), and iron (II) can induce oxidative stress, and their ligation may help in their excretion which would prevent them from reacting to induce oxidative stress^{63, 86}. Metal reduction by GSH and GSH derivatives is associated with lipid peroxidation, which stimulates oxidative stress rather than represses it. The efficiency of the reduction is modulated by the ligating abilities of the thiol species and their pKa's^{87, 88}. Lipid peroxidation due to Cu²⁺ is inhibited by DHLA which is believed to chelate the metal via its vicinal thiols. The stability of the complex however, is pH dependent and the complex becomes destabilized with increasing pH²⁴.

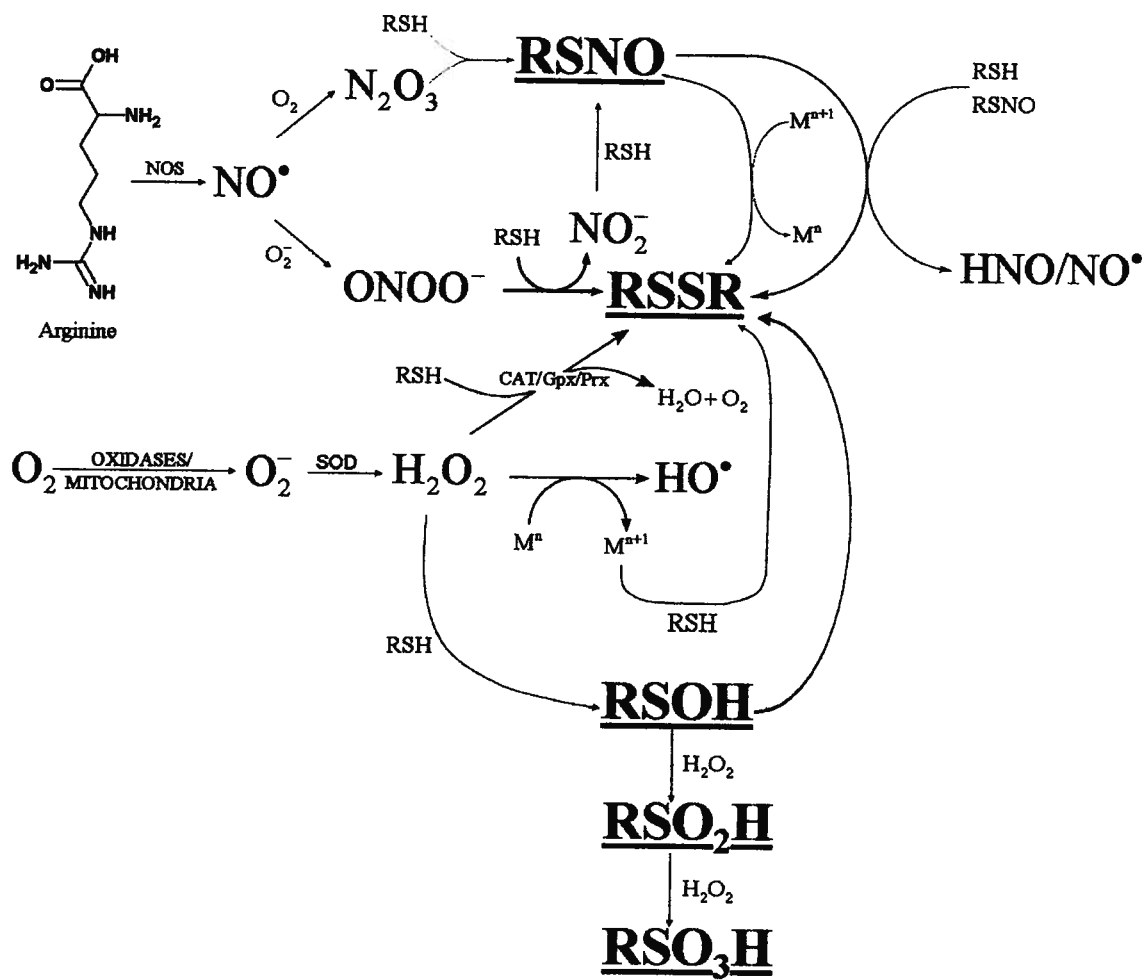


Figure 2.2.1 Thiol oxidation pathways, *in vivo*.

Mechanisms of Disulfide Reduction

From the discussion of ROS and RNS one can see that thiols tend to become oxidized to disulfides when exposed to oxidative pressures. Therefore, a mechanism for the reduction of disulfides to thiols must exist to rejuvenate the reduced thiol pool. The principal pathways for such processes are the thioredoxin and glutaredoxin enzyme systems (figure 2.2.2).

Thioredoxins (Trx) are a family of thiol-disulfide oxidoreductases found within both prokaryotes and eukaryotes⁸⁹. The active form found in the cytosol and nuclei of cells is thioredoxin-1 (Trx 1)⁹⁰, while mitochondria has the thioredoxin-2 (Trx 2) isoform which contains an N-terminal mitochondrial translocation sequence⁹¹. A third form of thioredoxin is found in spermatozoa, called sperm-specific Trx (Sptrx)⁹². All isoforms contain a conserved active site sequence: Cys-Gly-Pro-Cys⁹³. They interact with a variety of disulfide containing species, most notably ribonucleotide reductase (RNR) involved in DNA repair and synthesis³¹, transcription factors, PDI in the endoplasmic reticulum, and peroxyredoxins^{53, 94}.

The Trx mechanism of action involves nucleophilic attack of the disulfide species to be reduced by the Trx N-terminal cysteine, forming a mixed disulfide intermediate. This in turn is reduced by the C-terminal cysteine of Trx⁹⁵. The end products are a reduced dithiol species and an oxidized Trx now containing a disulfide in its active site⁹⁵. Trx is ultimately reduced by thioredoxin reductase (TrxR) coupled with oxidation of NADPH to NADP⁺ and formation of a Sec-SCys bond in TrxR⁹⁶. TrxR is a homodimer selenocysteine (Sec) enzyme⁹⁷. The Sec site is located near the C-terminal of the enzyme (Gly-Cys-Sec-Gly-COOH)⁹⁸. The motif is conserved across species and isoforms of TrxR⁹⁹. Enzymatic activity of oxidized TrxR is restored by donation of electrons from NADPH via a bound FAD to a thiol/disulfide site (Cys-Val-Asn-Val-Gly-Cys) present in one subunit of TrxR reducing it to a dithiol. This site is similar in structure and reactivity to that of glutathione reductase (GR) and is in the proximity of the Sec residue on the second subunit of TrxR. This allows the thiol/disulfide site to donate electrons to the C-terminal selenocysteine-cysteine bond (Sec-SCys), reducing it and restoring TrxR reduction capabilities^{100, 101}.

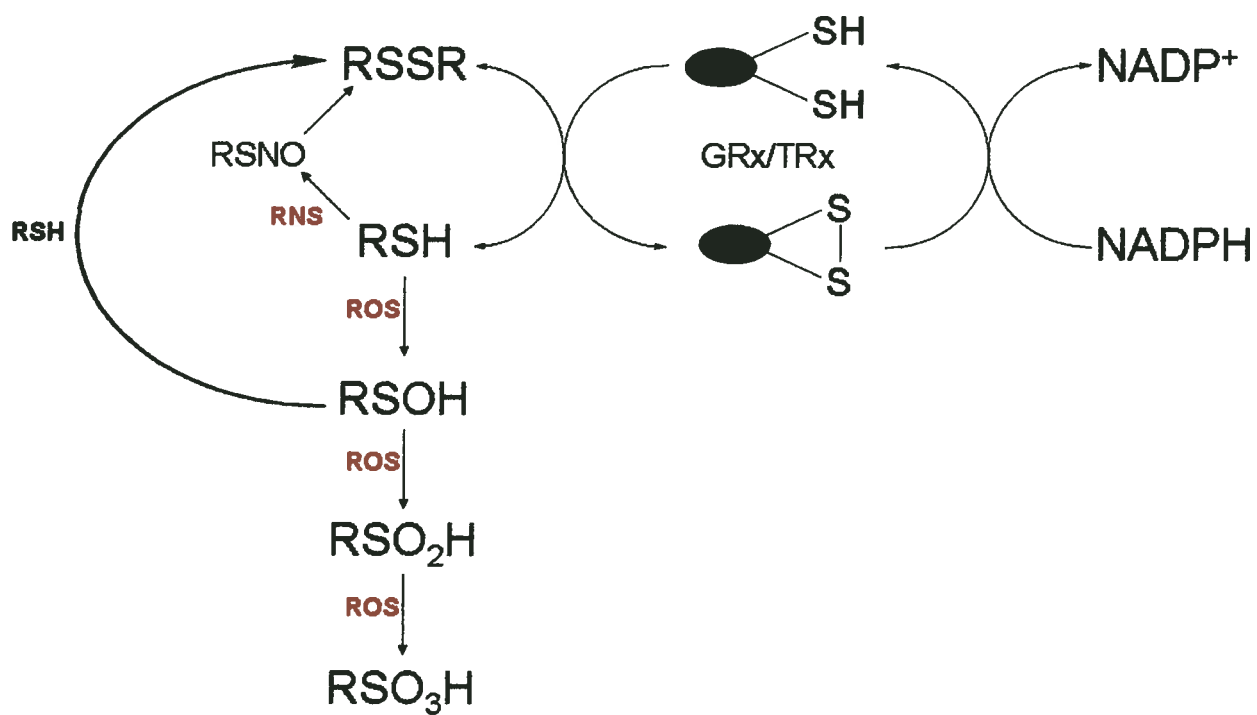


Figure 2.2.2 Reduction pathways of oxidized sulfur species, *in vivo*.

Glutaredoxins (Grx) are another essential family of thiol/disulfide oxidoreductases, which only differ slightly from thioredoxins in their mechanism of action. The major isoform, glutaredoxin 1 (Grx 1), is found in the cytosol and has an active site sequence Cys-Pro-Tyr-Cys¹⁰². Mitochondria have two glutaredoxins, glutaredoxin 2 (Grx 2) with the active site sequence Cys-Ser-Tyr-Cys¹⁰³ and glutaredoxin 5 (Grx 5) with only one cysteine in its active site implicated in iron homeostasis¹⁰⁴. Grx 1 is associated with dithiol/disulfide exchanges⁹³, cell differentiation¹⁰⁵ and apoptosis¹⁰⁶, dehydroascorbate reduction¹⁰⁷, transcription factor regulation¹⁰⁸, and as an electron source for ribonucleotide reductase^{31, 94}. Grx can also catalyze the formation and reduction of mixed disulfides between proteins and GSH¹⁰⁹, which has implications in protein regulation and cellular responses to oxidative stress⁹⁴.

Similar to thioredoxins, Grx reduces disulfide bonds by oxidizing its own active site cysteines to a cystine. However, the Grx active site is reduced by GSH to give GSSG. First one GSH forms a mixed disulfide with Grx, followed by formation of GSSG when a second GSH interacts with the complex¹¹⁰. The resulting GSSG can be reduced to GSH at the expense of NADPH by glutathione reductase (GR)¹¹¹⁻¹¹³. Similarly, GSSG resulting from the Gpx catalyzed reduction of H₂O₂ is reduced to GSH by glutathione reductase. GR is a homodimer¹¹⁴ with binding sites for NADPH and GSH, which are opposite to each other but on the same subunit¹¹⁵. The electrons are transferred from the NADPH binding site to the active site of the enzyme via an FAD prosthetic group next to the redox active cystine residues^{113, 115, 116}. The active site has the Cys-Val-Asn-Val-Gly-Cys sequence, which is conserved in humans and yeast, and is similar to lipamide dehydrogenase and TrxR^{113, 117}. Upon electron donation from NADPH the active site becomes reduced and catalytically active.

2.3 EXPERIMENTAL RATIONALE

Evidently, thiol oxidation is central to several biological processes, ranging from redox homeostasis to DNA transcription and modulation of enzyme activity. The most encountered oxidation states are the reduced –SH thiol of cysteines essential for transcription factor binding to DNA, and its counterpart the disulfide bond with implications in modulation of protein function as outlined by its effect on translocation of transcription factors to the nucleus. Enzymatic activity can also be affected by thiol

oxidation, as is the case of tyrosine phosphatase, where formation of sulfenic acid inhibits its function. Therefore characterization of the oxidation states of sulfur centers is important in the exploration of enzyme mechanisms as well as metabolic pathways.

Unfortunately, there are no conventional methods that can analyze sulfur oxidation. The most common way of detecting thiols is the use of Ellman's reagent (DTNB, 5,5'-dithiobis-2-nitrobenzoic acid)¹¹⁸. DTNB is a disulfide that exchanges with free thiols in solution to give a yellow chromophore¹¹⁸. Other chemical derivatization methods for detecting thiols involve tagging thiols with maleimides, iodoacetamides, iodoacetates or thiosulfates, all of which have to be linked either to fluorophores, radionucleotides, affinity labels such as biotin or labels that will change the overall molecular weight¹¹⁹. This is generally followed by gel electrophoresis and comparison between runs with tagged thiols and runs with untagged thiols to look for band profile changes. Similarly disulfide bonds are investigated via electrophoresis under oxidizing and reducing conditions followed by comparison of band shifts¹¹⁹. Analysis of other oxidation states is often further complicated by the short lifetime of the species. Sulfenic acids, are generally not very stable but have been detected *in vitro* by selective reduction with sodium arsenite or selectively reacting them with dimedone or NDB-Cl (7-Chloro-4-nitrobenzo-2-oxa-1,3-diazole) followed by biotinylation^{119, 120}. A similar method involves detection of S-nitrosylated thiols by selective reduction with sodium ascorbate followed by biotinylation¹²¹. Both methods have the drawback of requiring denaturing conditions and alkylation of free thiols prior to treatment with the selective reducing agents¹¹⁹.

Therefore, sulfur K-edge XAS is proposed as an alternative and direct method to look at thiol speciation, which may prove to be a powerful tool in elucidating the catalytic mechanisms of enzyme systems. It has the advantage of being sensitive to all sulfur oxidation states. Disulfide bonds and free thiols along with methionine, sulfenic, sulfinic and sulfonic acids are readily detected by XAS^{3, 122}. Furthermore, spectral fitting of a mixture of thiols with varying oxidation states allows for quantitative analysis of the sample^{2, 9}. Most recently XAS was proven to be a useful technique for the detection of S-nitrosylated proteins¹⁴. This suggests XAS could be applied to detect intermediates in the catalytic cycle of enzymes which are difficult to see by other means. A prime example is ribonucleotide reductase (RNR). There are three classes of this enzyme and in each case the reduction of the ribose moiety of the nucleotide substrate is

believed to have a thiyl radical intermediate^{123, 124}. Thiyl radicals are notoriously difficult to characterize due to their large spin orbit coupling ($\xi=382\text{cm}^{-1}$)¹²⁵ and broad g_{\parallel} component^{126, 127}. Sulfur K-edge XAS, on the other hand, should be very sensitive to the dipole allowed $S_{3p}\leftarrow S_{1s}$ transition from the thiyl radical.

XAS can also prove to be a useful source of information on particular bonding manifolds around the sulfur atom. It was previously proposed based on theoretical calculations coupled with X-ray structural data that the sulfonyl moiety (SO_2) in $\text{R}_a\text{SO}_2\text{R}_b$ type compounds experiences hyperconjugation interactions from the R_a nonbonding orbitals into the S-R_b σ^* antibonding orbital¹²⁸. A similar effect was also inferred in the case of aryl sulfonyls, which experience a bathochromic shift in the UV-VIS spectra of their benzyl group when the sulfonyl moiety is present¹²⁹. Because sulfur K-edge XAS consists of transitions to unoccupied or partially unoccupied molecular orbitals it could be a direct probe for the detection of hyperconjugative effects which result from molecular orbital mixing.

Thus, this thesis involved development of *in situ* experimental methods to investigate the reactivity, intermediates and products of biologically relevant low molecular weight thiols. Furthermore, the electronic configuration around sulfonyl groups was probed to investigate the effects of hyperconjugation on the reactivity of these compounds. The findings reported here, and the experimental methods devised, provide steps toward expanding XAS identification of thiol species in more complex systems, such as enzyme catalysis and reaction pathways.

3 Experimental Section

To study the reactivity of sulfur model compounds samples were photo-irradiated with a Xenon arc lamp and X-ray absorption data was collected. The experimental setup for *in situ* photo-reactivity of sulfur containing model compounds is described in the subsection below. Time-dependent density functional theory was employed to better understand and assign the transitions giving rise to the various features of the XAS spectra. Electron paramagnetic resonance spectroscopy (EPR) was used to help identify the sulfur based radical intermediates formed during photolysis while nuclear magnetic resonance (NMR) was used to characterize the starting materials and final products. The materials used in the following experiments are described in section 3.5.

3.1 X-RAY ABSORPTION SPECTROSCOPY (XAS)

Experimental Setup

The XAS data was collected at beam line 6-2 of the Stanford Synchrotron Radiation Lightsource (SSRL). The facility is a 3GeV ring with a current of 60-100mA. Beam line 6-2 operates in a high magnetic field mode of 10kG and consists of a 54-pole wiggler followed by a Ni coated harmonic rejection mirror, and a fully tuned Si(111) double crystal monochromator. The beam-line optics are under vacuum and protected from the pressurized experimental hutch by a 127 μ m beryllium window followed by a 6.35 μ m polypropylene window and a He chamber¹³. The spot size of the incident beam is controlled by a pair of horizontal and vertical JJ X-ray exit slits followed by a He gas ionization chamber, which measures the intensity of the incident beam (I_0). The sample chamber is isolated from the ionization chamber by another polypropylene window. The sample itself is 45° to the incident beam and 45° to a fluorescence ion chamber Stern-Head-Lytle detector¹³⁰, which was filled with argon gas and maintained at ambient temperatures. He flow from a liquid helium cooler provided by Cryo Industries (HFC-1645 LHE-Cryocool) maintains the sample below -20°C where it can be photo-reacted with a Ushio 75W Xenon arc lamp positioned 50cm from the sample. At these temperatures the samples did not react in the X-ray beam. The sample chamber encasing consists of a specially adapted transparent glove-bag providing an anaerobic He atmosphere for data collection (figure 3.1.1). By varying the point to point

increments, number of data points and collection time at each point, the scan rate was varied in order to better follow the rate of photo-reactivity¹³¹. The spectrometer resolution was $\sim 0.5\text{eV}$ ¹³².

Solid samples were mounted as a finely ground powder dusted on the adhesive side of sulfur-free Kapton tape (polyimide film with silicone adhesive) to minimize fluorescence self absorption effects¹³. Methyl sulfonyl chloride was mounted as a neat solution on the sulfur-free Kapton tape and covered with a polypropylene window under a nitrogen atmosphere. Spectra were acquired while the samples were irradiated with a 75W Xenon arc lamp at 253K (-20°C) under a helium atmosphere with $<1\%$ oxygen content. Glutathione mounted on the Kapton tape was irradiated with UV light at ambient temperature under aerobic conditions. The UV irradiation source was a LonglifeTM Filter 254nm shortwave ultraviolet lamp from Spectroline[®].

XAS spectra processing

Energies of the Sulfur K-edge XAS spectra were calibrated using hydrated sodium thiosulfate ($\text{Na}_2\text{S}_2\text{O}_3 \cdot 5\text{H}_2\text{O}$) with the first pre-edge feature peak maximum being calibrated at 2472.02eV ¹³. The value of 2472.02eV for the first pre-edge feature was arrived at by repeated experiments on different beamlines and checked against the inflection point of sulfur at 2471.3eV and the X-ray absorption spectra of molybdenum and copper foil¹³². An alternative value for the first pre-edge feature of sodium thiosulfate is 2469.2eV determined by calibrating the spectra of sodium thiosulfate to the first intense feature in the spectra of NiS powder assigned as occurring at 2469.8eV ¹³³. Spectra were background subtracted using the method of energy summation of two linearly weighted background terms derived from the background before and the background after the edge jump of the XAS spectra¹³⁴. The magnitude of the edge jump was normalized to a total intensity of 1. Principal component analysis of transient spectra was carried out using SixPack version 0.53¹³⁵.

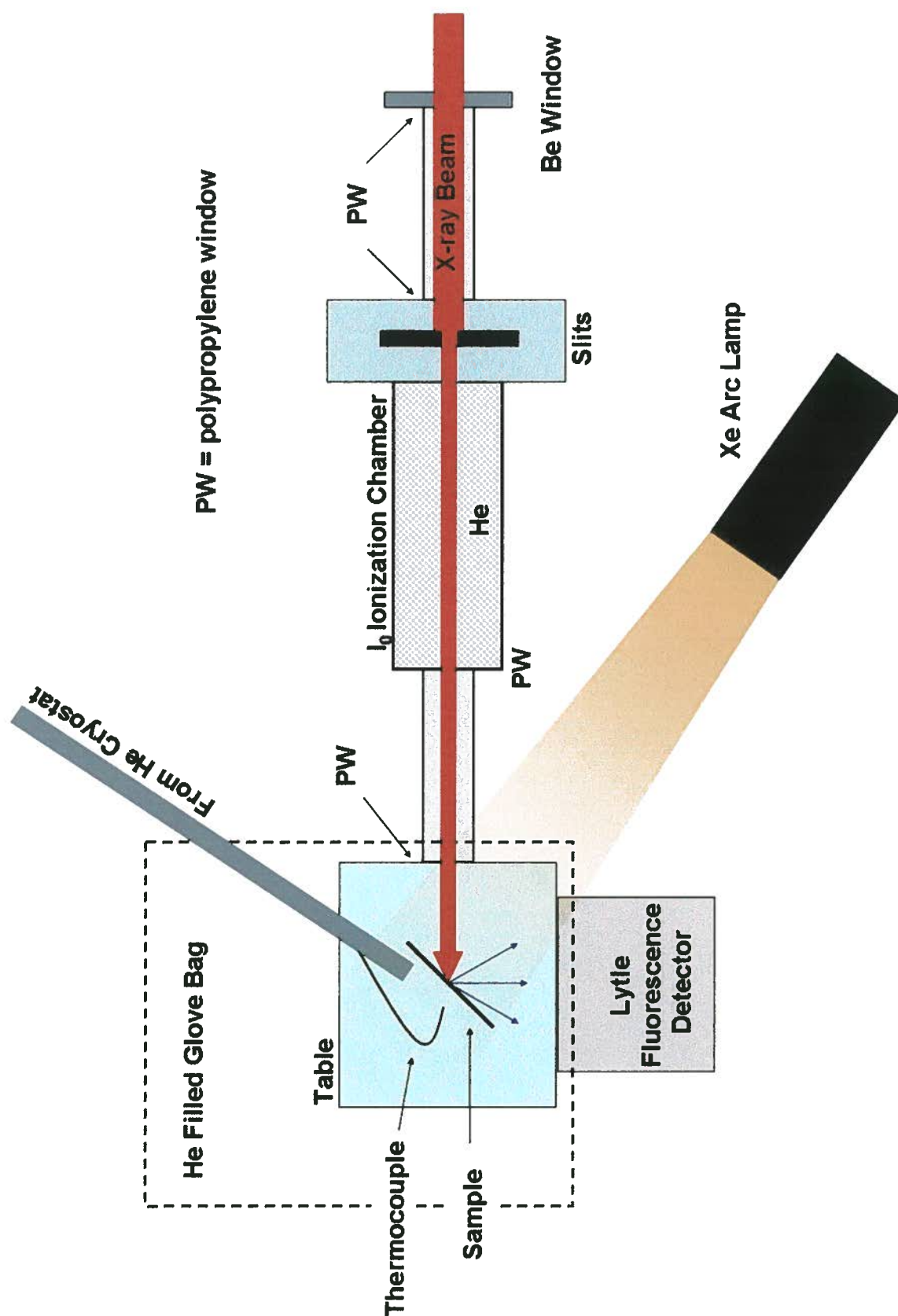


Figure 3.1.1 XAS experimental setup at SSRL beamline 6-2.

3.2 DENSITY FUNCTIONAL CALCULATIONS

Molecular orbital calculations to simulate spectrometric parameters and deduce molecular bonding interactions were carried out for the various species investigated. Density functional theory calculations were carried out using the Kohn-Sham Self-consistent field methodology provided with the Amsterdam Density Functional Software Package 2007.01^{136, 137}.

Full geometry optimizations were followed by single-point and time-dependent density functional theory (TD-DFT) calculations. Calculations were performed using the BP86 functional and a doubly polarized triple- ζ basis sets (TZ2P) using Slater-type orbitals (STO) basis functions. TZ2P was necessary to allow for the interaction between the sulfur valence (3s, 3p and 3d) orbitals resulting in correct geometries for the hypervalent sulfur atom. Previous researchers have shown this combination of functional and basis sets to give the best approximation for calculated spectra and relative experimental energies and intensities in ligand K-edge XAS¹. To calculate the corresponding sulfur core 1s excitations for each of the compounds, the ModifyExcitations key was used, along with the no core option for any of the atoms and no symmetry operations were applied. The resulting excitation energies for the sulfur 1s electrons were shifted by 76-81eV to account for deviations in the calculated core excited-state energies from experiment. These energy shifts fall within range of those calculated by other researchers¹. In the case of the aryl and alkyl sulfonyl compounds fragment calculations were necessary to better understand contributions to molecular orbitals from the different “fragments” such as the aryl and sulfonyl moieties. Fragment calculations consist of modeling the orbital interactions for each fragment individually and then combining them to give the final picture.

To assist in the spectroscopic assignment of XAS features and to account for relaxation effects due to electron excitation,¹³⁸⁻¹⁴⁰ the transition energies were recalculated using the Slater transition state self-consistent field method (Δ SCF) for the first 10 transitions of each model compound of interest. XAS spectra were then simulated using the recalculated energies and the oscillation strengths calculated with TD-DFT. Δ SCF was done by having 1.5 electrons in the S_{1s} orbital and one-half of an

electron in the orbital of interest which gives a good estimate for the relaxation energy in most core ionization/excitation cases¹⁴¹.

The magnitude of the calculated oscillatory strengths were used for the peak areas needed to simulate the features of the various XAS spectra using a pseudo-voigt function with 80% lorentzian and 20% gaussian character. The intensities of the oscillatory strength were normalized to fit the normalized experimental spectra. Details of further molecular calculations and deviations from the above procedures are mentioned in the text wherever applicable. Sample input files are found in Appendix 1.

3.3 NUCLEAR MAGNETIC RESONANCE SPECTROSCOPY (NMR)

NMR data was collected on a Bruker AV 300 NMR spectrometer. ¹H NMR data was collected with a 15ppm sweep width centered at 6ppm, each spectrum consisting of 128 scans with a time domain of 32K. Samples were dissolved in deuterium oxide (D₂O) solvent with a 99.9% deuterium atom composition, having a proton peak maximum calibrated at 4.80ppm.

3.4 ELECTRON PARAMAGNETIC RESONANCE SPECTROSCOPY (EPR)

X-band EPR data collection at 9.5GHz was carried out using a Bruker Eleksys E 500 series continuous wave EPR spectrometer running the Xepr software package. Photo-reactivity studies were carried out using a 75W Xenon arc lamp positioned 50cm from the sample. *In situ* irradiation experiments were carried out while collecting spectra at room temperature or, using a finger dewar filled with liquid nitrogen, at temperatures of 77K. Studies at 195K (-78 °C) were carried out by irradiating the sample while in an acetone-dry ice bath followed by data acquisition at 77K. *In situ* experiments were not viable in acetone-dry ice bath because of “lossyness” due to microwave absorption by acetone. Samples were run either under vacuum or under an argon gas atmosphere. DPPH (g=2.0036) was used as the standard for spectra calibration¹⁴². Power saturation profiles were acquired by varying microwave powers between 63mW and 0.002mW. Further details and deviations from the above procedures are mentioned in the text when needed. Simulation of spectra was carried out using the Bruker WinEPR SimFonia software package.

3.5 MATERIALS

Sulfur-free Kapton tape was purchased from Creative Global Services Inc. and checked for sulfur contamination (by sulfur K-edge XAS) before use. The irradiation sources consisted of a Longlife™ Filter 254nm shortwave ultraviolet lamp from Spectroline® for UV irradiation and a Ushio 75W Xenon arc lamp for full spectrum irradiation. 707-SQ-250 EPR tubes and a large finger dewar flask 150ml (Suprasil WG-853-B-Q) from Wilmad Labglass were used for EPR experiments. Polycrystalline powders of reduced L-glutathione, (±)-α-lipoic acid, *p*-toluene sulfonyl chloride, *p*-toluene sulfonic acid, phenyl ethyl sulfone, methionine sulfone, and sodium methane sulfonate along with a neat solution of methane sulfonyl chloride were purchased from Sigma-Aldrich and stored at 4°C until use. S-nitrosoglutathione was synthesized by reacting glutathione with sodium nitrite under acidic conditions and characterized using NMR (chapter 5 figure 5.2.7 p.52) and by its absorption at 545nm using UV-VIS¹⁴³. Glutathione, (±)-α-lipoic acid and *p*-toluene sulfonyl chloride were also characterized using NMR and no contaminants were found.

S-nitroso glutathione (GSNO) synthesis

To a mixture of 5ml of deionized water mixed with 5ml 1M HCl, 5mmol (1.5g) of glutathione (GSH) were added and dissolved. The solution was kept in an ice bath wrapped in aluminum foil to prevent product photo-degradation. To the colorless GSH solution, 5mmol (0.35g) of sodium nitrite was added. The reaction immediately turned red and was stirred for 1 hour. Precipitation of the GSNO product was initiated with 10ml of -20°C acetone followed by a further 30 minute of stirring. The product was then filtered by suction filtration and washed successively with 5 x 0.5ml of ice-cold water, 5 x 1ml acetone and 6ml of diethyl ether added drop-wise. The pale pink product was dried and stored in the dark at -20°C until use.

4 Sulfur K-edge XAS as a Probe of Sulfur-Centered Radical Intermediates

4.1 BACKGROUND

Sulfur based radical intermediates are involved in various biological processes¹⁴⁴, most notably the enzymatic reduction of ribose sugars in ribonucleotide reductase (RNR)^{145, 146}. Thiyl radicals are postulated to be essential in the catalytic mechanism of all classes of ribonucleotide reductases¹²⁴ however their detection and characterization have been elusive. Paramagnetic species are generally detected using electron paramagnetic resonance spectroscopy (EPR), however this is somewhat complicated for sulfur because of its relatively large spin orbit coupling ($\xi=382\text{cm}^{-1}$)¹²⁵ and broad g_{\parallel} component of thiyl (RS^{\bullet}) radicals^{126, 127}. Recently Lassman and coworkers have generated thiyl radicals using UV irradiation in polycrystalline glasses of both protein and cysteine samples. Integrated EPR spectra of UV irradiated bovine serum albumin (BSA), and the R1 subunit of RNR were compared to that of UV irradiated 300mM cysteine samples^{146, 147}. The UV irradiated cysteine samples exhibit a weak signal at a g_{\parallel} of 2.30 attributed to the thiyl radical. When integrated this gives “a broad ascending slope” in the absorption spectrum leading to the main absorption features at lower g values¹⁴⁶. Similar “slopes” were also detected in the protein samples and attributed to the thiyl radical even though the g_{\parallel} signal was absent in the 1st derivative spectra. Such analysis requires careful background subtraction and the researchers chose the 330mT point in the field domain as the cutoff for the thiyl “absorption feature” so that other features present would not superimpose with the thiyl radical g_{\parallel} signal. Although this approach has proven useful in the detection of free thiyl radicals, proper characterization of the thiyl radical using this method can be hindered by many factors such as incorrect baseline subtraction, imperfections in the EPR tubes, as well as the presence of other features which may overlap with the absorption signal of the integrated EPR spectrum of the thiyl radical. Other EPR approaches to the detection of thiyl radicals involve spin trapping agents. Unfortunately, spin trapping techniques cannot provide information about the g -tensor of the radical, hyperfine couplings, or radical lifetimes^{147, 148}.

Therefore XAS is proposed as a new tool for detecting thiyl radical intermediates which has the added advantage of also detecting EPR silent sulfur intermediates such

as sulfenic, sulfinic, and sulfonic acids that generally rely on secondary methods of detection such as chemical methods involving thiol derivatization¹¹⁹. These species can often form as byproducts of the radical generating reactions and their identification and characterization is important in the overall reaction mechanism. These studies used glutathione as a model compound which has a redox couple ($2\text{GSH} \leftrightarrow \text{GSSG} + 2\text{e}^-$) that is essential for proper redox balance and homeostasis. It has been shown that photochemical one-electron oxidation of GSH forms a multitude of radical products including the short-lived thiyl (GS^\bullet) and long-lived perthiyl (GSS^\bullet) radicals, yet the one-electron redox chemistry of GSH and cysteine is still somewhat unclear. Therefore, polycrystalline glutathione is used as a model system for evaluating the use of sulfur K-edge XAS in the study of sulfur-containing radicals.

4.2 RESULTS AND DISCUSSION

Characterization of Irradiated Samples with EPR

Experimental conditions were as described in the experimental section. Polycrystalline GSH was irradiated in the UV region ($\lambda=254\text{nm}$) at room temperature ($295 \pm 5\text{K}$) giving an EPR spectrum that has been previously investigated and attributed to a complex mixture of radical species (i.e., GS^\bullet , G^\bullet , H^\bullet , and GSS^\bullet)¹⁴⁶. XAS data was collected for samples irradiated from 2 to 48 hours. EPR of the UV-irradiated samples remained unchanged even after prolonged exposure to the X-ray beam (>3 hours) and were not affected by the Kapton tape.

From the spectra in figure 4.2.1 one can see that the features of the “ GSH^{XAS} ” spectra and those of “GSH” are comparable. “ GSH^{XAS} ” was a sample prepared and used for the XAS experiment. It consisted of GSH on Kapton tape irradiated for 48 hours and its EPR spectrum was acquired at room temperature. “GSH” is glutathione polycrystalline powder irradiated for 4 hours and placed in an EPR tube with its EPR spectrum acquired at room temperature. Both samples exhibit features at g values of 2.030 and 2.057 that are due to the perthiyl radical, while the feature at 2.009 is in the thiyl radical g_\perp region ($g \approx 2.01$) as previously reported by Lassman *et al.* and Neese *et al.*^{127, 146}. In addition, the features of the simulated perthiyl EPR spectrum (figure 4.2.1) correspond well to those of irradiated glutathione. The perthiyl radical EPR spectrum was simulated with g values at 2.057, 2.03 and 2.07 which match well those derived

from the density functional calculations of the $\text{CH}_3\text{SS}^\bullet$ model for the perthiyl radical used to analyze the XAS spectra. The calculated g values for the $\text{CH}_3\text{SS}^\bullet$ perthiyl radical are 2.058, 2.027 and 2.002. The difference in the lower g values at 2.002 and 2.07 between the actual and calculated spectra may arise because of the presence of additional EPR signals such as those from a possible thiyl radical.

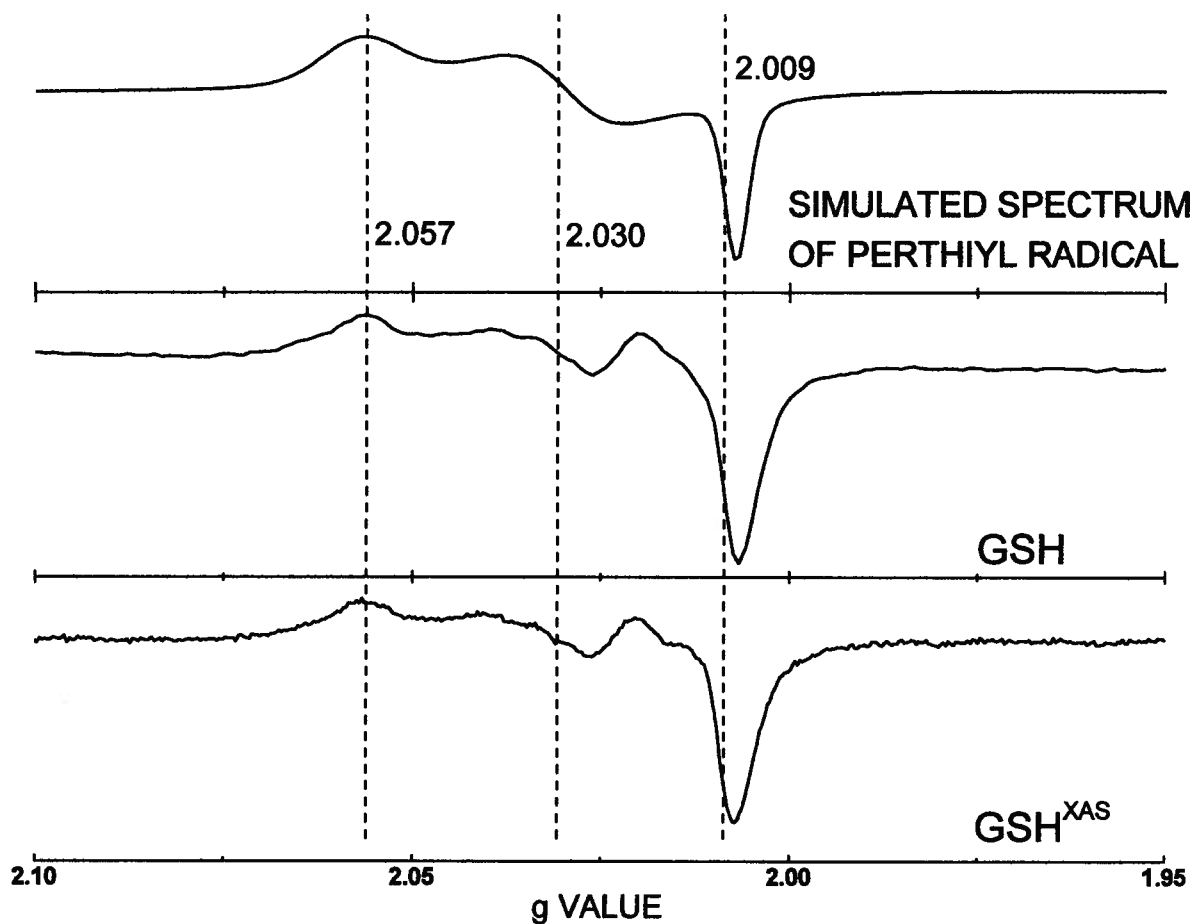


Figure 4.2.1: X-band EPR spectra of UV irradiated glutathione. “ GSH^{XAS} ” is GSH on Kapton sulfur free tape irradiated for 48 hours and used for XAS with EPR collected at room temperature (power 2mW, 3scans, modulation amplitude 5G, modulation frequency 100kHz); and “GSH” is GSH powder irradiated overnight and placed in an EPR tube and run at room temperature (power 2mW, 3scans, modulation amplitude 5G, modulation frequency 100kHz). The simulated spectrum of perthiyl radical has g values of 2.062, 2.030 and 2.007.

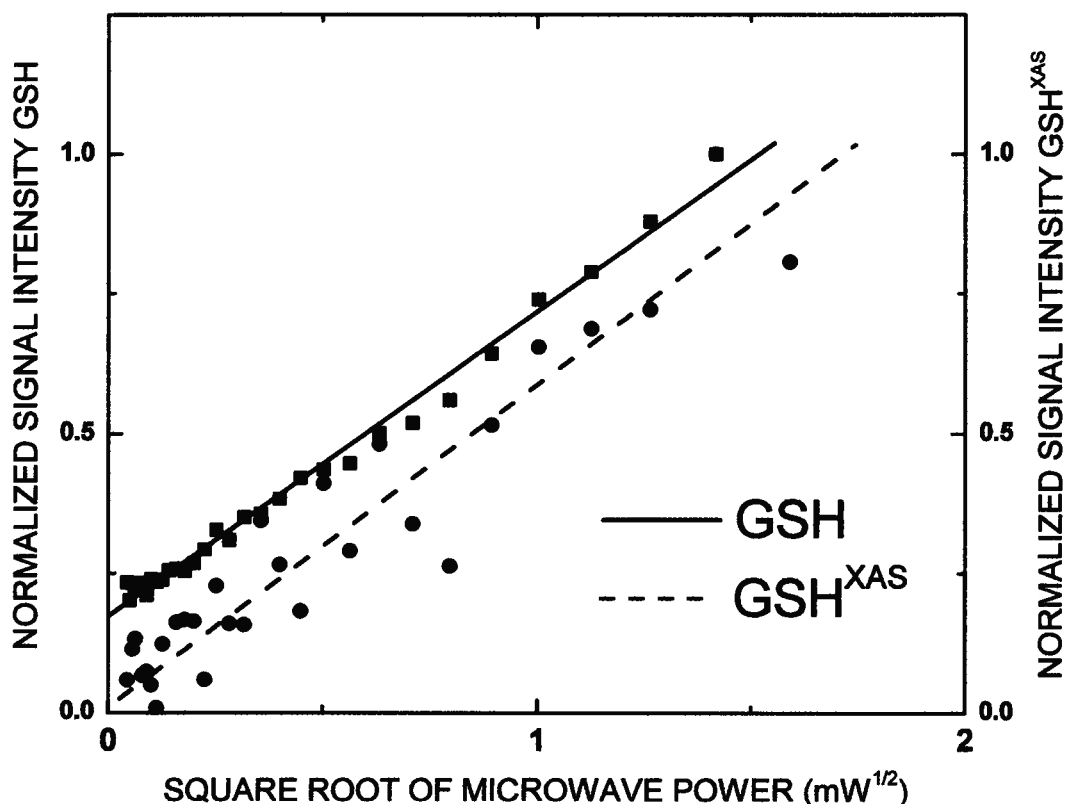


Figure 4.2.2: Power saturation study of the EPR signals from “GSH^{XAS}” and “GSH” samples.

The presence of the perthiyl radical was further confirmed with power saturation studies (figure 4.2.2). The feature at $g=2.057$ was chosen for these studies because it does not overlap with other spectral features. It is found that the signal at 2.057 increases linearly with higher microwave powers in the range of 0.002mW to 20mW, which is consistent with the low saturation effects seen in perthiyl radicals^{146, 149}. The $g_{||}$ of the thiyl radical was not observed in the EPR spectra of either the “GSH^{XAS}” or the “GSH” samples but was identified in the XAS spectra.

Characterization of Irradiated Samples with XAS

The XAS data of UV irradiated GSH, shows distinct changes in the GSH spectrum upon irradiation (figure 4.2.3 and 4.2.4). The GSH spectrum is initially dominated by an intense $CS_{6^*} \leftarrow S_{1s}$ at $\sim 2473.5\text{eV}^3$. With UV-irradiation, new pre-edge features appear at 2468.8eV and 2470.5eV and the $CS_{6^*} \leftarrow S_{1s}$ feature of GSH broadens and decreases in intensity. The reactivity of GSH can also be followed by the

disappearance of the features at 2476.7eV and 2479.3eV. Second derivative analysis of the spectra shows the presence of an additional feature at 2471.5eV as indicated by an inflection point in this region (figure 4.2.4 B). These pre-edge features coincide with the appearance of radical species in the EPR spectra and therefore should correspond to transitions to the half-occupied sulfur orbitals of sulfur-centered free radicals. At longer irradiation times, a high energy feature at 2482.6eV appears indicative of a highly oxidized sulfur species. This species has not been characterized, however formation of stable sulfoxyl radical intermediates along with sulfinic and sulfonic species have been reported as a result of photo-irradiated sulfur containing amino acids¹⁴⁶. Principal component analysis (table 4.2.1) on the transient spectra shows that 3 components are needed to obtain >0.99 cumulative variance for the low energy pre-edge region of the spectra (2465 - 2475eV) whereas 4 components are needed when the higher energy components are included (2465 - 2490eV). This indicates the formation of 3 species as a result of irradiation.

Table 4.2.1. Principal component analysis of UV irradiated GSH XAS spectra from the various irradiation time points. Dotted lines show the number of components needed for >99% cumulative variance over the energy ranges described.

COMPONENT ANALYSIS FOR 2465eV – 2475eV RANGE		
Component	Eigenvalue	Cumulative Variance
1	25.62	0.907
2	1.75	0.969
3	0.63	0.991
4	0.12	0.995
5	0.04	0.997
6	0.03	0.998
7	0.02	0.999
COMPONENT ANALYSIS FOR 2465eV – 2490eV RANGE		
1	46.42	0.922
2	2.24	0.966
3	0.89	0.984
4	0.33	0.990
5	0.25	0.995
6	0.14	0.998
7	0.05	0.999

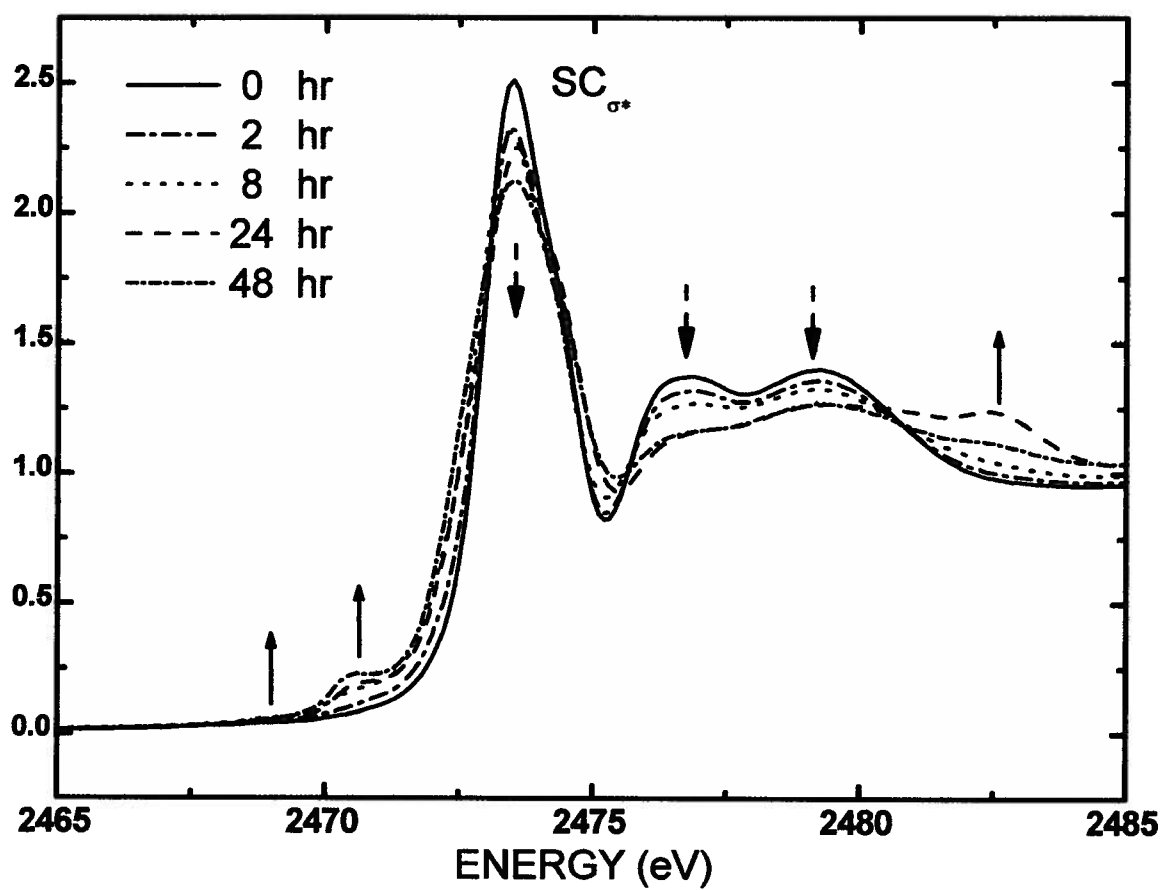


FIGURE 4.2.3 Sulfur K-edge XAS of UV irradiated GSH after various time intervals of irradiation.

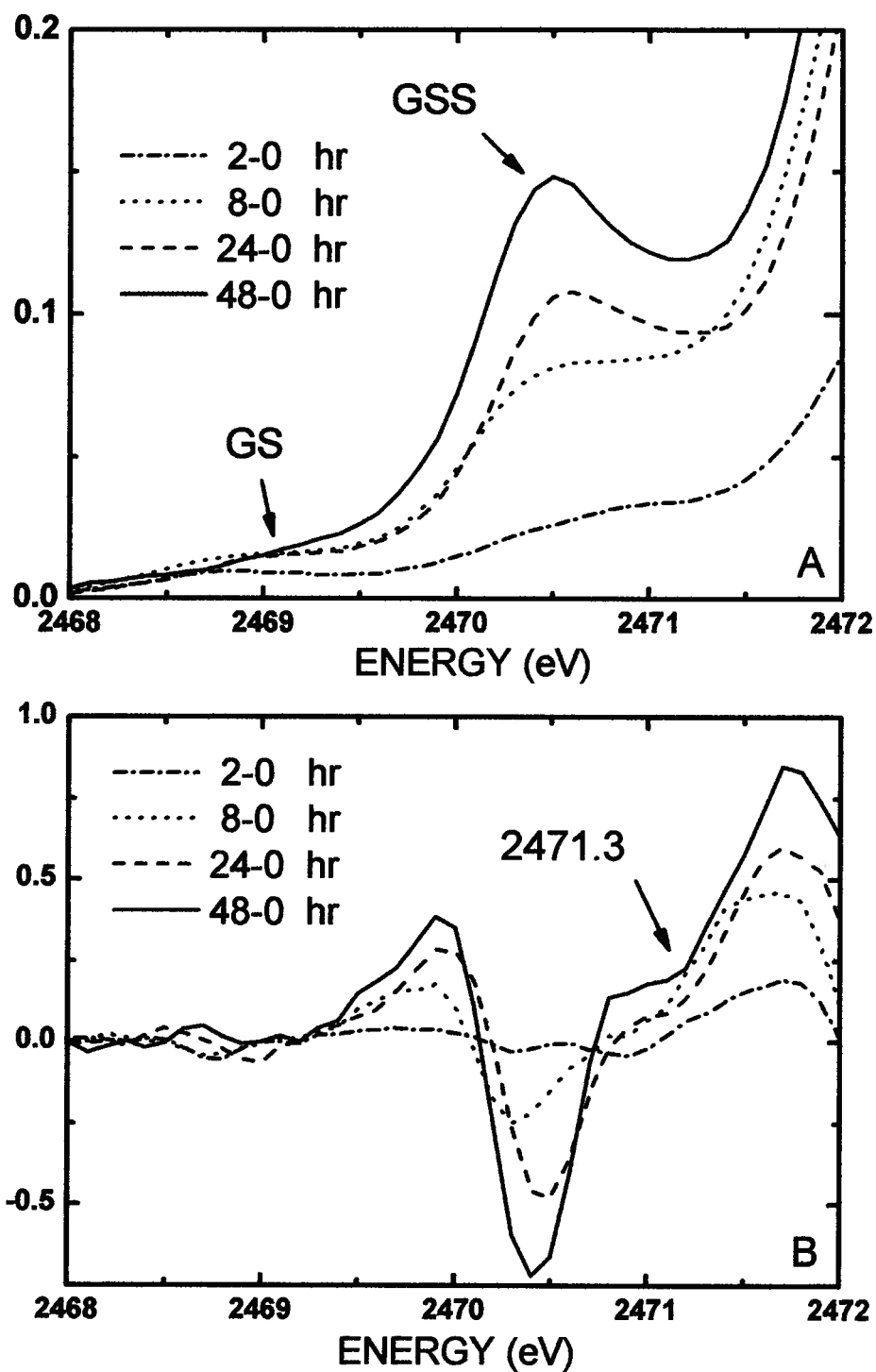


Figure 4.2.4 Difference XAS spectra of UV irradiated GSH at various times and GSH control (A) and the second derivative of the difference spectra showing an inflection point at 2471.3eV (B).

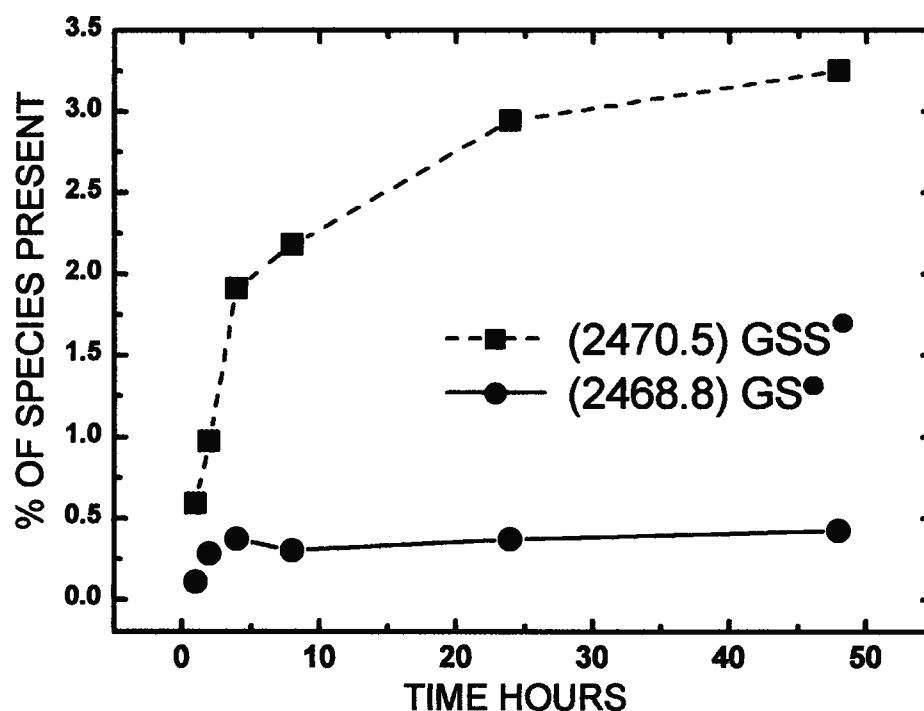


Figure 4.2.5 Time evolution of the features 2468.8eV and at 2470.5eV in terms of calculated percentage of thiyl and perthiyl radical after various intervals of irradiation.

Based on differences in their rates of formation (figure 4.2.5) the two low-energy pre-edge features must correspond to different sulfur radical species, most likely GS* (thiyl) and GSS* (perthiyl), respectively. To better understand the electronic structure and characteristics of these transitions a combination of unrestricted ground state and time-dependent density functional theory (TD-DFT) calculations were carried out on simplified models of the expected thiyl (CH_3S^*) and perthiyl (CH_3SS^*) radical species. Electron density maps were generated and the important empty valance orbitals are shown in figure 4.2.6 with relevant transitions listed in table 4.2.2. Spectra at the sulfur K-edge are dominated by transitions with electric dipole allowed $\text{S}_{3p} \leftarrow \text{S}_{1s}$ character; therefore empty orbitals with S_{3p} character are of most importance. DFT results show that the unpaired electron in GS* resides in a singly-occupied S_{3p} orbital perpendicular to the S-C bond axis¹²⁷. Two other orbitals, labeled CS_{σ^*} and HC_{σ^*} , have significant S_{3p} character and account for the two major bound-state transitions at 2473.7eV and 2474.5eV in the Sulfur K-edge spectrum of GS*. The HC_{σ^*} final state obtains much of its sulfur K-edge intensity through intensity borrowing from the CS_{σ^*} state at ~1eV higher

energy. The lowest energy transition at 2468.8eV corresponds to a nearly pure ($\sim 92\%$) $S_{3p} \leftarrow S_{1s}$ transition attributed to the singly occupied sulfur 3p orbital.

The unpaired electron in GSS^\bullet is located in a SS_{π^*} orbital (figure 4.2.6). Two transitions should be observed to this orbital, one from each of the S_{1s} orbitals. TD-DFT calculations indicate a significant splitting of the two SS_{π^*} transitions of 1.3eV suggesting a more positive effective charge for S^A , which lowers its 1s core orbital energy. The σ^* transitions for GSS^\bullet include both CS_{σ^*} and SS_{σ^*} contributions that occur at about the same energy as in the GSH spectrum. It is important to note that the low-energy pre-edge feature for GSS^\bullet should occur at higher energy than that of GS^\bullet . This is because the acceptor orbital in the perthiyl species is a higher energy antibonding orbital. In addition, a splitting of the pre-edge feature in GSS^\bullet is expected from the DFT results.

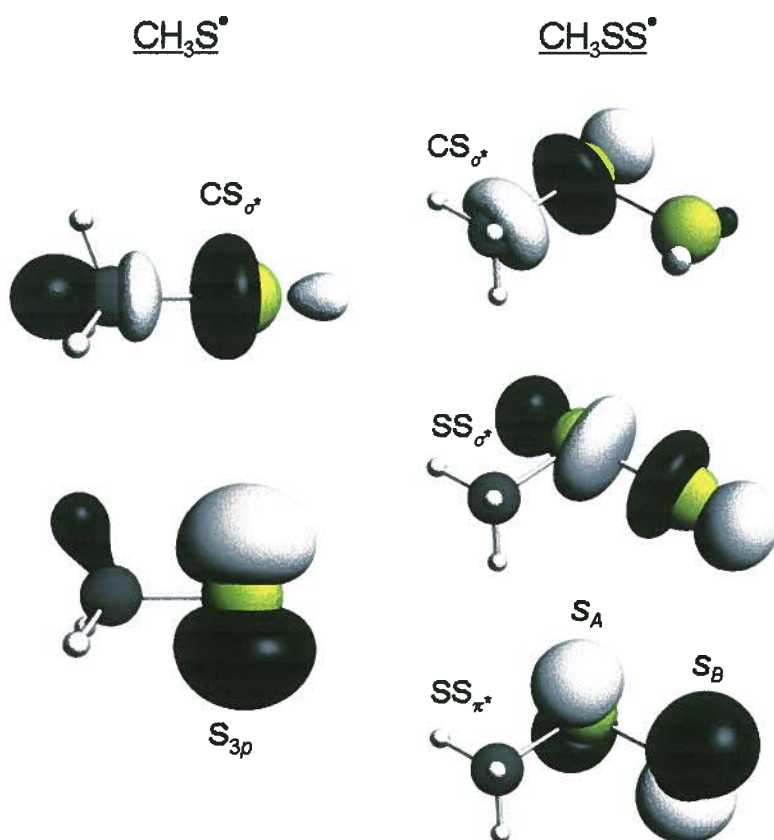


Figure 4.2.6 DFT calculated electron density contour maps of important valence orbitals for thiyl and perthiyl radicals (Isovalue = $0.075e \cdot \text{\AA}^{-3}$).

Table 4.2.2. TD-DFT calculated sulfur K-edge pre-edge features of relevant model compounds. The resulting excitation energies for the sulfur 1s electrons were shifted by +76.5eV in all cases, using the main σ^* feature of GSH as a calibration point.

Species	Assignment	Energy (eV)	<i>f</i>
CH ₃ SH	CS σ^* +HS σ^* ←S _{1s}	2472.8	2.0×10 ⁻³
	CS σ^* ←S _{1s}	2473.7	1.1×10 ⁻³
	CS σ^* +HS σ^* ←S _{1s}	2474.4	1.3×10 ⁻³
CH ₃ S [•]	S _{3p} ←S _{1s}	2468.8	3.9×10 ⁻³
	HC σ^* ←S _{1s}	2473.7	8.1×10 ⁻⁴
	CS σ^* ←S _{1s}	2474.5	9.3×10 ⁻⁴
CH ₃ SS [•]	SS π^* ←S _{1s} ^B	2469.3	2.5×10 ⁻³
	SS π^* ←S _{1s} ^A	2470.6	1.8×10 ⁻³
	SS σ^* ←S _{1s} ^B	2472.7	3.1×10 ⁻³
	CS σ^* ←S _{1s} ^B	2473.4	5.3×10 ⁻⁴
	SS σ^* ←S _{1s} ^A	2474.1	2.6×10 ⁻³
	CS σ^* ←S _{1s} ^A	2474.8	1.6×10 ⁻³

The DFT data is in good agreement with the experimental sulfur K-edge spectra. The lowest energy pre-edge feature in the UV irradiated GSH spectra was assigned to a S_{3p}←S_{1s} transition in GS[•] while the feature at 2470.5eV was attributed to the SS π^* transitions of GSS[•]. The GSS[•] pre-edge feature was fitted using PeakFit v4.12 (figure 4.2.7) and the splitting caused by differences in Z_{eff} of the two sulfur atoms, is similar to that predicted by DFT (~1.1eV vs. 1.3eV). The kinetic behavior of the sulfur K-edge pre-edge features are also consistent with previously published EPR data, showing initial formation of the thiyl radical followed by subsequent formation of the longer-lived perthiyl species¹⁴⁶. Radical yields were estimated using the ratios of DFT predicted oscillator strengths (*f*) for pre-edge features of the methyl thiyl (CH₃S[•]) and methyl perthiyl (CH₃SS[•]) radicals with that of methane thiol (CH₃SH). This allowed the extrapolation of the value for the areas of the radical species corresponding to a 100% thiyl or perthiyl XAS spectrum. The calculated areas corresponding to 100% of a species were then compared to the actual areas achieved at the different irradiation times to calculate the percent radical yields. Maximum yields for the thiyl and perthiyl radical were achieved after irradiating the sample for 4 hours (~0.45%) and 48 hours (~3.1%), respectively (figure 4.2.5).

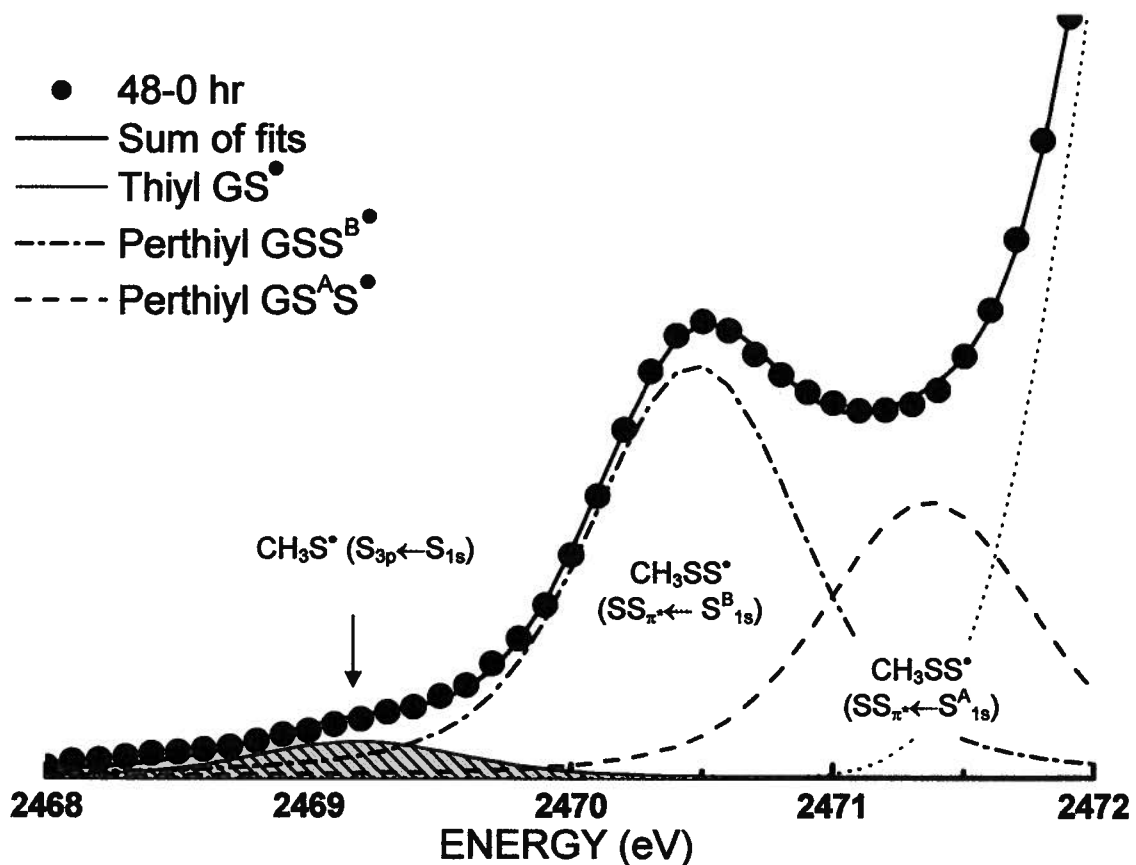


Figure 4.2.7 Peak fitting of the difference spectra for the pre-edge region of the GSH sample irradiated for 48 hours and control (0 hours). The peak ratios for the two perthiyl radical pre-edge features were kept within 20% of the DFT calculated result. Pseudo-voigt functions with 50% lorentzian and 50% gaussian character were used for each of the fitted peaks.

4.3 CONCLUSION

This study shows the usefulness of XAS as a probe to detect sulfur based radical intermediates and was the first study to detect and characterize isolated free sulfur radicals using XAS. Within the same model system it is possible to differentiate between two sulfur radical intermediates GS^\bullet and GSS^\bullet , which had pre-edge features well resolved from each other and the intense σ^* contributions. An EPR silent byproduct of the photo-chemical reaction described by the peak at 2482.6eV was also identified. This feature is indicative of a highly oxidized sulfur species possibly a sulfoxyl radical intermediate or a sulfonic acid. In the following sections this technique is applied to increasingly more complicated systems and reactivity profiles, which prove the usefulness of this technique when used in conjunction with more main stream spectroscopies such as EPR and NMR.

5 Perthiyl Radical and Disulfide Bond Formation in Photo-irradiated Nitrosoglutathione and Lipoic Acid

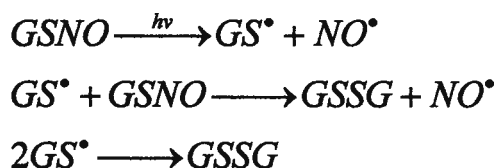
5.1 BACKGROUND

The initial study involving glutathione (GSH, chapter 4) showed that XAS can be very useful in the detection of sulfur based radicals, which have low energy pre-edge features well separated from the typical spectroscopic features of non-radical species. Nitrosoglutathione (GSNO), the S-nitrosylated version of glutathione, and lipoic acid (LA), the oxidized disulfide of dihydrolipoic acid (DHLA), are low molecular weight thiols which are also involved in antioxidant defense as previously described. In fact, DHLA is involved in the denitrosation of GSNO to yield LA and the free thiol GSH⁷⁷. The reaction is believed to proceed via transfer of the NO[•] moiety to DHLA followed by the formation of an internal disulfide and release of NO[•]. Sulfur K-edge studies with *in situ* photo-irradiation show formation of new disulfide bonds in GSNO and formation of an additional pre-edge feature attributed to the perthiyl radical. The transition assigned to the perthiyl radical is also present in LA. EPR and NMR techniques were applied to better understand the reactivity of these species and complement the XAS experiment. Even though these systems have been previously investigated there is still some debate to their mechanism of action. Furthermore, their reactivity seems to be very dependent on the reaction conditions¹⁵⁰⁻¹⁵⁴. If XAS is to be applied to more complicated reaction profiles such as those of enzymes, the reactivity of simpler systems and the conditions that govern them must first be investigated.

S-nitroso glutathione (GSNO)

The main function of GSNO is as an NO[•] carrier and delivery system, NO[•] being an essential signaling molecule. The mechanism of NO[•] delivery is still under investigation and most recent studies suggest that at neutral pH NO[•] is released from nitrosoglutathione by a one electron reduction mechanism involving a possible GSNO^{•-} intermediate¹⁵⁵. Still, other research emphasizes the importance of disulfide bond formation during NO[•] release as a result of denitrosation reactions, such as those involving DHLA and thioredoxin to give the corresponding lipoic acid and oxidized

thioredoxin products⁷⁷. Nitrosothiol (RSNO) decomposition accompanied by release of NO[•] and formation of disulfides is also catalyzed by the presence of copper (Cu⁺), application of heat and photo-irradiation¹⁵⁶. Based on previous experiments with GSH, GSNO decomposition can be observed with sulfur K-edge XAS and *in situ* photo-irradiation of the sample. Initial formation of the GS[•] intermediate should be followed by disulfide bond formation (GSSG) and be proceeded by the disappearance of features due to the GSNO starting material (scheme 5.1.1)¹⁵².



Scheme 5.1.1 GSNO photo-reactivity induced reaction pathways.

The sulfur K-edge spectrum of GSNO was previously investigated and assigned by Szilagyi and coworkers; our data are consistent with this previous work (figure 5.1.1)¹⁴. The dominant features are the SN_π*←S_{1s} at 2471.7eV and the SN_σ*←S_{1s} transitions at 2473.4eV due to the S-NO bond and the SC_σ*←S_{1s} feature at 2474.8eV. This assignment is reinforced further by TD-DFT simulation of the core S_{1s} bound transitions of CH₃CH₂SNO model system which indicates two SC_σ*←S_{1s} transitions account for the feature at 2472.8eV, while a single transition is observed for the SN_σ*←S_{1s} feature. The SN_σ* acceptor orbital for the SN_π*←S_{1s} at 2471.7eV shows a significant interaction between the p orbitals of all atoms making up the S-N-O bonding manifold (figure 5.1.2). This is consistent with an S-NO bonding model stabilized by resonance as previously described, with the most significant contribution being due to the S-N_σ resonance structure followed by S-N_π and S⁺NO⁻ ion pair¹⁵⁷. Therefore, in a series of S-nitrosothiols the intensity of the SN_π*←S_{1s} and SN_σ*←S_{1s} transitions could be used to determine the relative importance of the S-N_π resonance structure, a project which is currently ongoing in the Kennepohl group.

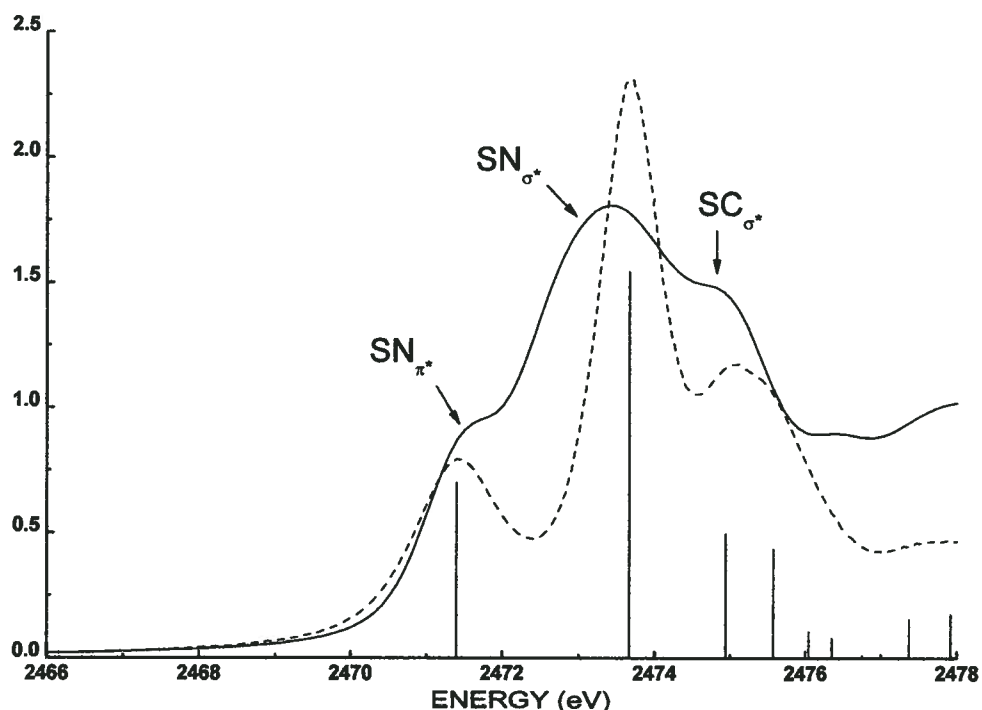


Figure 5.1.1 GSNO sulfur K-edge XAS spectrum (solid line) with the main S_{1s} core excitation transitions assigned¹⁴. The edge jump of the spectra was normalized to 1. TD-DFT simulated XAS spectrum of GSNO using CH_3CH_2SNO as a model system (dotted line).

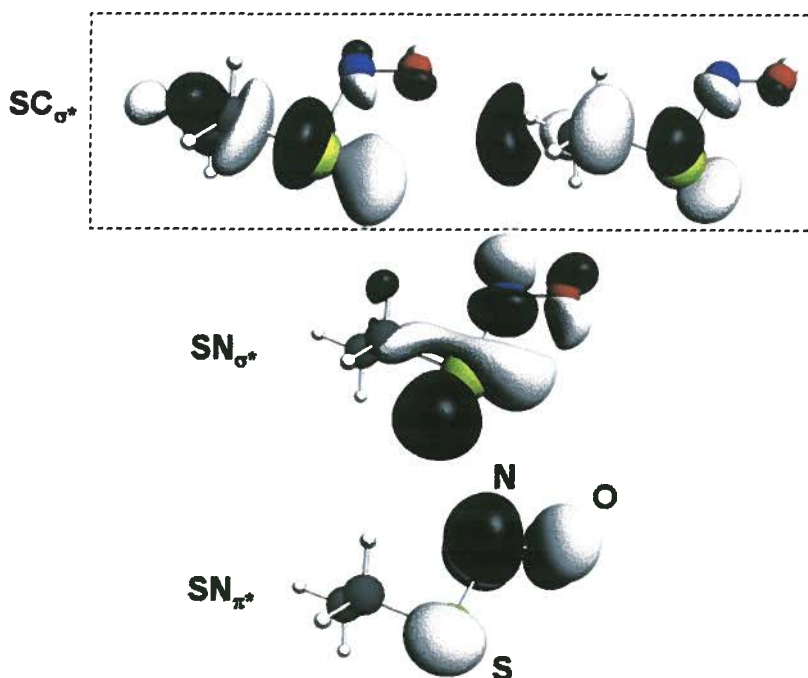
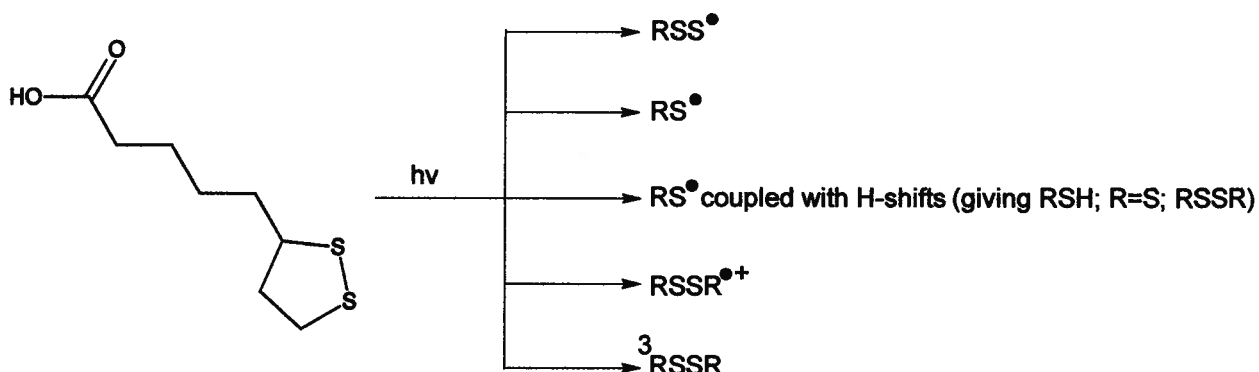


Figure 5.1.2 DFT calculated electron density contour maps of important empty valence orbitals for CH_3CH_2SNO (Isovalue = $0.05e\cdot\text{\AA}^{-3}$).

Lipoic acid (LA)

Lipoic acid is an important cofactor and antioxidant. The LA/DHLA redox couple is distinguished from that of other low molecular weight thiols by its ability to function as an antioxidant in both hydrophilic and lipophilic environments and even reduce other antioxidants such as glutathione^{23, 25}. In addition, LA can be further oxidized to give a disulfide radical cation¹⁵⁴. The photochemical reactivity of LA was previously investigated. Depending on the conditions the presence of thiyl radicals, perthiyl radicals, disulfide radical cations, and triplet states were detected, making LA a versatile system to observe by XAS. Photolysis of disulfides in solution results in the formation of perthiyl radicals¹⁴⁹. This reaction is more favourable with increased substitution of the resulting carbon radical which further stabilizes it^{150, 151}. The presence of oxygen during photolysis seems to facilitate thiyl radical formation¹⁵⁰. Cage effects also impact photolysis. The hexacyclic disulfide *trans*-4,5-dihydroxy-1,2-dithiacyclohexane when irradiated (wavelengths between 305-410nm) near its absorbance maximum at 280nm (the absorbance spans the 250-325nm range) forms a thiyl radical pair which is proposed to undergo H shifts to form more stable products, including the formation of the starting material¹⁵³. Laser flash photolysis of LA at 266nm in aqueous solution results in the formation of the disulfide radical cation, while flash photolysis at 355nm yields a triplet state with a lifetime of 75ns¹⁵⁴. Therefore, irradiation of LA under anaerobic condition with a Xe arc lamp would be expected to give a combination of the perthiyl radical, thiyl radical or disulfide radical cation intermediates (scheme 5.1.2).



Scheme 5.1.2 LA photo-reactivity induced products.

The transitions of the sulfur K-edge XAS spectrum (figure 5.1.3) of LA were previously investigated¹⁵. The first and most intense pre-edge feature corresponds to the

$SS_{\sigma^*} \leftarrow S_{1s}$ at 2472.3eV followed by the $SC_{\sigma^*} \leftarrow S_{1s}$ at 2473.9eV. TD-DFT simulated XAS spectra for the bound transitions of methyl disulfide (CH_3SSCH_3) is consistent with this assignment (figure 5.1.3). The feature labeled LA_1 at 2475.4eV in figure 5.1.3 is attributed to a collapse in symmetry between the sulfurs of LA due to bonding to a primary carbon in one case and a secondary carbon in the other. This feature is not present in symmetric disulfide systems¹⁵. The steric strain in the pentacyclo LA disulfide is emphasized by a lowering in energy of both the SS_{σ^*} and SC_{σ^*} when compared to cystine where these features appear at ~2472.6eV and ~2474.2eV respectively¹⁵. This suggests that weaker bonds than generally found in disulfides result in LA due to steric strain. The XAS of LA also exhibits broader features which could be do to self-absorption effects from non-homogenous grinding of the solid sample¹⁵⁸. However, the intensities of the features are consistent from run to run and comparable to those of other researchers¹⁵ indicating that self-absorption should be minimal. Furthermore the features of the spectra are well resolved and self-absorption should not pose a significant problem for determining the energy of the various transitions of the spectra.

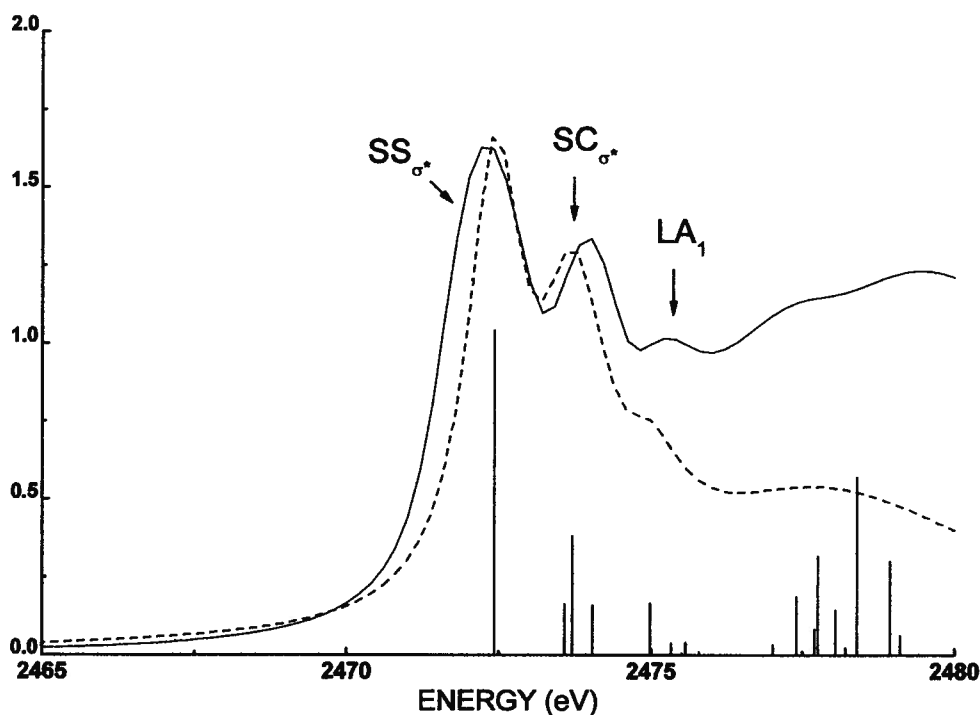


Figure 5.1.3 LA sulfur K-edge XAS spectrum (solid line) with the main S_{1s} core excitation transitions assigned¹⁵. The edge jump of the spectra was normalized to 1. TD-DFT simulated XAS spectrum of LA using CH_3SSCH_3 as a model system (dotted line).

Previous assignments of the features from the sulfur K-edge XAS of GSNO and LA give an idea of which features are most important to observe in the irradiation studies. Disappearance of the $SN_{\pi^*} \leftarrow S_{1s}$ and $SN_{\sigma^*} \leftarrow S_{1s}$ transitions in GSNO would indicate breakage of the S-NO bond, while a decrease in intensity of the $SS_{\sigma^*} \leftarrow S_{1s}$ in LA would suggest bond homolysis. Previously determined reaction pathways helped to explain the reactivity observed. It was found that although LA and GSNO are “simple”, small sulfur containing compounds their reactivity can be quite complex, and under the experimental conditions, even related.

5.2 RESULTS AND DISCUSSION

Photo-irradiation of LA

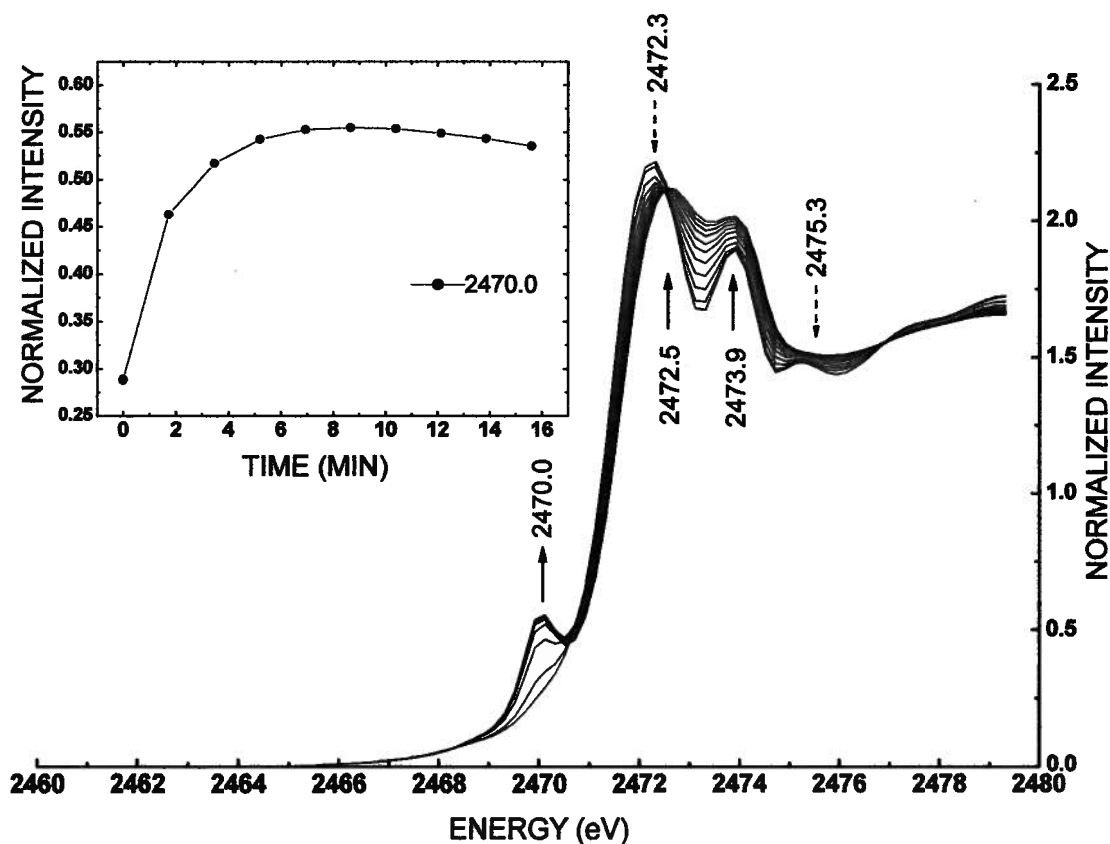


Figure 5.2.1 LA sulfur K-edge XAS spectrum with *in situ* photo-irradiation. Dotted arrows are decreasing features, solid arrows are growing features. Subset: Formation of the feature at 2470.0eV attributed to the perthiyl radical.

Irradiation of LA with a Xe arc lamp under anaerobic conditions was followed with sulfur K-edge XAS. In this system the starting compound is a strained cyclic disulfide and as displayed in figure 5.2.1 a feature at 2470.0eV appears after only a few minutes of irradiation. For LA a shift is also seen coupled with a drop in intensity of the feature at 2472.3eV corresponding to the breaking of the cyclic disulfide. However, formation of a feature at 2472.5eV and an increase in intensity at 2473.9eV with a 1.5eV separation between the two is suggestive of new disulfide bonds forming, along with perhaps other minor products. The higher energies lead to the conclusion that the forming disulfides have stronger bonds resulting from a less strained conformation. The disappearance of the peak at 2475.3eV indicates that if new disulfides are being formed they have sulfurs with similar core excitation energies. Unfortunately, the product from the irradiation forms a white insoluble precipitate which does not lend itself to easy characterization by other spectroscopic techniques such as NMR, and confirmation and characterization of the final product formed from the irradiation is still unclear.

To confirm the presence of the perthiyl radical, EPR spectra of anaerobically irradiated LA were collected and analyzed. The formation of the perthiyl radical was clearly visible (figure 5.2.2). A rhombic signal was observed with irradiation at 195K and 77K with g-values of 2.002, 2.026 and 2.062 matching well the simulated EPR spectrum of the perthiyl radical and the density functional theory calculated values for the $\text{CH}_3\text{SS}^\bullet$ perthiyl radical (2.058, 2.027 and 2.002)¹⁴⁶. Table 5.2.1 shows half power saturation values ($P_{1/2}$) which represent the value at which the signal intensity divided by the square root of power drops by 50%. Analysis shows that the features between 2.026 and 2.002, as well as those below 2.000, saturate at low powers suggesting they are due to carbon centered radicals¹⁴⁹. Perthiyl radicals however like most sulfur centered radicals saturate at higher powers and their intensity increases with microwave power over the ranges investigated, overwhelming the spectra from other species (figure 5.2.3)^{146, 149}. The feature due to the perthiyl radical at $g=2.062$ is well resolved from other peaks and has a $P_{1/2}$ of 20mW, consistent with previously reported values¹⁴⁶. The features due to the perthiyl at 2.026 and 2.002 overlap features with low saturation powers (2.026 to 2.002 and below 2.002), which might explain why they have lower $P_{1/2}$ values (6mw vs. 20mW). $P_{1/2}$ values of carbon radical species were found to lie in the 0.6mW range which is consistent with previously reported values ($\sim 1\text{mW}$)¹⁴⁶. LA shows a similar reactivity profile when dissolved in D_2O as in the solid state.

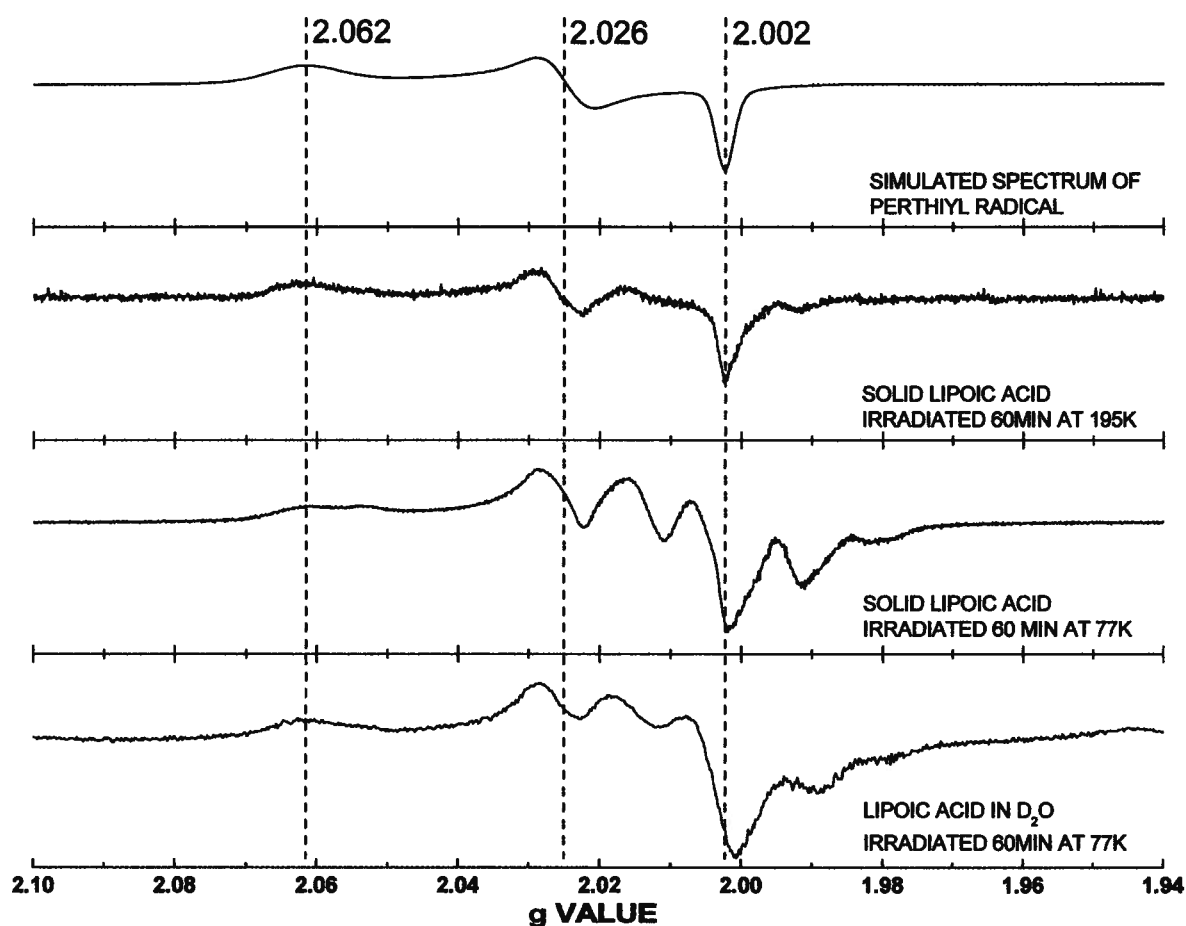


Figure 5.2.2 EPR of irradiated (60min) LA under different conditions (microwave power 0.6mW, modulation frequency 50MHz, modulation amplitude 3.0G, 5 scans) and simulation of the spectrum for the perthiyl radical with g values of 2.062, 2.026 and 2.002.

Table 5.2.1 Half power saturation values for EPR spectra of solid LA irradiated at 77K (as in figure 5.2.3).

g VALUE RANGE	P_{1/2} mW SATURATION
2.062	20
2.026	6
2.026 – 2.002	0.6
2.002	6
2.00-1.95	0.6

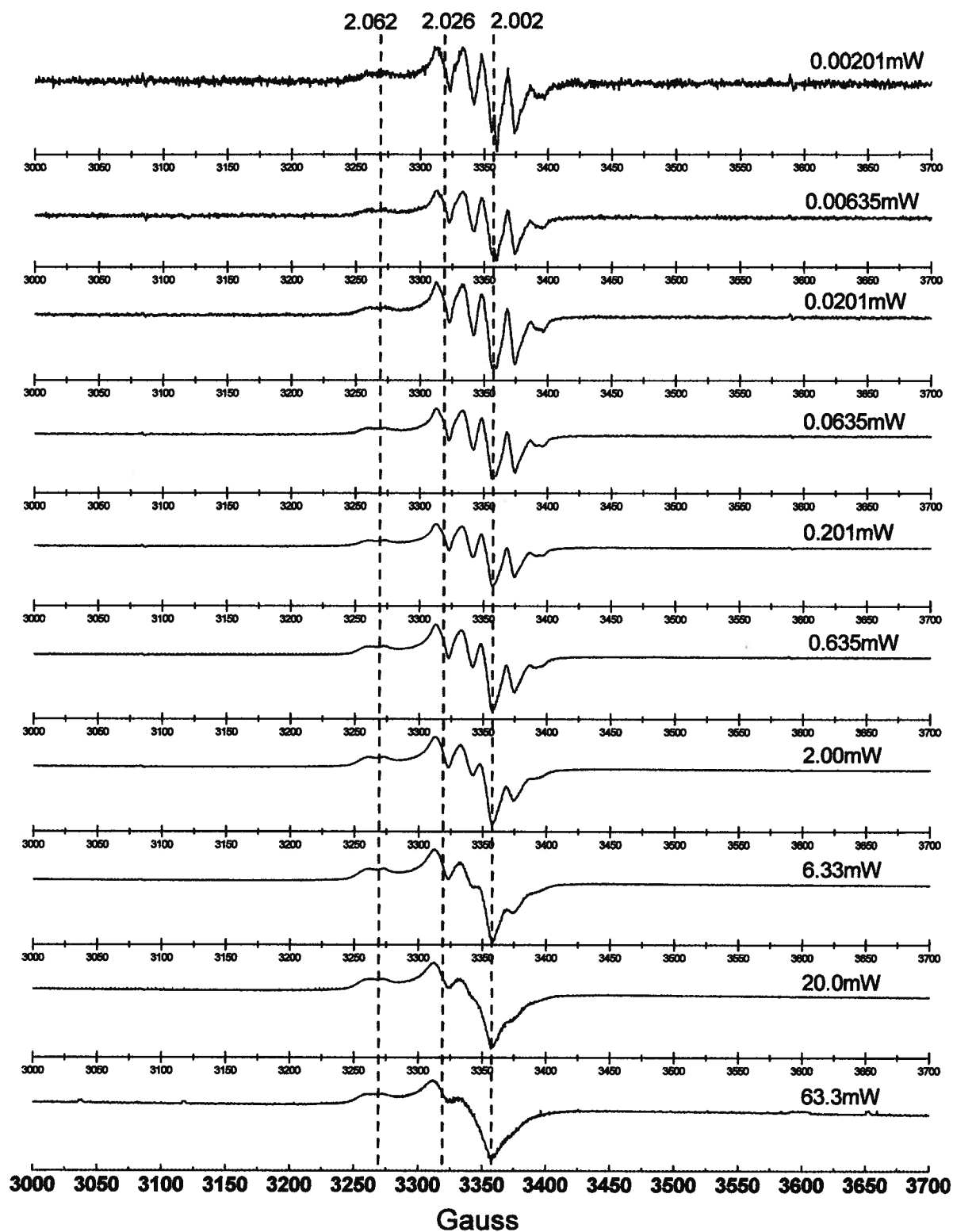


Figure 5.2.3 EPR power saturation study of irradiated (60 min) LA solid at 77K. Microwave powers were increased between 0.002mW and 63.3mW. Perthiyl radical at g values of 2.062, 2.026 and 2.002 is found to increase with increasing microwave powers; (modulation frequency 50MHz, modulation amplitude 3G, 10scans).

Photo-irradiation of GSNO

Over the duration of 1 hour, irradiation caused the features in GSNO due to the S-NO bond to disappear as highlighted by the dotted arrows in figure 5.2.4. Of particular importance is the peak at 2471.6eV, which is well resolved from other features and allows one to easily follow the breaking of the S-N bond. Under the conditions of the experiment some minor products indicative of oxidized sulfur species form in the 2476.5 – 2477.5eV region where transitions from R_2SO and RSO_2^- may occur and at 2480.8eV indicative of the formation of RSO_3^- ². The transition at 2480.8eV due to RSO_3^- is also present in the initial spectrum, showing that it is formed as a minor product during GSNO synthesis. Appearance of features at 2472.8eV and 2474.0eV during irradiation, suggest the formation of disulfide bonds and correspond to $SS_{\sigma^*} \leftarrow S_{1s}$ and $SC_{\sigma^*} \leftarrow S_{1s}$ excitations^{2, 15}. They are split by 1.2eV and the higher intensity of the first feature over the second further suggests the presence of disulfide bond formation. However, the $SS_{\sigma^*} \leftarrow S_{1s}$ and $SC_{\sigma^*} \leftarrow S_{1s}$ transitions in disulfide bonds are generally separated by 1.5eV. The poor resolution of the separation between the $SS_{\sigma^*} \leftarrow S_{1s}$ and $SC_{\sigma^*} \leftarrow S_{1s}$ transitions indicates the presence of other species whose features are overlapping those of the forming disulfides and could be due to minor products. A small shoulder forming at 2470.2eV is consistent with the formation of a perthiyl radical, and forms congruently with S-N bond cleavage reaching a steady state when about half the GSNO is reacted (figure 5.2.5). The rate of perthiyl radical formation and the fact that it reaches a steady state is consistent with previously observed behavior of perthiyl radicals generated in both GSH and LA experiments. It is not clear from the XAS data by what mechanism the perthiyl radical is formed, but the presence of features from disulfide bonds suggests a possible secondary process, such as disulfide bond formation followed by S-C bond homolysis resulting in a perthiyl radical. To further investigate this, EPR data was acquired to determine the time of perthiyl radical generation and NMR data was used to confirm disulfide bond formation.

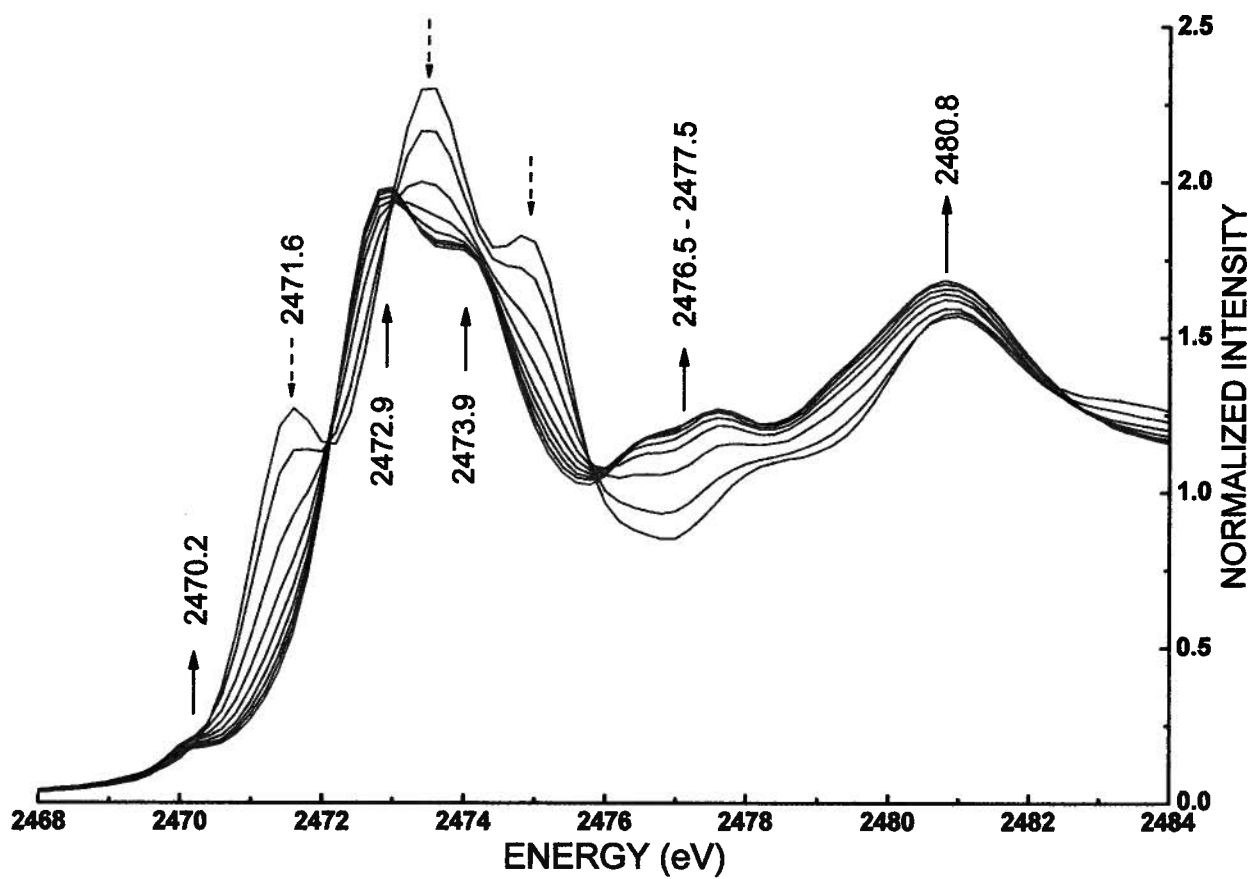


Figure 5.2.4 GSNO sulfur K-edge XAS spectrum with *in situ* photo-irradiation. Dotted arrows are decreasing features, solid arrows are growing features.

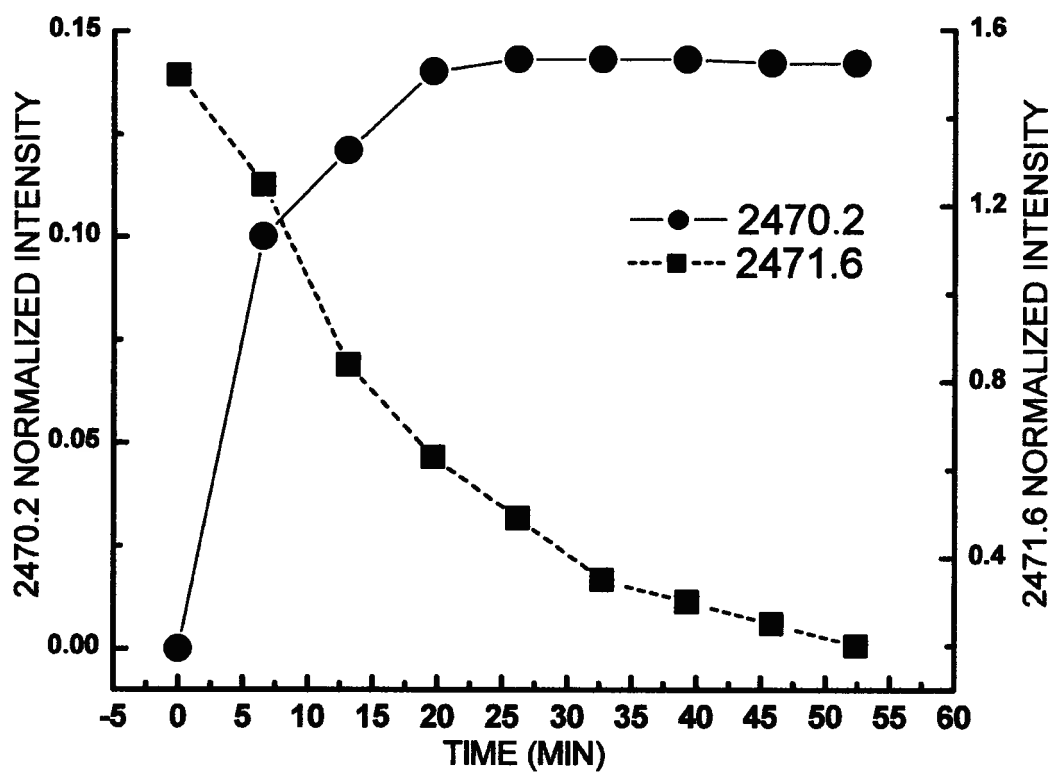


Figure 5.2.5 Time evolution of the intensities from sulfur K-edge XAS spectra of the feature at 2471.6, indicating disappearance of the S-NO bond, and the feature at 2470.2, indicating the appearance of the perthiyl radical, during *in situ* photo-irradiation of GSNO.

Irradiation of GSNO at 195K or 77K, both as a solid or dissolved in D₂O, yields a similar EPR signal, suggesting that S-NO bond photo-cleavage is not sensitive to sample preparation under the conditions of this experiment. The most striking characteristic of the EPR spectra of irradiated GSNO is the absence of features due to the perthiyl radical such as those that would be expected at a $g \sim 2.06$ (figure 5.2.6). The inflection point at 2.012 may suggest the presence of thiyl radicals, but a clear identification is not possible because of overlapping features with similar power saturation profiles.

However, formation of the GSSG disulfide from photo-irradiated GSNO under anaerobic conditions at 77K and 195K as well as GSNO irradiated at room temperature was detected by NMR and is in fact the major product. Low levels of GSSG are present in our GSNO samples due to sample decomposition as illustrated in figure 5.2.7. The NMR of GSNO has features at 2.15ppm (2H, m), 2.47ppm (2H, t) and 3.85ppm (1H, t) due to the glutamyl β , γ and α protons respectively. This is followed by a singlet at 3.98ppm due to the glycyI protons which sits on top of the signals at 4.13ppm (1H, m) and 3.99ppm (1H, m) from the cysteine β protons, followed by the cysteine α proton at 4.68ppm (1H, t)¹⁵⁹. GSSG formation can be followed by observing the doublet of doublets at 3.0ppm and 3.3ppm due to the cysteine β protons as well as the triplet at 2.6ppm due to the glutamyl γ protons (dotted square figure 5.2.7)¹⁶⁰. After irradiation at 77K for 1 hour the GSNO sample whose EPR spectra is shown in figure 5.2.6 was brought to room temperature and the NMR was acquired. The initial control NMR shows a ratio of 10:3 GSNO to GSSG, derived from the relative peak integrations. After irradiation the GSSG features increase in intensity leading to a 2:1 ratio GSNO to GSSG. The sample was further irradiated at room temperature for 5 minutes to facilitate full conversion of GSNO to the disulfide GSSG. The newly formed GSSG was then used to determine if perthiyl radical generation would occur with further irradiation at 77K.

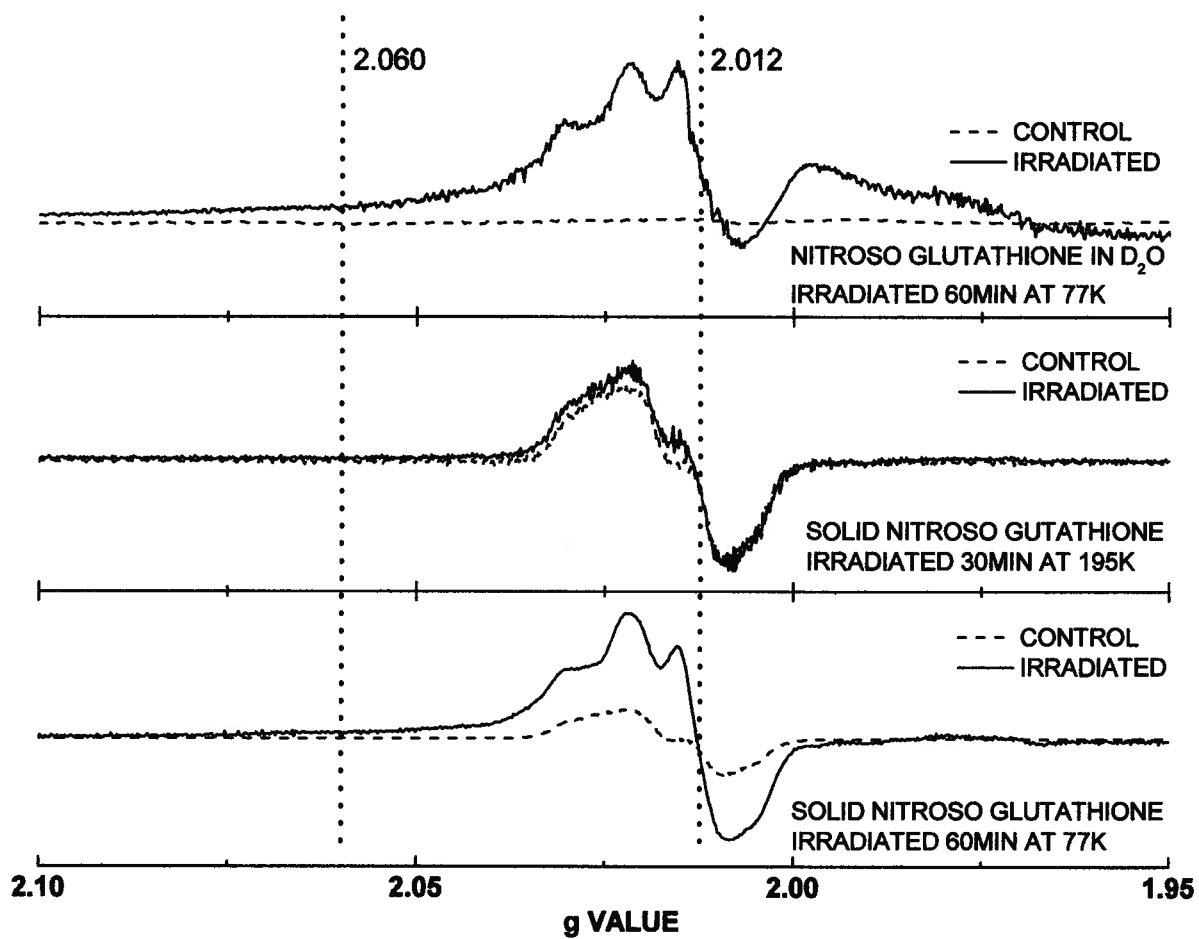


Figure 5.2.6 EPR of GSNO irradiated under different conditions. No clear detection of sulfur based radicals; (microwave power 0.6mW, modulation frequency 50MHz, modulation amplitude 3.0G, 5 scans).

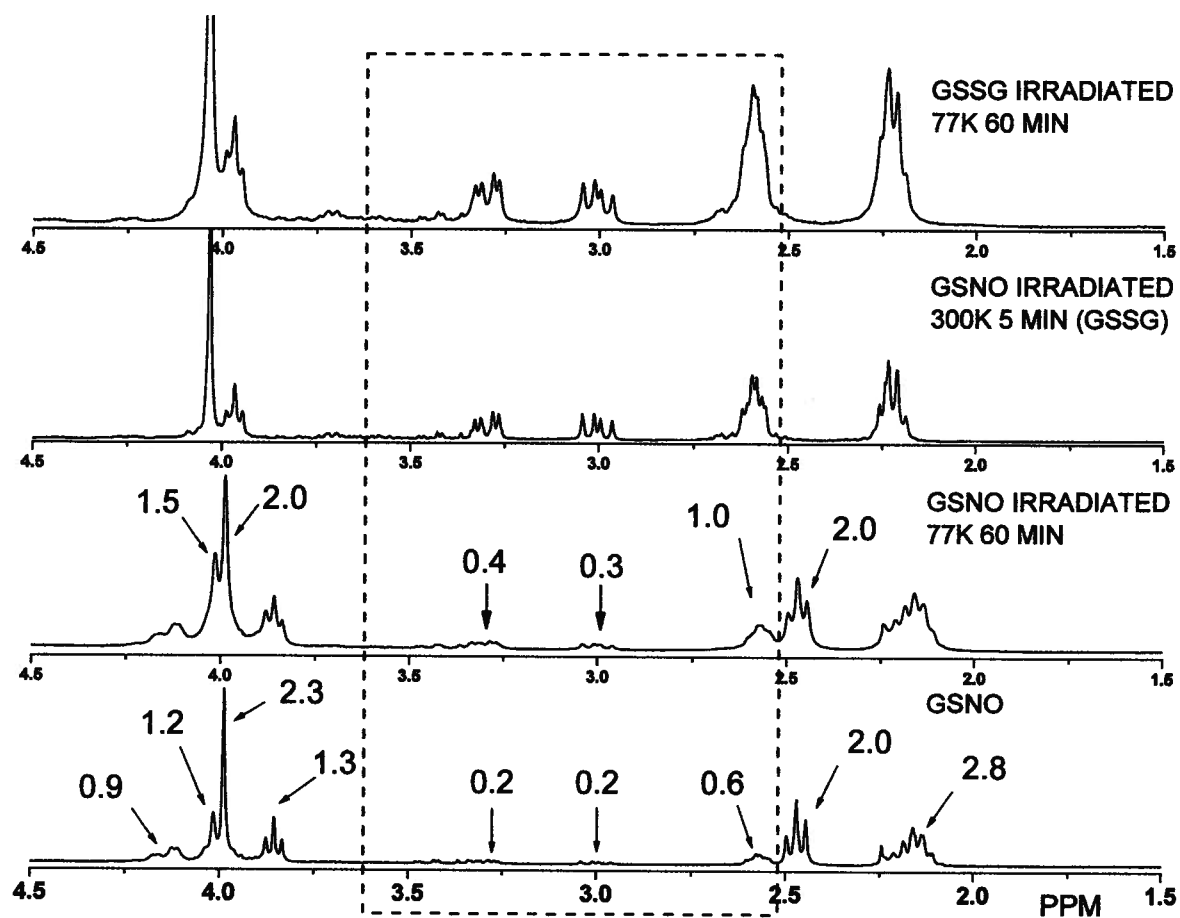


Figure 5.2.7 Comparison of NMR spectra from samples of GSNO and GSSG in D_2O . Dotted rectangle encloses features due to the presence of GSSG.

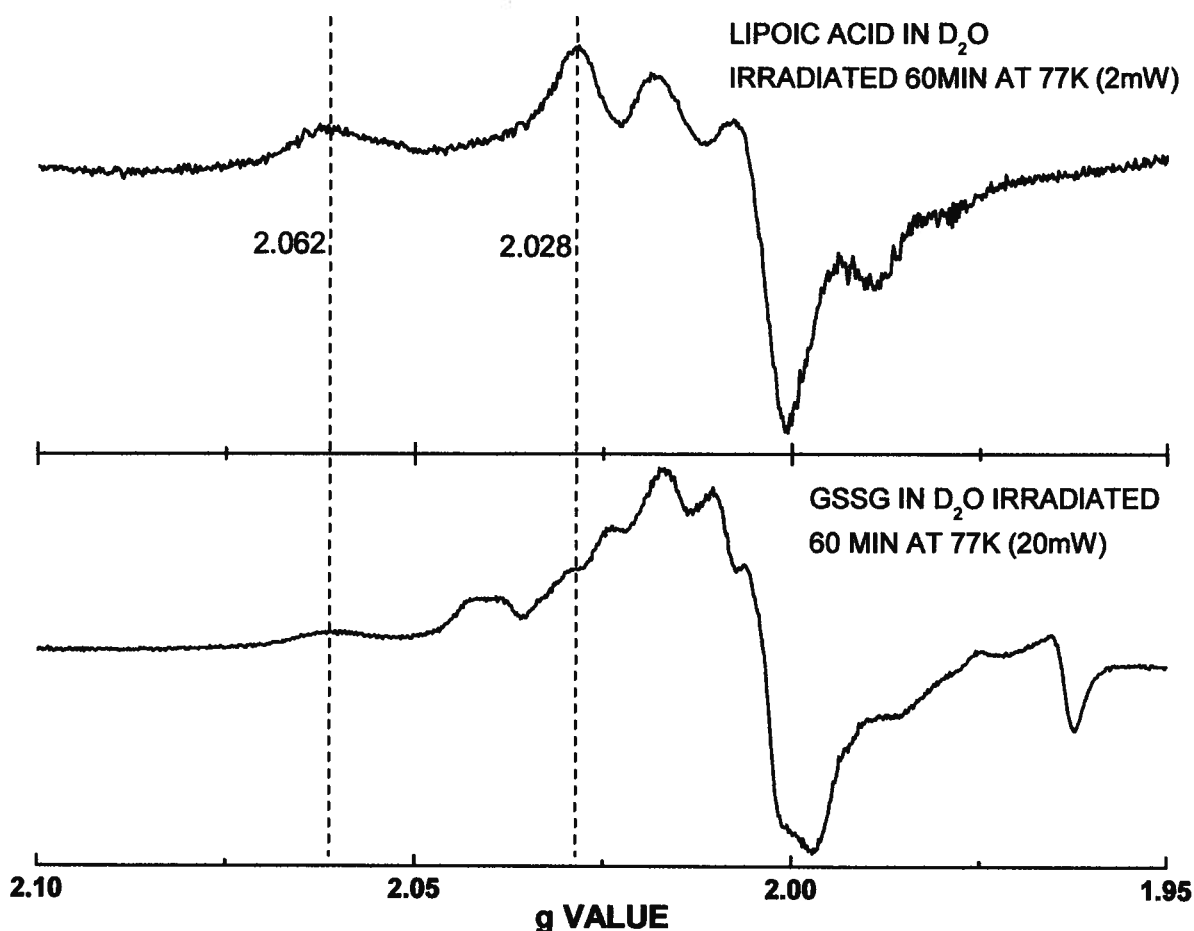


Figure 5.2.8 Comparison of EPR from irradiated GSSG and LA showing the presence of perthiyl radicals; (modulation frequency 50MHz, modulation amplitude 3.0G, 5 scans).

Irradiation of the GSSG sample in D₂O at 77K gives a rich EPR spectrum (figure 5.2.8). When the EPR spectra of irradiated GSSG in D₂O is compared with that of LA in D₂O the feature attributed to the perthiyl radical at $g \sim 2.062$ is present in both samples. Furthermore, a shoulder at 2.028 in the spectrum of irradiated GSSG corresponds to the peak maximum of the perthiyl feature in irradiated LA. This is also confirmed by power saturation studies that show the feature at 2.062 has a $P_{1/2}$ greater than 20mW and a linear saturation profile in the 0.002mW to 6mW range (figure 5.2.9). This is similar to the perthiyl radical behavior seen in both irradiated GSH and LA. The perthiyl radical yield under the conditions investigated is very low as evidenced by the weak EPR signal. This is mirrored by the XAS experiment, where the peak at 2470.2eV has a very low intensity. It is important to note that after 60 minutes of irradiation the NMR of the GSSG sample is still dominated by the disulfide features (figure 5.2.7).

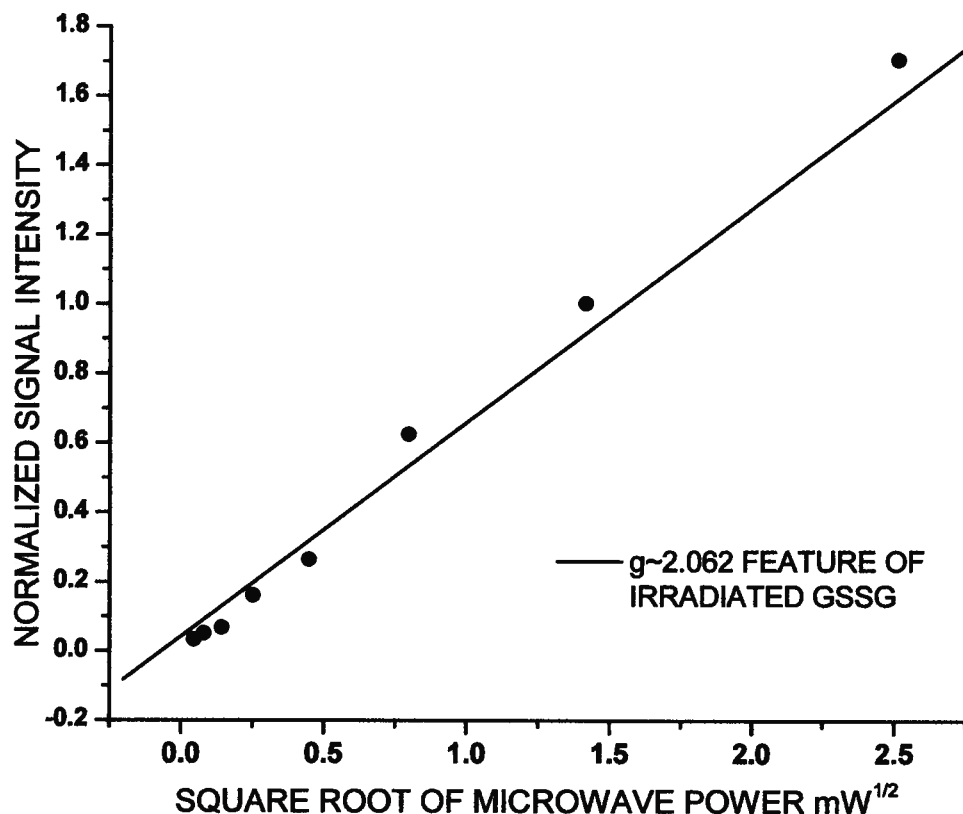


Figure 5.2.9 Power saturation study of irradiated GSSG feature at $g \sim 2.062$ attributed to the perthiyl radical; (modulation frequency 50MHz, modulation amplitude 3.0G, 5 scans).

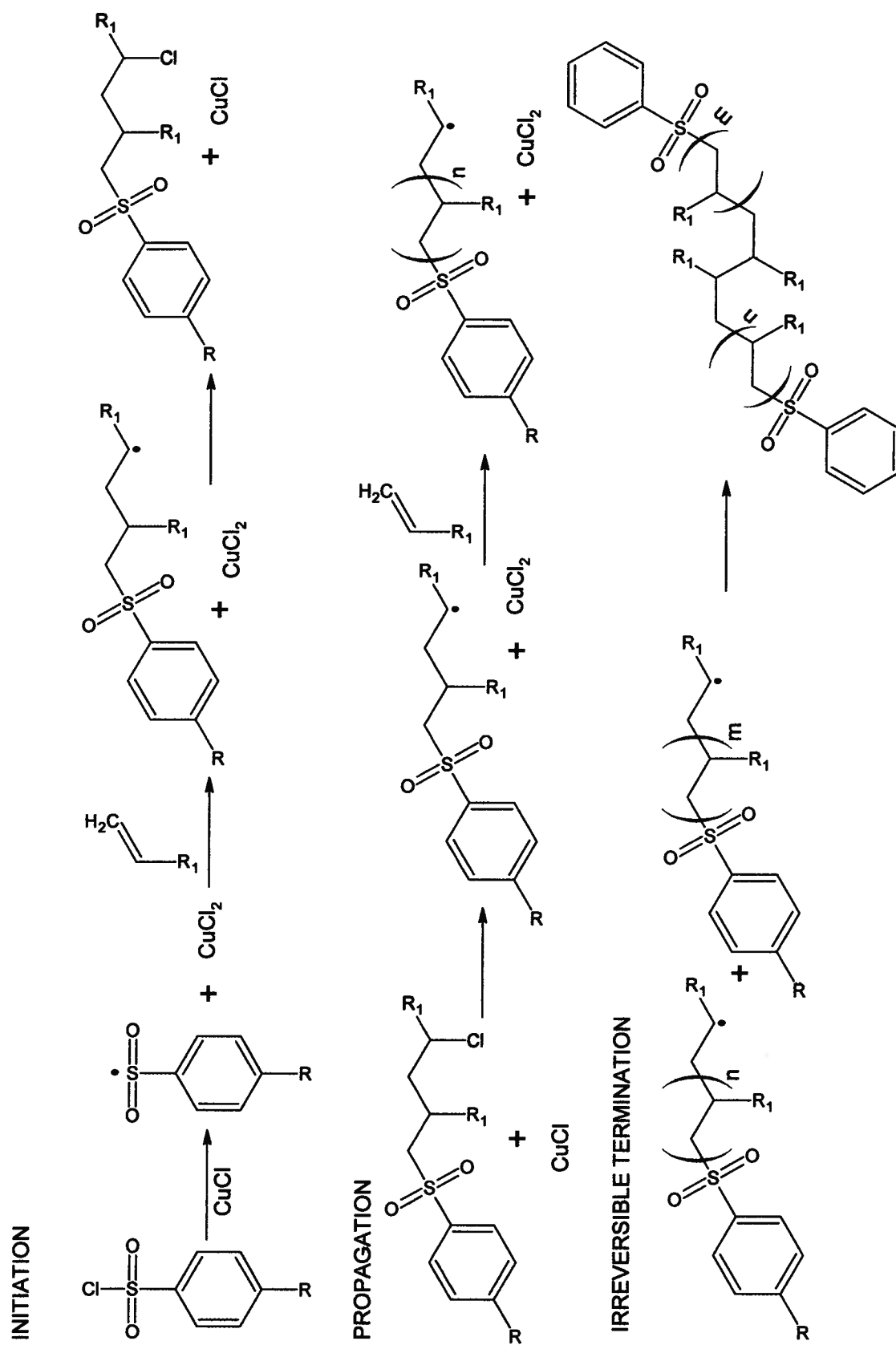
5.3 CONCLUSION

XAS spectra of irradiated GSNO and LA under He atmosphere indicate the formation of the perthiyl radical at $\sim 2470.0\text{eV}$. The presence of the perthiyl radical was clearly shown in the EPR spectra of irradiated LA; however it is proposed that GSNO must first react to form GSSG before being able to account for the perthiyl radical signal in its XAS spectrum. Formation of GSSG from irradiated GSNO is indicated by the XAS spectra as evidenced by the disappearance of the features due to the S-NO bond and formation of new peaks at 2472.8eV and 2474.0eV . This was confirmed with NMR where the transition from GSNO to GSSG (figure 5.2.7) occurs with little or no side products. Further irradiation of the sample resulted in formation of a small amount of perthiyl radical giving rise to a weak EPR signal. XAS of irradiated GSNO therefore shows both the formation of GSSG along with the weak signal due to the perthiyl radical $\text{SS}_{\pi^*} \leftarrow \text{S}_{1s}$ transition.

6 Effects of Hyperconjugation on the Electronic Structure and Photo-reactivity of Organic Sulfonyl Chlorides

6.1 BACKGROUND

The electronic structure of p-toluene sulfonyl chloride and related organic sulfones has generated some attention because of its role as an initiator in living radical polymerization reactions (scheme 6.1.1)^{161, 162}. Living radical polymerization is characterized by a faster initiation step than the following propagation reactions and a minimization of termination processes, resulting in a narrower polydispersity index^{162, 163}. This is achieved by the presence of actively propagating species due to the persistent radical effect¹⁶⁴. Seen from the perspective of the polymerization reactions involving sulfonyl chloride, this effect can be explained as follows. The S-Cl bond of the sulfonyl chloride is catalytically broken by CuCl/bpy (bpy = 2,2'-bipyridine) to give the sulfonyl radical and the corresponding CuCl₂ organometallic complex. The sulfonyl radical can further react with the olefinic substrates, which can in turn further polymerize. However, termination events are inhibited by a rise in the concentration of the CuCl₂ complex. As mentioned, initiation results in the formation of the CuCl₂ complex. These complexes can not react with each other so they accumulate. If the growing chains or initiators react with each other ("self terminate"/disproportionate) the concentration of the CuCl₂ complexes will still increase with more initiation events. Further termination steps would involve the reaction of growing polymers (which are free radicals) with CuCl₂ to give a halogenated alkyl, rather than "self termination" simply due to the increase in the concentration of the CuCl₂ complex. However, the now dormant alkyl halides can be reactivated by the CuCl/bpy catalyst. Systems following the persistent radical effect reach a steady state of growing radicals established between the activation and deactivation (propagation and termination) processes. This demands stoichiometric amounts of catalyst to be added for proper reactivity modulation of "capped" dormant alkyl halide chains¹⁶³. The S-Cl bond cleavage in addition to metal reduction can also be initiated by thermolysis or photo-irradiation^{162, 165-167}.

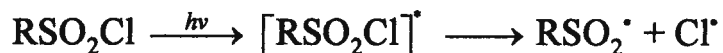


Scheme 6.1.1 Metal catalyzed living radical polymerization with p-toluenesulfonyl chloride as an initiator.

Both aryl and alkyl sulfonyl chlorides (RSO_2Cl) have been termed universal initiators of metal catalyzed living radical polymerization of styrene, methylacrylates and acrylates^{161, 162}. Regardless of the nature of their R group (alkyl/aryl) or electron withdrawing or donating effects of substituted aromatic R groups, the polymerization reactions involving RSO_2Cl result in faster initiation than propagation and narrow polydispersity indices¹⁶¹. This has been attributed to several factors such as the faster formation of sulfonyl radicals vs. carbon centered radicals¹⁶⁸, and the low rate of sulfonyl radical dimerization as compared to carbon radicals^{161, 167}. Most notably they also attributed this universality to a lack of effect of the R group on the reactivity of the sulfonyl radical^{161, 166, 169}. For the aryl compounds this was attributed to poor conjugation between the aromatic ring and the sulfonyl moiety¹⁶⁶. However the rate of oxidation of CuCl_2 by aryl sulfonyl chlorides was shown to be impacted by the substituent on the aromatic ring: electron withdrawing groups at the para-substituted position enhanced copper oxidation¹⁶⁶. Furthermore there is both computational and experimental evidence for hyperconjugation in sulfonyl compounds^{128, 129}. The computational study coupled with X-ray diffraction data for a series of sulfate monoesters, sulfamates, and methanesulfonates shows that the sulfur bonding is highly polarized with the substituents around the sulfur acting both as donor and acceptors resulting in a sulfonyl bonding manifold composed of polar interactions with reciprocal hyperconjugative bonding¹²⁸. Secondly, a bathochromic shift in the benzene UV-Vis absorption is observed when a sulfonyl group is attached to a benzene ring, indicating conjugative mixing between the orbitals of the two moieties¹²⁹.

Therefore, the electronic structure of *p*-toluene sulfonyl chloride (**1a**) and related sulfonyl species (figure 6.2.1) was explored in order to better understand their electronic structure, the importance of hyperconjugation, as well as its impact on sulfonyl radical generation and subsequent radical polymerization. A series of compounds of the form RSO_2G were probed using sulfur K-edge XAS spectroscopy to determine the effect on the SG bond ($\text{G} = -\text{Cl}, -\text{OH}, -\text{alkyl}$) due to the presence of a π system in the R group. In particular, aryl (**a**, $\text{R} = p\text{-XC}_6\text{H}_4\text{-}$, $\text{X} = \text{H/CH}_3$) and alkyl (**b**) R groups were chosen to study the effect of orbital mixing in the sulfonyl centre. Photo-cleavage (scheme 6.1.2) of the S-Cl bond, via irradiation with a Xe arc lamp, was investigated for the sulfonyl chlorides (**1a,b**) and the reactivity was correlated to the hyperconjugative effects

observed. Molecular orbital calculations were carried out to aid in the assignment of spectral features.



Scheme 6.1.2. Sulfonyl chloride photo-cleavage reaction (R= alkyl, p-tolyl).

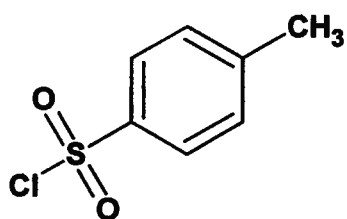
6.2 RESULTS

Sulfur K-edge XAS spectroscopy

The sulfur K-edge XAS spectra of **1-3 a,b** (figure 6.2.1), are shown along with a detailed analysis of simulated spectra in figures 6.2.3 to 6.2.5. The XAS of sodium methane sulfone was used as the model spectrum for **2b** to facilitate analysis of solid samples. The spectra of aqueous methane sulfone¹⁷⁰ and sodium methane sulfone are comparable. The pre-edge regions of the model spectra exhibit clear differences in their features as a function of the R group and substituent G. The aryl compounds (**1-3a**) show additional features not present in the spectra of their alkyl counterparts (**1-3b**). Compound **1a** has three features, two peaks at 2477.4eV and 2481.2eV and a shoulder at 2479.6eV, which is not seen in **1b** where only the peaks at 2477.6 and 2480.9eV are present. The sulfonate **2a** has a main peak at 2481.7eV flanked by two shoulders at 2479.9eV and 2483.9eV. In contrast **2b** has only one shoulder at 2483.1eV in addition to its main peak at 2481.3eV (see figure 6.2.4). Lastly, **3a** exhibits a peak at 2478.6eV in addition to the main absorption feature of the spectrum seen in **3b**. The main absorption feature is also at slightly higher energy in **3a** (2480.6eV) compared to **3b** (2480.1eV). The XAS spectra show that the aromatic ring has a significant effect on the energy and sulfur 3p character of the valence orbitals. This could be due to energy redistribution of the existing transitions in the alkyl compounds, the presence of additional transitions or a combination of the two.

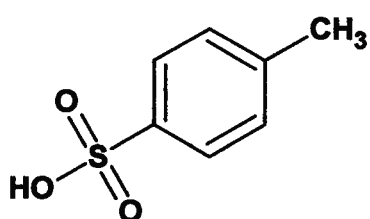
p-Toluene Sulfonyl Chloride

1a



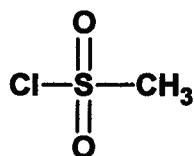
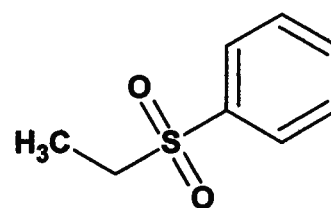
p-Toluene Sulfonic Acid

2a



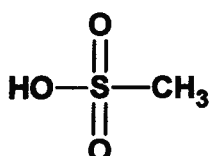
Ethyl Phenyl Sulfone

3a



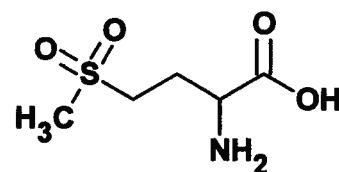
Methane Sulfonyl Chloride

1b



Methane Sulfonate

2b



Methionine Sulfone

3b

Figure 6.2.1 Structures of **1a**. p-toluene sulfonyl chloride; **1b** methane sulfonyl chloride; **2a** p-toluene sulfonic acid; **2b** methane sulfonate; **3a** ethyl phenyl sulfone; **3b** methionine sulfone.

DFT calculations and spectroscopic assignments

Spectral features and electronic transitions were simulated using TD-DFT. Fragment calculations were also carried out on R, SO₂ and G for a better description of the assigned transitions and to assess the effect of the aryl substituent. The relevant transitions and their descriptions are listed in Tables 6.2.1 to 6.2.6 for each of the compounds. The XAS of **3b** was simulated using (CH₃)₂SO₂ as a model compound. It has been previously shown that TD-DFT transitions for (CH₃)₂S are in good agreement with XAS spectra of methionine¹⁵. Two conformational models were evaluated for the simulation of the sulfur K-edge XAS spectra of **3a**. The lower energy conformation (linear) is only ~0.42kJ/mol lower in energy than the higher energy conformation (bent). This low energy barrier suggests that the molecule is able to interconvert between linear and bent conformations (figure 6.2.2). The XAS spectra were best simulated using the bent conformation and thus this geometry was used in our analysis.

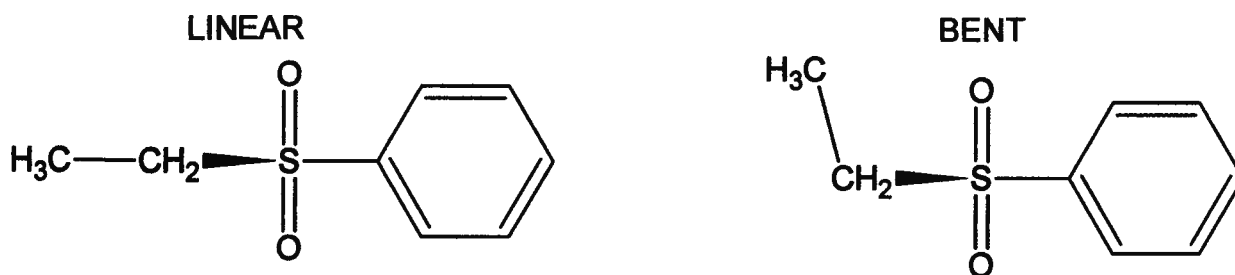


Figure 6.2.2 Geometries of ethyl phenyl sulfone conformations (**3a**).

The TD-DFT simulated spectra (figures 6.2.3 - 6.2.5) for the alkyl compounds (**1-3b**) are in good agreement with experimental data. The spectra of the alkyl compounds are dominated by features due to the σ^* orbitals of the S-C and S=O bonds in the RSO₂ molecular fragment. A low energy feature corresponding to the $\text{SCl}_{\sigma^*} \leftarrow \text{S}_{1s}$ transition is clearly visible in **1b**. For the aryl compounds (**1-3a**) only the calculated spectrum for **2a** is in good agreement with experimental data. Spectra from TD-DFT for **1a** predicts the feature due to $\text{SCl}_{\sigma^*} \leftarrow \text{S}_{1s}$ transition at 2477.4 to have a shoulder, while there is no accounting for the actual shoulder at 2479.6eV in the experimental data. For **3a**, TD-DFT completely fails to predict the feature at 2478.6eV.

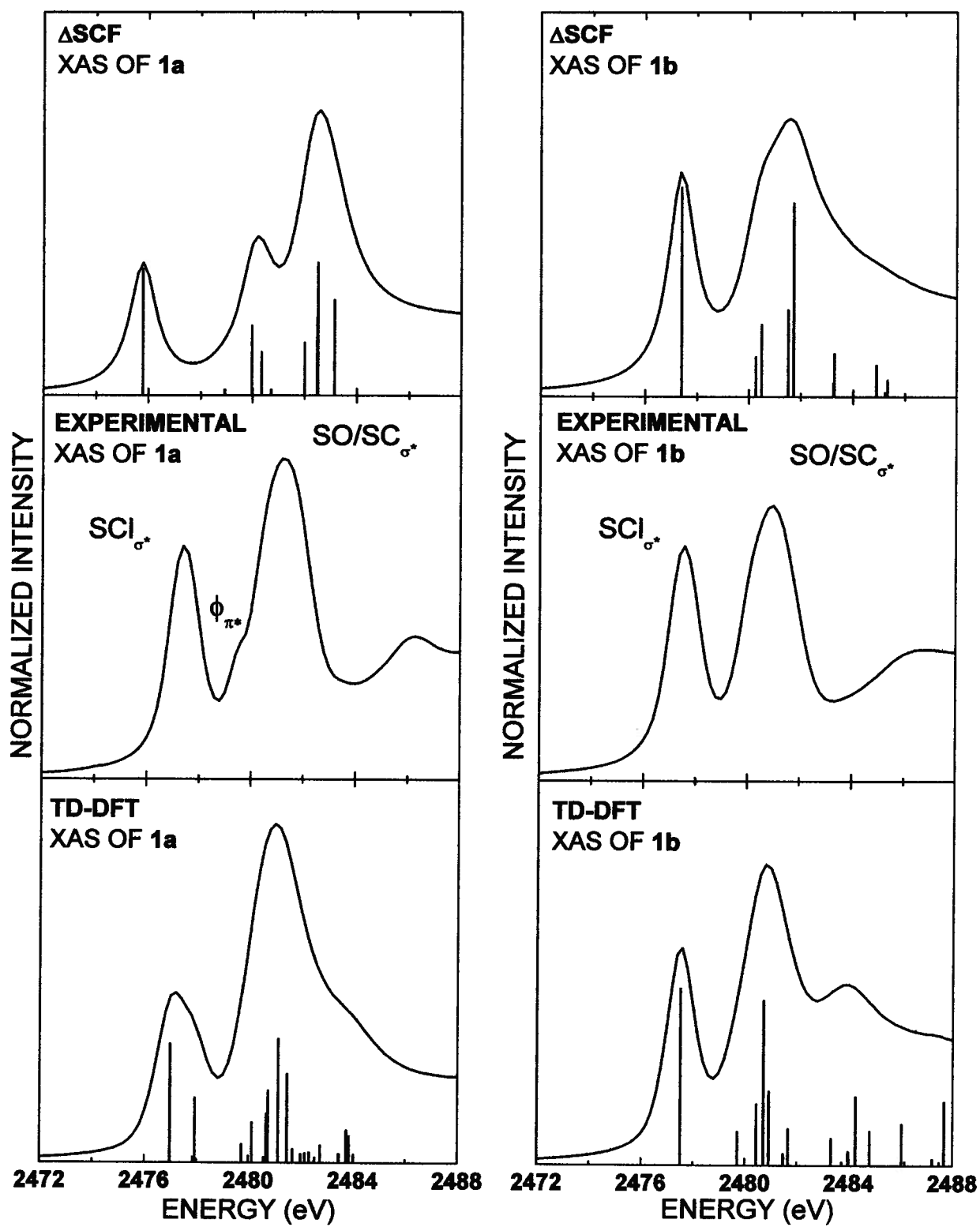


Figure 6.2.3 Comparison of simulated spectra using TD-DFT and Δ SCF, and experimental spectra for compounds **1a,b** the sulfonyl chlorides.

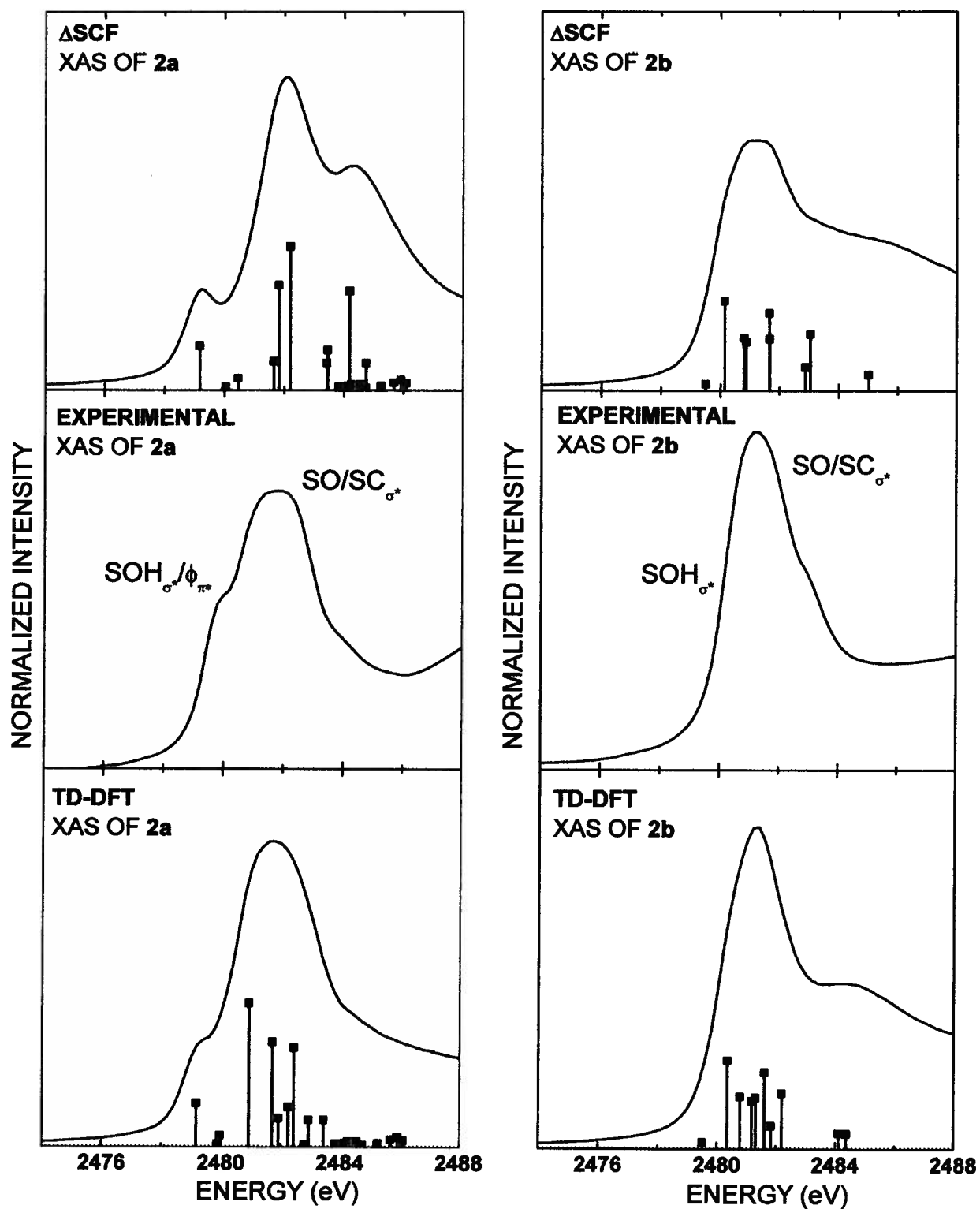


Figure 6.2.4 Comparison of simulated spectra using TD-DFT and Δ SCF, and experimental spectra for compounds **2a,b** the sulfonates.

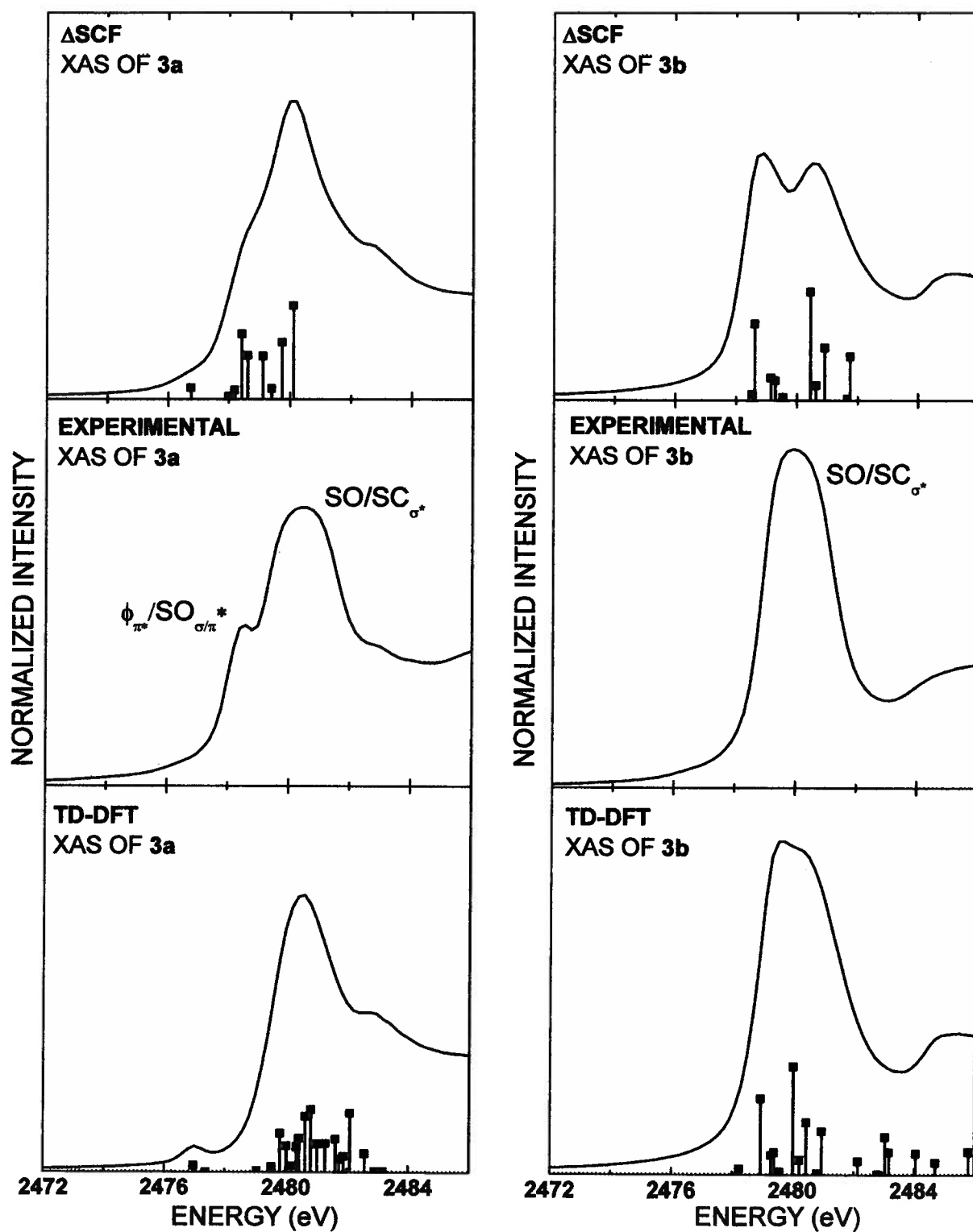


Figure 6.2.5 Comparison of simulated spectra using TD-DFT and Δ SCF, and experimental spectra for compounds 3a,b the sulfones.

However, TD-DFT generates a spectrum using the ground state calculation as its only reference, and thus does not account for possible electronic relaxation in the excited state. To gauge the importance of this effect, the transition energies were recalculated using the Slater transition state Δ SCF approach by populating the acceptor orbital with half an electron and removing the same half electron from the S_{1s} core orbital^{138-141, 171}. Δ SCF can overestimate the relaxation shifts; however, it can be very effective in determining which transitions are most susceptible to relaxation effects. Generally, the alkyl sulfonyl compounds were not affected by relaxation effects as much as the aryl sulfonyls. But even for the alkyl compounds the Δ SCF spectra show broadening of the main spectral features and even a splitting into two peaks as is the case of **3b**. For the aryls the relaxation effects seem least important in the case of **2a** where there is not much change in the Δ SCF simulation from that of the TD-DFT. Relaxation effects become more pronounced in **3a**. Here, Δ SCF accounts for the peak at 2478.6eV by shifting the energies for TD-DFT calculated transitions 5 and 6 to lower energy by ~ 1.1 eV. In **1a** there is a dramatic splitting between transition 1 and transitions 2 and 3 (table 6.2.1), pushing the latter transitions to higher energy. This results in a single peak for the transition at 2477.4eV and suggests that transitions 2 and 3 are responsible for the shoulder at 2479.6eV in the XAS spectra, which TD-DFT calculations failed to account for. It is apparent that orbitals with π^* antibonding character, especially those of the aryl rings are most affected by electronic relaxation.

Together, the TD-DFT and Δ SCF results allow us to assign the features of the sulfur K-edge XAS spectra for each species as illustrated in figures 6.2.3 to 6.2.5. The sulfonyl chlorides exhibit low energy features corresponding to the energy of the $SCl_{\sigma^*} \leftarrow S_{1s}$ transition and higher energy features due to the $SO_{\sigma^*} \leftarrow S_{1s}$ and $SC_{\sigma^*} \leftarrow S_{1s}$ transitions. The shoulder at 2479.6eV, which is present only in the aryl (**1a**), corresponds to the $\Phi^4_{\pi^*} \leftarrow S_{1s}$ transition. $\Phi^4_{\pi^*}$ and $\Phi^5_{\pi^*}$ are the two lowest energy π^* orbitals of the aryl ring (figure 6.2.6). $\Phi^4_{\pi^*}$ has the largest electron density on the carbon bound to the sulfonyl moiety allowing it to mix with the SCl_{σ^*} final state. The mixing gives $\Phi^4_{\pi^*}$ sulfur p character allowing this transition to be visible in the sulfur K-edge XAS spectrum (figure 6.3.1). The XAS spectra of the sulfonic acids (**2a,b**) do not show a distinct pre-edge feature relating to the SG_{σ^*} , because the SOH_{σ^*} orbital is higher in energy than SCl_{σ^*} and overlaps with the main feature of **2a,b** at 2481.7eV. The lower energy shoulder in **2a** is attributed to the $SOH_{\sigma^*} \leftarrow S_{1s}$, which is lowered in energy going

from the alkyl to the aryl by mixing with the $\Phi^4_{\pi^*}$ orbital of the aryl group. Similarly the main features of **3a** and **3b** correspond to a combination of $\text{SO}_{\sigma^*} \leftarrow \text{S}_{1s}$ and $\text{SC}_{\sigma^*} \leftarrow \text{S}_{1s}$ transitions. These transitions are lower in energy than in either the case of the sulfonyl chlorides (**1a,b**) or the sulfonic acids (**2a,b**). Like in the previous examples, the presence of the aryl group is accompanied by additional features in the spectra. **3a** has a lower energy feature not present in **3b** attributed to the $\Phi^4_{\pi^*}$ final state mixing with SO_{σ^*} orbital. This interaction is particularly favorable in **3a** because the two energy states are closer in energy than in any of the other aryl compounds.

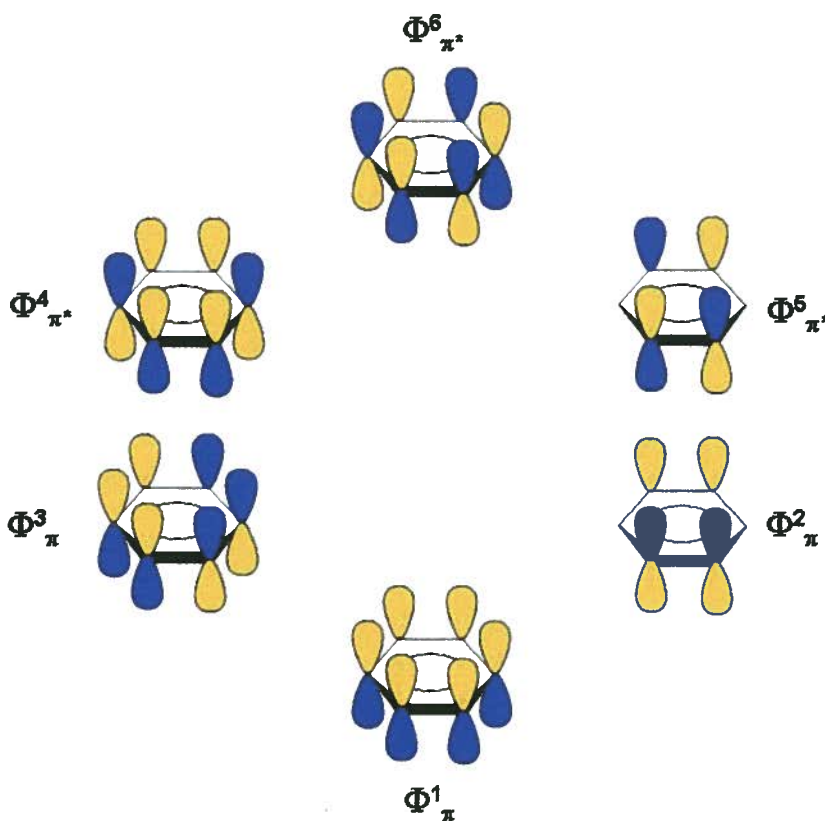


Figure 6.2.6 Molecular orbitals of benzene.

Table 6.2.1. Sulfur K-edge DFT calculated transitions for **1a** with major contributors listed first. Δ SCF calculated energy shifts are referenced to the lowest TD-DFT calculated energy transition.

Transition	Assignment (Primary + Others)	TD-DFT Energies (eV)	Δ SCF (eV)	f
1	SCl_{σ^*} , $\Phi_{\pi^*}^4$, SO_{π^*}	2476.99	0.0	2.3×10^{-3}
2	$\Phi_{\pi^*}^5$	2477.85	+2.3	1.1×10^{-4}
3	$\Phi_{\pi^*}^4$, SO_{σ^*} , SCl_{σ^*}	2477.94	+3.2	1.3×10^{-3}
4	$\text{C}_{\phi}\text{S}_{\sigma^*}$, SO_{σ^*}	2479.74	+1.8	3.6×10^{-4}
5	SO_{σ^*}	2480.13	+1.4	7.9×10^{-4}
6	SO_{π^*} , SO_{σ^*} , Φ_{σ^*}	2480.59	+1.3	1.0×10^{-4}
7	Φ_{σ^*}	2480.69	+2.5	9.6×10^{-4}
8	Φ_{σ^*} ,	2480.76	+2.9	1.4×10^{-3}
9	SO_{σ^*} , SO_{π^*} , Φ_{σ^*}	2481.14	+2.6	2.4×10^{-3}

Table 6.2.2. Sulfur K-edge DFT calculated transitions for **1b** with major contributors listed first. Δ SCF calculated energy shifts are referenced to the lowest TD-DFT calculated energy transition.

Transition	Assignment (Primary , Others)	TD-DFT Energies (eV)	Δ SCF (eV)	f
1	SCl_{σ^*} , SO_{π^*}	2477.50	0.00	3.8×10^{-3}
2	SC_{σ^*} , SO_{σ^*}	2479.72	+0.66	7.2×10^{-4}
3	SC_{σ^*} , SO_{σ^*}	2480.44	+0.18	1.3×10^{-3}
4	SC_{σ^*} , SO_{π^*}	2480.72	+1.12	3.5×10^{-4}
5	SO_{σ^*} CH_{σ^*}	2480.92	+0.70	1.6×10^{-3}
6	CH_{σ^*} , SO_{σ^*}	2481.48	+1.84	2.4×10^{-4}
7	CH_{σ^*} , SO_{σ^*}	2481.67	+1.68	7.9×10^{-4}

Table 6.2.3. Sulfur K-edge DFT calculated transitions for **2a** with major contributors listed first. Δ SCF calculated energy shifts are referenced to the lowest TD-DFT calculated energy transition.

Transition	Assignment (Primary , Others)	TD-DFT Energies (eV)	Δ SCF (eV)	f
1	$\Phi_{\pi^*}^4$, SO_{π^*} , SOH_{σ^*}	2479.16	0.00	1.3×10^{-3}
2	$\Phi_{\pi^*}^5$	2479.87	+0.16	1.0×10^{-4}
3	$\Phi_{\pi^*}^4$, SOH_{σ^*} , SO_{σ^*}	2479.97	+0.49	3.6×10^{-4}
4	SO_{π/σ^*}	2480.93	+1.27	4.3×10^{-3}
5	SO_{π/σ^*} , $\Phi_{\pi^*}^4$	2481.71	+0.11	3.2×10^{-3}
6	SC_{σ^*} , SO_{π^*}	2481.92	-0.28	8.7×10^{-4}
7	SC_{σ^*} , SO_{π^*} , OH_{σ^*}	2482.25	+1.21	1.2×10^{-3}
8	SC_{σ^*} , SO_{π^*} , OH_{σ^*}	2482.43	+1.76	3.0×10^{-3}
9	Φ_{σ^*}	2482.78	+1.86	7.4×10^{-5}

Table 6.2.4. Sulfur K-edge DFT calculated transitions for **2b** with major contributors listed first. Δ SCF calculated energy shifts are referenced to the lowest TD-DFT calculated energy transition.

Transition	Assignment (Primary , Others)	TD-DFT Energies (eV)	Δ SCF (eV)	f
1	SOH_{σ^*} , SC_{σ^*} , SO_{σ^*}	2479.50	0.00	2.0×10^{-4}
2	SO_{π^*} , SC_{σ^*}	2480.35	-0.21	2.7×10^{-3}
3	SC_{σ^*} , SOH_{σ^*}	2480.78	+0.02	1.6×10^{-3}
4	SC_{σ^*} , SO_{π^*}	2481.18	-0.30	1.5×10^{-3}
5	SO_{π/σ^*} , SO_{σ^*}	2481.31	+0.37	1.6×10^{-3}
6	CH_{σ^*} SO_{σ^*} ,	2481.61	+0.05	2.3×10^{-3}
7	CH_{σ^*} , SO_{σ^*}	2481.83	+1.04	7.1×10^{-4}

Table 6.2.5. Sulfur K-edge DFT calculated transitions for **3a** with major contributors listed first. Δ SCF calculated energy shifts are referenced to the lowest TD-DFT calculated energy transition.

Transition	Assignment (Primary , Others)	TD-DFT Energies (eV)	Δ SCF (eV)	f
1	Φ_{π}^4	2476.95	0.00	1.8×10^{-4}
2	Φ_{π}^5	2477.36	+0.85	3.6×10^{-6}
3	SC_{σ}^* , $C_{\phi}S_{\sigma}^*$	2479.04	-0.86	4.1×10^{-5}
4	SC_{σ}^* , $C_{\phi}S_{\sigma}^*$	2479.53	-1.15	1.4×10^{-4}
5	SO_{π}^* , SO_{σ}^* , SC_{σ}^* , $C_{\phi}S_{\sigma}^*$	2479.81	-1.20	1.0×10^{-3}
6	SO_{π}^* , SO_{σ}^* , SC_{σ}^* , $C_{\phi}S_{\sigma}^*$	2480.01	-1.19	6.8×10^{-4}
7	SO_{σ}^* , SO_{π}^*	2480.17	-0.57	1.6×10^{-4}
8	SO_{σ}^* , SO_{π}^*	2480.34	-1.03	6.7×10^{-4}
9	CH_{σ}^*	2480.42	-0.49	8.8×10^{-4}

Table 6.2.6. Sulfur K-edge DFT calculated transitions for **3b** with major contributors listed first. Δ SCF calculated energy shifts are referenced to the lowest TD-DFT calculated energy transition.

Transition	Assignment (Primary , Others)	TD-DFT Energies (eV)	Δ SCF (eV)	f
1	SC_{σ}^*	2478.53	0.00	1.9×10^{-4}
2	SC_{σ}^*	2479.24	-0.62	2.4×10^{-3}
3	CH_{σ}^* , SO_{σ}^*	2479.59	-0.30	6.2×10^{-4}
4	SC_{σ}^* , SO_{π}^*	2479.69	-0.54	7.0×10^{-4}
5	CH_{σ}^* , SO_{σ}^*	2479.87	-0.33	1.0×10^{-4}
6	SO_{π}^* , CH_{σ}^*	2480.31	+0.13	3.4×10^{-3}
7	CH_{σ}^* , SO_{σ}^*	2480.52	+0.12	4.7×10^{-4}
8	SO_{σ}^* , CH_{σ}^*	2480.75	+0.16	1.7×10^{-3}

Photo-cleavage Reactions

To examine the effect of the aryl ring on the generation of the sulfonyl radical and photo-cleavage of the S-Cl bond, p-toluene sulfonyl chloride (**1a**) and methane sulfonyl chloride (**1b**) were irradiated with a 75W Xe arc lamp and XAS spectra were collected as described in the experimental section (figure 6.2.8). Scans were acquired consecutively with continuous irradiation and changes in the intensity of the features attributed to the S-Cl bond, present at 2477.4eV in **1a** and 2477.6eV in **1b**, were recorded. Each scan lasted 5.5 minutes, and over the same time span of irradiation the intensities of both peaks decrease indicating cleavage of the S-Cl bond. The photo-cleavage rate of **1a** containing the aryl moiety was much higher (figure 6.2.7) than in the alkyl containing compound **1b**. This is indicated by the larger decrease in intensity with irradiation attributable to the S-Cl bond feature of **1a**.

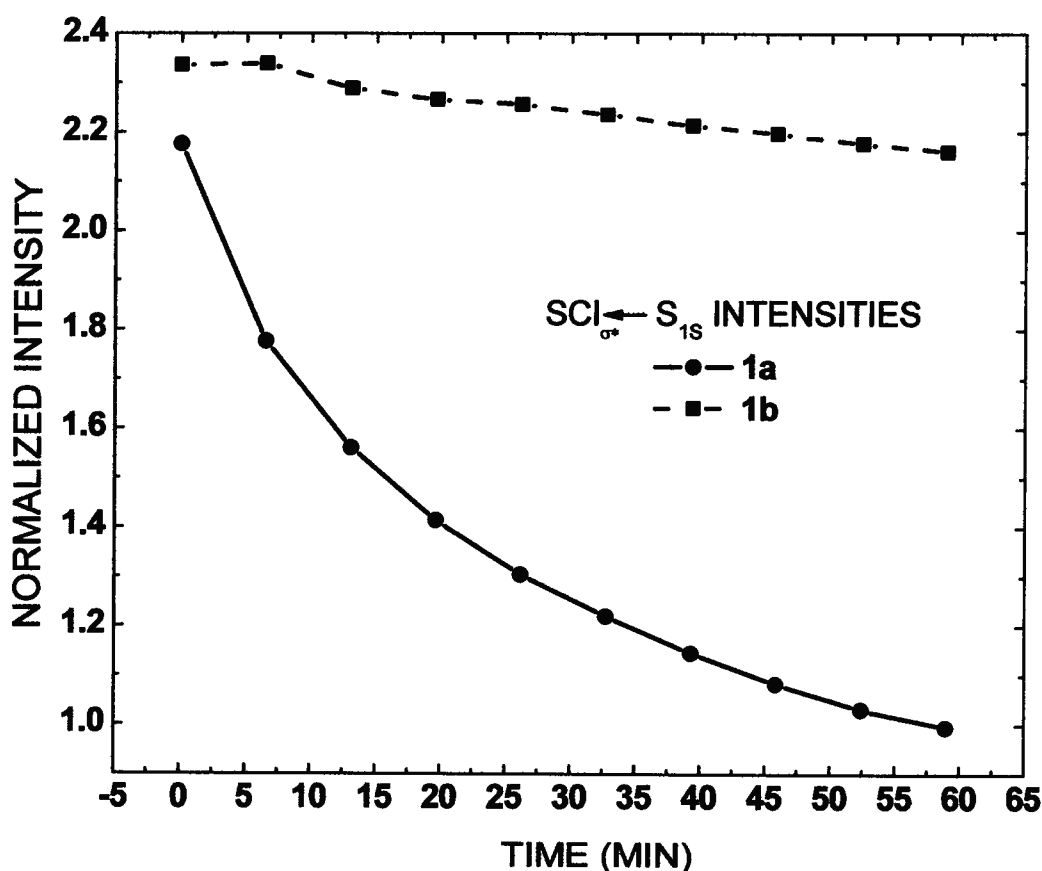


Figure 6.2.7 Time evolution of the sulfur K-edge features due to the S-Cl bond in **1a** and **1b** with in-situ irradiation.

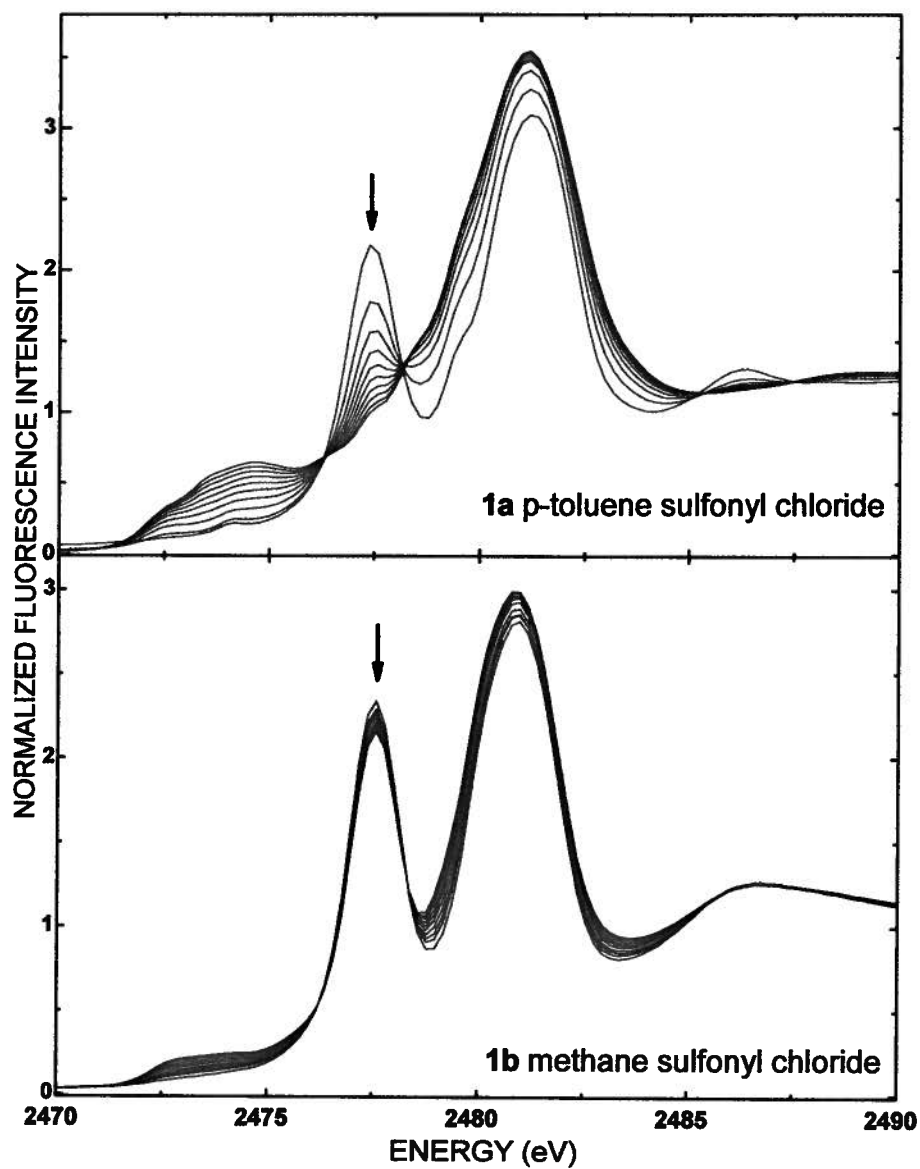


Figure 6.2.8 XAS spectra with *in situ* irradiation of **1a** (top) and **1b** (bottom) with a 75W Xe arc lamp under anaerobic conditions. Scans were taken every ~5.5min with continuous irradiation.

6.3 DISCUSSION

Assigning the sulfur K-edge XAS spectral features of these compounds is the first step in determining the effect of their electronic structure on their respective reactivities. Of particular interest are p-toluene sulfonyl chloride (**1a**) and its role as an initiator in living radical polymerization reactions. The reactivities of the complexes studied should be affected by electronic coupling such as that due to an aromatic group bound directly to the sulfonyl moiety. These interactions have been confirmed by the presence of features in the sulfur K-edge XAS spectra of the aryl compounds which, are not present in their alkyl counterparts, and are attributable to the mixing of $\Phi^4_{\pi^*}$ (aryl π^* orbitals) with orbitals containing sulfur 3p character.

The XAS data coupled with the molecular orbital calculations give insights into the nature of bonding in these systems. In the alkyl compounds (**1-3b**), there is a distinct ordering of the empty valence orbitals with the lowest energy attributed to the SG_{σ^*} followed by SR_{σ^*} , SO_{π^*} , and SO_{σ^*} . The splittings between these states is generally small resulting in a single intense broad feature for these species. The exception is the methane sulfonyl chloride (**1b**) with a very low SG_{σ^*} feature $\sim 3\text{eV}$ below the main peak attributed to the $SCl_{\sigma^*} \leftarrow S_{1s}$ transition. In contrast, the ordering in the aryl compounds is switched such that the transitions due to $SR_{\sigma^*} \leftarrow S_{1s}$ are higher in energy than those of $SO_{\sigma^*} \leftarrow S_{1s}$, resulting in an energy arrangement resembling $E(SG_{\sigma^*}) < E(SO_{\pi^*}) < E(SO_{\sigma^*}) < E(SR_{\sigma^*})$. The reordering of SR_{σ^*} and SO_{σ^*} final states in the aryl compounds is attributable to the stronger S-C bond due to the sp^2 character of the aryl carbons¹⁷². This pushes the SC_{σ^*} orbital to higher energy, which is consistent with the main sulfur K-edge feature for the aryl compounds being $\sim 0.4\text{eV}$ higher in energy than that of the alkyl species.

Furthermore, the aryl group has two low-lying π^* orbitals ($\Phi^4_{\pi^*}$ and $\Phi^5_{\pi^*}$), that can mix and redistribute intensity in the Sulfur K-edge spectra. Since $\Phi^5_{\pi^*}$ has no electron density on the carbon bound to the sulfur, $\Phi^5_{\pi^*}$ is effectively non-bonding with respect to the sulfonyl moiety (figure 6.3.1). As already mentioned $\Phi^4_{\pi^*}$ has good overlap and a strong interaction with the sulfur moiety. This interaction, however, is dependent on the nature of the G group and its bonding interactions. The energy of the $SG_{\sigma^*} \leftarrow S_{1s}$ increases from $Cl \rightarrow OH \rightarrow CH_3$, in agreement with expected bond strengths¹⁷²⁻¹⁷⁴. In

the case of **1a**, mixing with $\Phi^4_{\pi^*}$ results in a further lowering of the SCl_{σ^*} . The higher energy SOH_{σ^*} orbital in **2a** can interact more fully with the aryl group resulting in a highly mixed lowest lying final state in the XAS data. In **3a** however, it is the mixing of the aryl with the SO_{π^*} which takes precedence. The absence of a strong SG_{σ^*} interaction with $\Phi^4_{\pi^*}$ could be attributed to both energetic and overlap considerations. As mentioned earlier, the SO_{π^*} is closer in energy to the aryl $\Phi^4_{\pi^*}$ and the SO_{π^*} orbitals might more readily overlap with the aryl π^* than the sp^3 hybridized orbitals of the ethyl G group in **3a**.

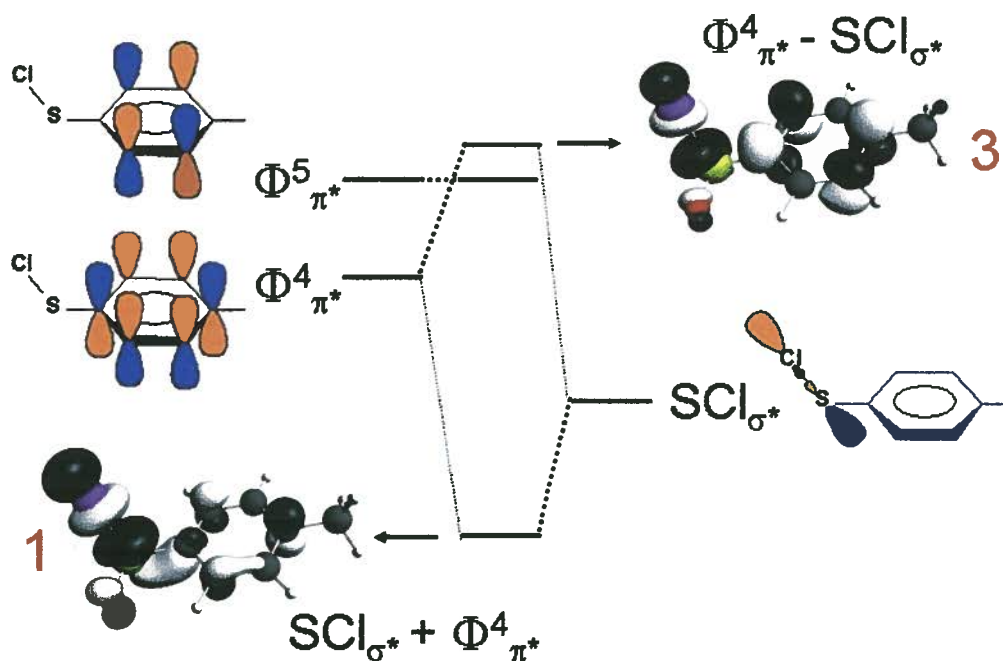


Figure 6.3.1 Mixing of the $\Phi^4_{\pi^*}$, $\Phi^5_{\pi^*}$ and SCl_{σ^*} orbitals resulting in transitions 1 and 3 in the sulfur K-edge spectrum of **1a** (top). (Isovalues = $0.060e\cdot\text{\AA}^{-3}$).

To test whether the effect of the aryl group could in fact be an inductive effect rather than a conjugative one, the aryl ring was rotated with respect to the SG bond to simulate “turning off” aryl hyperconjugation yet maintaining an inductive effect. The result of the rotation about the $\text{S-C}_{(\text{sp}^2)}$ bond on the predicted sulfur K-edge spectrum of **1a** as calculated by TD-DFT is shown in figure 6.3.2. The starting point for the calculation has the aryl ring at 90° to the S-Cl bond and is consistent with the geometry observed in the crystal structure of **1a** where the aryl ring and the S-Cl bond are almost perpendicular (84.3°)¹⁷⁵. As the aryl ring is rotated from a perpendicular plane to the

SG bond, a situation allowing for maximum conjugation, to a plane parallel to the SG bond, resulting in no conjugation to the SG bond, the splitting between the $\text{SCl}_{\sigma^*} \leftarrow \text{S}_{1s}$ and $\Phi^4_{\pi^*} \leftarrow \text{S}_{1s}$ decreases by $\sim 1\text{eV}$. At the same time the intensity of $\text{SCl}_{\sigma^*} \leftarrow \text{S}_{1s}$ increases suggesting increased sulfur p character, while the intensity of $\Phi^4_{\pi^*} \leftarrow \text{S}_{1s}$ decreases indicating a decrease in the sulfur p character. This leads to the conclusion that as hyperconjugation is “turned off” the mixing between $\Phi^4_{\pi^*}$ and S_{1s} is also turned off. The calculated energy stabilization of the hyperconjugative interaction on SCl_{σ^*} is $\sim 0.5\text{eV}$ which is equal to the experimental value for the difference in $\text{SCl}_{\sigma^*} \leftarrow \text{S}_{1s}$ transition energies going from **1b** to **1a**.

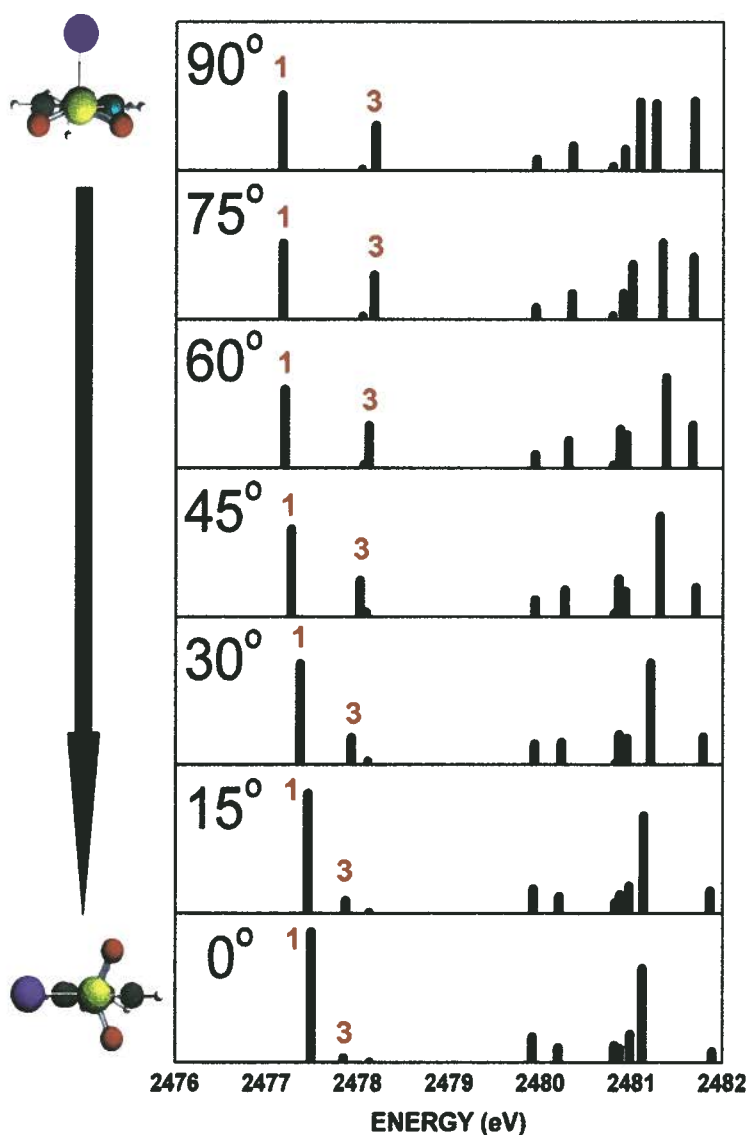


Figure 6.3.2 Effect of turning off $\Phi^4_{\pi^*}/\text{SCl}_{\sigma^*}$ mixing on the intensities and energies of transitions 1 and 3, by rotating the aryl ring.

It is important to note that the above mentioned hyperconjugative interaction occurs between two empty antibonding orbitals; hence it is not a typical hyperconjugative effect. This excited state hyperconjugation¹⁷⁶⁻¹⁷⁸ enhances cleavage of the S-Cl bond in **1a** over **1b** in accordance with the postulate that the aryl group should have a large effect on the S-Cl bond cleavage. Direct photolysis likely results from excitation into the SCl_{σ^*} acceptor orbital with subsequent bond cleavage to form radical products. This study provides a direct assessment of the nature of the SCl_{σ^*} orbital and the effect of the aryl group on the photolytic process. This is very beneficial for living radical polymerization since initiation has to be faster than propagation; therefore facile radical generation is key. The aryl group in **1a** allows for partial delocalization of the excited state electron through mixing with the $\Phi^4_{\pi^*}$ orbital. Mixing of the $\Phi^4_{\pi^*}$ with SCl_{σ^*} orbital results in a decrease in the excitation energy as previously described, but also in a likely increase in the excited state lifetime through charge separation. An increased lifetime of the SCl_{σ^*} excited state allows for a higher transmission coefficient for the overall reaction and a faster rate of photo-cleavage. It can also be argued that the rate of photo-cleavage is faster in toluene sulfonyl chloride because the aryl group itself can enhance the absorption of photons, however this is unlikely since the source of irradiation passes through a plastic window which should remove photons with wavelengths below ~350nm. Because toluene has an absorption maximum at ~260nm¹⁷⁹, no enhancement of photon absorption should occur due to the presence of the aryl group under the described experimental conditions.

6.4 CONCLUSION

In the work on sulfonyl complexes of the type RSO_2G interactions present in the aryl compounds but not seen in their alkyl counterparts were identified. The mixing of the $\Phi^4_{\pi^*}$ aryl orbital into the sulfonyl moiety gives rise to new features in the sulfur K-edge spectra. These features were characterized. Of particular interest is the excited state hyperconjugation interaction between $\Phi^4_{\pi^*}$ and SCl_{σ^*} , resulting in a faster photo-cleavage rate for the S-Cl bond. Excited state hyperconjugation facilitates photo-cleavage by lowering the SCl_{σ^*} energy and allowing delocalization of the excited state, increasing its lifetime and enhancing the photo-cleavage reaction. It is then reasonable to assume that the magnitude of excited state hyperconjugation can be modulated by

electron withdrawing or donating groups on the aromatic ring. Future experiments include plans to acquire XAS spectra for a series of para substituted aryl sulfonyl chlorides with a variety of electron withdrawing and electron donating substituents. Characterization and quantization of the features arising due to the aryl $\Phi^4_{\pi^*}$ mixing with SCl_{σ^*} should be a good measure of the total excited state hyperconjugative interaction present. A preliminary quantization of this effect in p-toluene sulfonyl chloride **1a** was carried out. The increase in intensity ($I_{\Phi^4_{\pi^*} \leftarrow S_{1s}}$) of the $\Phi^4_{\pi^*} \leftarrow S_{1s}$ transition coupled with the decrease in $\text{SCl}_{\sigma^*} \leftarrow S_{1s}$ transition intensity ($I_{\text{SCl}_{\sigma^*} \leftarrow S_{1s}}$) is a direct measure of $\Phi^4_{\pi^*} \text{--} \text{SCl}_{\sigma^*}$ mixing and hence excited state hyperconjugation. Assuming that no other contributions are present in the features due to the SCl_{σ^*} and $\Phi^4_{\pi^*}$ orbitals, the percent of excited state hyperconjugation can be calculated by fitting the sulfur K-edge spectra (figure 6.4.1) and applying equation 6.4.1 to the measured intensities. For **1a** 10-15% mixing of the $\Phi^4_{\pi^*}$ into the SCl_{σ^*} is estimated.

Equation 6.4.1

$$\% \text{ mixing} = \frac{I_{\Phi^4_{\pi^*} \leftarrow S_{1s}}}{\left(I_{\Phi^4_{\pi^*} \leftarrow S_{1s}} + I_{\text{SCl}_{\sigma^*} \leftarrow S_{1s}} \right)} \times 100\%$$

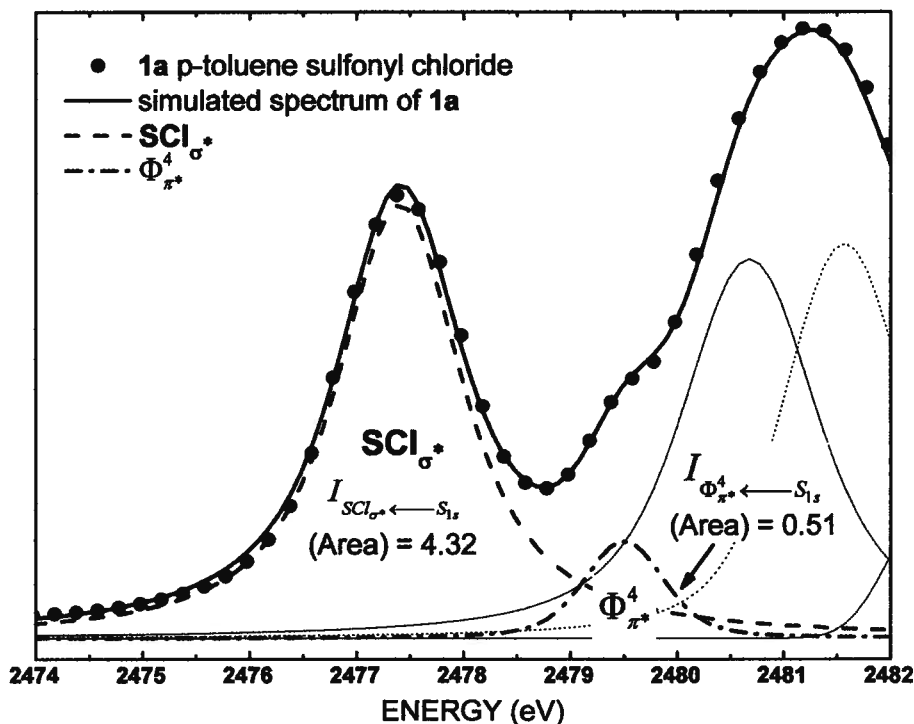


Figure 6.4.1 Fitted XAS spectra of p-toluene sulfonyl chloride (**1a**) with intensities calculated for the $\text{SCl}_{\sigma^*} \leftarrow S_{1s}$ transition and the $\Phi^4_{\pi^*} \leftarrow S_{1s}$ transition.

The question still remains as to why excited state hyperconjugation does not seem to affect the living radical polymerization reactions in which p-toluene sulfonyl chloride (**1a**) acts as an initiator. By definition the initiation step in such reactions is the faster than the propagation step, so the formation of the aryl sulfonyl radical intermediate will not be the major factor to impact reactivity. Furthermore using EPR techniques, previous research has shown that the sulfur p orbital containing the unpaired electron in the aryl sulfonyl radical is in the plane of the phenyl ring¹⁸⁰. This would preclude any interaction of the paramagnetic S_{3p} orbital with the aryl Φ_{π}^4 orbitals. Since it is the half empty S_{3p} orbital which is involved in the polymerization reaction, there would be no major effect on the propagation step due to excited-state hyperconjugation. Also, as the polymer chain grows one would expect the effect of the aryl sulfonyl moiety to diminish. Even if the orientation was optimal for mixing of the S_{3p} and Φ_{π}^4 states in the aryl sulfonyl radicals, preliminary TD-DFT calculation predict this interaction to be minimal.

7 Concluding Remarks and Outlook

In this thesis, the application of Sulfur K-edge XAS to investigate the photo-reactivity of a series of model sulfur containing compounds was discussed. It was shown that XAS can be applied to a wide variety of systems with applications both in biological and inorganic chemistry. XAS proved to be a useful tool in the detection of thiyl radical intermediates in UV irradiated GSH, which are difficult to characterize using other spectroscopic techniques such as EPR. Further research investigating thiyl radical generation and characterization via XAS may help in the elucidation of the mechanism of action of enzyme systems which form thiyl radical intermediates, as is proposed in the case of ribonucleotide reductase¹²³.

Additional sulfur based intermediates were also characterized in the form of the stable perthiyl radical, which is a product of photo-irradiation in all biologically relevant low molecular weight sulfur species investigated. Initially it was somewhat unclear what the mechanism of perthiyl radical formation in GSNO is; however, the XAS spectra indicated generation of a disulfide bond upon photo-irradiation. NMR of irradiated GSNO confirmed disulfide bond formation, and EPR showed that only after disulfide bond generation is the perthiyl radical formed during photo-irradiation.

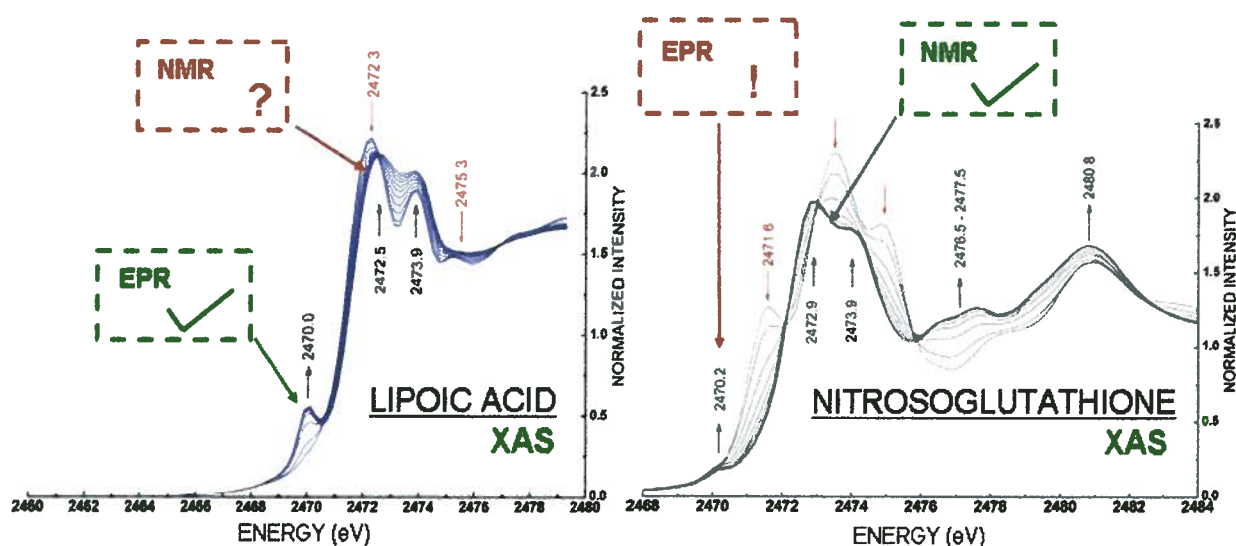


Figure 7.1.1 XAS data from irradiated LA and GSNO complements well the information from both NMR and EPR experiments, filling in the gaps when needed.

Furthermore it is important to note that in both the case of LA and GSNO, XAS detected the intermediates and products being formed, while detection with EPR and NMR proved difficult (figure 7.1.1). In the case of LA, the intermediate was readily detected by EPR while the final major product, which is believed to also be a disulfide, could not be characterized by NMR due to its insolubility. For GSNO the story is somewhat the opposite. While the major product was easily characterized by NMR the formation of the perthiyl radical intermediate seen in the XAS spectra required extensive EPR characterization.

The sensitivity of this technique to the bonding configuration is particularly evidenced in the case of LA, which has features due to $SS_{\sigma^*} \leftarrow S_{1s}$ and $SC_{\sigma^*} \leftarrow S_{1s}$ transitions at lower energy than “linear” disulfides suggesting weaker bonding in the sterically strained pentacyclo-disulfide. GSNO, on the other hand, exhibits sulfur core excitations to the SN_{π^*} orbital consistent with theoretical calculations, indicating the presence of an S- N_{π} resonance form in nitrosylated thiols¹⁵⁷. The applicability of XAS to characterize electronic configurations could be used to further investigate the bonding interactions in S-nitrosothiols. Understanding the bonding interaction in these compounds could help in the synthesis of S-nitrosothiols in which NO^{\bullet} release can be modulated with the potential to target specific locations within the body, and stimulate NO^{\bullet} controlled signaling pathways with beneficial consequences.

The power of XAS to elucidate electronic configuration was also exploited in the case of p-toluene sulfonyl chloride. Here, it was found that p-toluene sulfonyl chloride is more susceptible to photo-reactivity than its alkyl counterpart methane sulfonyl chloride. This was attributed to an excited hyperconjugation bonding interaction, directly detectable via XAS, found between the aromatic antibonding orbitals and the SCl_{σ^*} orbital in p-toluene sulfonyl chloride. Excited state hyperconjugation has also been observed in a series of ruthenium arene thiolates ($Ru(p\text{-cym})(en)SO_2 - Ph$) whose role as therapeutic agents to combat cancer is dependent on Ru-S bond dissociation¹⁸¹. Hyperconjugation could play an essential role in these species and may influence bioactivity of the arylthiolato version of these drugs. Modulating this effect could lead to better anticancer therapeutic agents. Future work includes measuring the excited state hyperconjugation effects in a series of para substituted phenyl sulfonyl chlorides to

determine the impact of electron withdrawing and donating groups on S-Cl bond strengths, the results of which could be applied to the ruthenium arylthiolato complexes.

Coupled with molecular orbital calculations and other spectroscopic techniques XAS is a powerful tool that can offer a wealth of information on the bonding, reactivity and mechanism of reaction for a variety of systems.

References

1. George S D, Petrenko T, and Neese F, *Inorg Chim Acta*, 2008, 361(4), p965.
2. Pickering T J, Prince R C, Divers T, et al., *FEBS Lett*, 1998, 441(1), p11.
3. Rompel A, Cinco R M, Latimer M J, et al., *Proc Natl Acad Sci USA*, 1998, 95(11), p6122.
4. Huffman G P, Shah N, Huggins F E, et al., *Fuel*, 1995, 74(4), p549.
5. Solomon D, Lehmann J, and Martinez C E, *Soil Sci Soc Am J*, 2003, 67(6), p1721.
6. Sandstrom M, Jalilehvand F, Persson I, et al., *Nature*, 2002, 415(6874), p893.
7. Gales L, Cardoso I, Fayard B, et al., *J Biol Chem*, 2003, 278(13), p11654.
8. Prange A, Dahl C, Truper H G, et al., *Eur Phys J D*, 2002, 20(3), p589.
9. Bellacchio E, McFarlane K L, Rompel A, et al., *J Synch Rad*, 2001, 8, p1056.
10. Prange A, Chauvistre R, Modrow H, et al., *Microbiology-Sgm*, 2002, 148, p267.
11. Shadle S E, Hedman B, Hodgson K O, et al., *Inorg Chem*, 1994, 33(19), p4235.
12. Williams K, Hedman B, Hodgson K O, et al., *Inorg Chim Acta*, 1997, 263(1-2), p315.
13. Solomon E I, Hedman B, Hodgson K O, et al., *Coord Chem Rev*, 2005, 249(1-2), p97.
14. Szilagyi R K and Schwab D E, *Biochem Biophys Res Commun*, 2005, 330(1), p60.
15. Sarangi R, Frank P, Hodgson K O, et al., *Inorg Chim Acta*, 2008, 361(4), p956.
16. Moriarty-Craige S E and Jones D P, *Annu Rev Nutr*, 2004, 24, p481.
17. Schafer F Q and Buettner G R, *Free Radical Biol Med*, 2001, 30(11), p1191.
18. Kirlin W G, Cai J, Thompson S A, et al., *Free Radical Biol Med*, 1999, 27(11-12), p1208.
19. Jones D P, Carlson J L, Mody V C, et al., *Free Radical Biol Med*, 2000, 28(4), p625.
20. Hoshi T and Heinemann S H, *J Physiol-London*, 2001, 531(1), p1.
21. Pastore A, Federici G, Bertini E, et al., *Clin Chim Acta*, 2003, 333(1), p19.
22. Myers P R, Minor R L, Guerra R, et al., *Nature*, 1990, 345(6271), p161.
23. Jocelyn P C, *Eur J Biochem*, 1967, 2(3), p327.
24. Lodge J K, Traber M G, and Packer L, *Free Radical Biol Med*, 1998, 25(3), p287.
25. Moini H, Packer L, and Saris N-E L, *Toxicol Appl Pharmacol*, 2002, 182(1), p84.

26. Allen R G, Newton R K, Sohal R S, et al., *J Cell Physiol*, 1985, 125(3), p413.
27. Sandstrom B E and Marklund S L, *Biochem J*, 1990, 271(1), p17.
28. Klug A and Rhodes D, *Cold Spring Harb Symp Quant Biol*, 1987, 52, p473.
29. Sen C K and Packer L, *FASEB J*, 1996, 10(7), p709.
30. Suthanthiran M, Anderson M E, Sharma V K, et al., *Proc Natl Acad Sci USA*, 1990, 87(9), p3343.
31. Avval F Z and Holmgren A, *J Biol Chem*, 2009, 284(13), p8233.
32. Ho Y-F and Guenther T M, *Chinese Pharm J (Taipei)*, 1997, 49(5-6), p267.
33. Hwang C, Sinskey A J, and Lodish H F, *Science*, 1992, 257(5076), p1496.
34. Sevier C S and Kaiser C A, *Nat Rev Mol Cell Biol*, 2002, 3(11), p836.
35. Anfinsen C and Haber E, *J Biol Chem*, 1961, 236(5), p1361.
36. Staal F J T, Ela S W, Roederer M, et al., *Lancet*, 1992, 339(8798), p909.
37. Buhl R, Holroyd K, Mastrangeli A, et al., *Lancet*, 1989, 334(8675), p1294.
38. Eck H P, Gmunder H, Hartmann M, et al., *Biol Chem Hoppe-Seyler*, 1989, 370(2), p101.
39. Staal, *Eur J Clin Invest*, 1998, 28(3), p194.
40. Smith C V, Jones D P, Guenther T M, et al., *Toxicol Appl Pharmacol*, 1996, 140(1), p1.
41. Nakamura H, De Ros S C, Yodoi J J, et al., *Proc Natl Acad Sci USA*, 2001, 98(5), p2688.
42. Lioy J, Ho W Z, Cutilli J R, et al., *J Clin Invest*, 1993, 91(2), p495.
43. Denu J M and Tanner K G, *Biochemistry*, 1998, 37(16), p5633.
44. Hehner S P, Breitkreutz R, Shubinsky G, et al., *J Immunol*, 2000, 165(8), p4319.
45. Read M A, Whitley M Z, Gupta S, et al., *J Biol Chem*, 1997, 272(5), p2753.
46. Moinova H R and Mulcahy R T, *Biochem Biophys Res Commun*, 1999, 261(3), p661.
47. Hansen J M, Watson W H, and Jones D P, *Toxicol Sci*, 2004, 82(1), p308.
48. Dinkova-Kostova A T, Holtzclaw W D, Cole R N, et al., *Proc Natl Acad Sci USA*, 2002, 99(18), p11908.
49. Bloom D, Dhakshinamoorthy S, and Jaiswal A K, *Oncogene*, 2002, 21(14), p2191.
50. Droge W, *Phys Rev*, 2002, 82(1), p47.
51. Finkel T and Holbrook N J, *Nature*, 2000, 408(6809), p239.

52. Wink D A and Mitchell J B, *Free Radical Biol Med*, 1998, 25(4-5), p434.
53. Nordberg J and Arner E S J, *Free Radical Biol Med*, 2001, 31(11), p1287.
54. Thomas E L, Lehrer R I, and Rest R F, *Rev Infect Dis*, 1988, 10, pS450.
55. Ignarro L J and Kadowitz P J, *Annu Rev Pharmacol Toxicol*, 1985, 25, p171.
56. Ignarro L J, *Pharmacol Toxicol*, 1990, 67(1), p1.
57. Radomski M W, Palmer R M J, and Moncada S, *Br J Pharmacol*, 1987, 92(3), p639.
58. Turrens J F, *Biosci Rep*, 1997, 17(1), p3.
59. Inoue M, Sato E F, Nishikawa M, et al., *Curr Med Chem*, 2003, 10(23), p2495.
60. McIntyre M, Bohr D F, and Dominiczak A F, *Hypertension*, 1999, 34(4), p539.
61. Fridovich I, *Science*, 1978, 201(4359), p875.
62. Rhee S G, *Exp Mol Med*, 1999, 31(2), p53.
63. Halliwell B, *FASEB J*, 1987, 1(5), p358.
64. Chance B, Sies H, and Boveris A, *Phys Rev*, 1979, 59(3), p527.
65. Leonard S S, Harris G K, and Shi X L, *Free Radical Biol Med*, 2004, 37(12), p1921.
66. Reddie K G and Carroll K S, *Curr Opin Chem Biol*, 2008, 12(6), p746.
67. Chelikani P, Fita I, and Loewen P C, *Cell Mol Life Sci*, 2004, 61(2), p192.
68. Epp O, Ladenstein R, and Wendel A, *Eur J Biochem*, 1983, 133(1), p51.
69. Chae H Z, Kim H J, Kang S W, et al., *Diabetes Res Clin Pract*, 1999, 45(2-3), p101.
70. Monteiro G, Horta B B, Pimenta D C, et al., *Proc Natl Acad Sci USA*, 2007, 104(12), p4886.
71. Rhee S G, Chae H Z, and Kim K, *Free Radical Biol Med*, 2005, 38(12), p1543.
72. Biteau B, Labarre J, and Toledano M B, *Nature*, 2003, 425(6961), p980.
73. Woo H A, Chae H Z, Hwang S C, et al., *Science*, 2003, 300(5619), p653.
74. Palmer R M J, Rees D D, Ashton D S, et al., *Biochem Biophys Res Commun*, 1988, 153(3), p1251.
75. Wink D A, Nims R W, Darbyshire J F, et al., *Chem Res Toxicol*, 1994, 7(4), p519.
76. Coupe P J and Williams D L H, *J Chem Soc-Perkin Trans 2*, 2001(9), p1595.
77. Stoyanovsky D A, Tyurina Y Y, Tyurin V A, et al., *J Am Chem Soc*, 2005, 127(45), p15815.

78. Konorev E A, Kalyanaraman B, and Hogg N, *Free Radical Biol Med*, 2000, 28(11), p1671.
79. Al-Sa'doni H and Ferro A, *Clin Sci*, 2000, 98(5), p507.
80. Butler A R, Al-Sa'doni H H, Megson I L, et al., *Nitric Oxide*, 1998, 2(3), p193.
81. Davis F J, Gilbert B C, Norman R O C, et al., *J Chem Soc-Perkin Trans 2*, 1983(11), p1763.
82. Prutz W A, Butler J, and Land E J, *Biophys Chem*, 1994, 49(2), p101.
83. Laurie S H, Lund T, and Raynor J B, *J Chem Soc-Dalton Trans*, 1975(14), p1389.
84. Lima A I G, Corticeiro S C, and de Almeida Paula Figueira E M, *Enzyme and Microb Technol*, 2006, 39(4), p763.
85. Da Costa Ferreira A M, Ciriolo M R, Marcocci L, et al., *Biochem J*, 1993, 292(3), p673.
86. Valko M, Rhodes C J, Moncol J, et al., *Chemico-Biol Interact*, 2006, 160(1), p1.
87. Spear N and Aust S D, *Arch Biochem Biophys*, 1994, 312(1), p198.
88. Misra H P, *J Biol Chem*, 1974, 249(7), p2151.
89. Holmgren A, *Annu Rev Biochem*, 1985, 54, p237.
90. Taniguchi Y, Taniguchi Ueda Y, Mori K, et al., *Nucleic Acids Res*, 1996, 24(14), p2746.
91. Spyrou G, Enmark E, Miranda-Vizuete A, et al., *J Biol Chem*, 1997, 272(5), p2936.
92. Miranda-Vizuete A, Ljung J, Damdimopoulos A E, et al., *J Biol Chem*, 2001, 276(34), p31567.
93. Holmgren A, *J Biol Chem*, 1989, 264(24), p13963.
94. Berndt C, Lillig C H, and Holmgren A, *Am J Physiol Heart Circ Physiol*, 2007, 292(3), p1227.
95. Kallis G B and Holmgren A, *J Biol Chem*, 1980, 255(21), p10261.
96. Arner E S J and Holmgren A, *Eur J Biochem*, 2000, 267(20), p6102.
97. Tamura T and Stadtman T C, *Proc Natl Acad Sci USA*, 1996, 93(3), p1006.
98. Gladyshev V N, Jeang K T, and Stadtman T C, *Proc Natl Acad Sci USA*, 1996, 93(12), p6146.
99. Sun Q A, Zappacosta F, Factor V M, et al., *J Biol Chem*, 2001, 276(5), p3106.

100. Zhong L W, Arner E S J, and Holmgren A, *Proc Natl Acad Sci USA*, 2000, 97(11), p5854.
101. Arscott L D, Gromer S, Schirmer R H, et al., *Proc Natl Acad Sci USA*, 1997, 94(8), p3621.
102. Klintrot I-M, Hoog J-O, Jornvall H, et al., *Eur J Biochem*, 1984, 144(3), p417.
103. Gladyshev V N, Liu A M, Novoselov S V, et al., *J Biol Chem*, 2001, 276(32), p30374.
104. Wingert R A, Galloway J L, Barut B, et al., *Nature*, 2005, 436(7053), p1035.
105. Takashima Y, Hirota K, Nakamura H, et al., *Immunol Lett*, 1999, 68(2-3), p397.
106. Daily D, Vlamis-Gardikas A, Offen D, et al., *J Biol Chem*, 2001, 276(2), p1335.
107. Wells W W, Xu D P, Yang Y F, et al., *J Biol Chem*, 1990, 265(26), p15361.
108. Hirota K, Matsui M, Murata M, et al., *Biochem Biophys Res Commun*, 2000, 274(1), p177.
109. Gravina S A and Mieyal J J, *Biochemistry*, 1993, 32(13), p3368.
110. Bushweller J H, Aslund F, Wuthrich K, et al., *Biochemistry*, 1992, 31(38), p9288.
111. Mize C E, Thompson T E, and Langdon R G, *J Biol Chem*, 1962, 237(5), p1596.
112. Staal G E J and Veeger C, *Biochim Biophys Acta-Enzymology*, 1969, 185(1), p49.
113. Massey V and Williams C H J, *J Biol Chem*, 1965, 240, p4470.
114. Schulz G E, Zappe H, Worthington D J, et al., *FEBS Lett*, 1975, 54(1), p86.
115. Zappe H A, Krohne-Ehrich G, and Schulz G E, *J Mol Biol*, 1977, 113(1), p141.
116. Worthington D J and Rosemeyer M A, *Eur J Biochem*, 1976, 67(1), p231.
117. Krohneehrich G, Schirmer R H, and Untuchtgrau R, *Eur J Biochem*, 1977, 80(1), p65.
118. Ellman G L, *Arch Biochem Biophys*, 1959, 82(1), p70.
119. Eaton P, *Free Radical Biol Med*, 2006, 40(11), p1889.
120. Ellis H R and Poole L B, *Biochemistry*, 1997, 36(48), p15013.
121. Jaffrey S R and Snyder S H, *Science*, 2001, 2001(86), ppl1.
122. Jalilehvand F, *Chem Soc Rev*, 2006, 35(12), p1256.
123. Nordlund N and Reichard P, *Annu Rev Biochem*, 2006, 75, p681.
124. Sjoberg B M, *Metal Sites in Proteins and Models*, 1997, 88, p139.
125. Carrington A and McLachlan D M, *Introduction to Magnetic Resonance*. 1969, New York: Harper & Row,.

126. Symons M C R, *J Chem Soc-Perkin Trans 2*, 1974(13), p1618.
127. van Gastel M, Lubitz W, Lassmann G, et al., *J Am Chem Soc*, 2004, 126(7), p2237.
128. Denehy E, White J M, and Williams S J, *Inorg Chem*, 2007, 46(21), p8871.
129. Fehnel E A and Carmack M, *J Am Chem Soc*, 1950, 72(3), p1292.
130. Lytle F W, Greigor R B, Sandstrom D R, et al., *Nucl Instr Meth*, 1984, 226(2-3), p542.
131. Kennepohl P, Wasinger E, and George S D, *J Synch Rad*, 2009, 16, p484.
132. Hedman B, Frank P, Gheller S F, et al., *J Am Chem Soc*, 1988, 110(12), p3798.
133. Sekiyama H, Kosugi N, Kuroda H, et al., *Bull Chem Soc Jpn*, 1986, 59(2), p575.
134. Delgado-Jaime M U, Conrad J C, Fogg D E, et al., *Inorg Chim Acta*, 2006, 359(9), p3042.
135. Webb S M, *Phys Scr*, 2005, T115, p1011.
136. Guerra C F, Snijders J G, te Velde G, et al., *Theor Chem Acc*, 1998, 99(6), p391.
137. Velde G T, Bickelhaupt F M, Baerends E J, et al., *J Comput Chem*, 2001, 22(9), p931.
138. Schwarz K, *Chem Phys*, 1975, 7(1), p100.
139. Sen K D, *J Phys B*, 1978, 11(19), pL577.
140. Gopinathan M S, *J Phys B*, 1979, 12(4), p521.
141. Triguero L, Pettersson L G M, and Agren H, *Phys Rev B*, 1998, 58(12), p8097.
142. Krzystek J, Sienkiewicz A, Pardi L, et al., *J Magn Reson*, 1997, 125(1), p207.
143. Hart T W, *Tetrahedron Lett*, 1985, 26(16), p2013.
144. Giles N M, Giles G I, and Jacob C, *Biochem Biophys Res Commun*, 2003, 300(1), p1.
145. Silva D J, Stubbe J, Samano V, et al., *Biochemistry*, 1998, 37(16), p5528.
146. Lassmann G, Kolberg M, Bleifuss G, et al., *Phys Chem Chem Phys*, 2003, 5(11), p2442.
147. Kolberg M, Bleifuss G, Graslund A, et al., *Arch Biochem Biophys*, 2002, 403(1), p141.
148. Kolberg M, Bleifuss G, Sjöberg B-M, et al., *Arch Biochem Biophys*, 2002, 397(1), p57.
149. Terryn H, Tilquin B, and Houee-Levin C, *Res Chem Intermed*, 2005, 31(7-8), p727.

150. Morine G H and Kuntz R R, *Photochem Photobiol*, 1981, 33(1), p1.
151. Grant D W and Stewart J H, *Photochem Photobiol*, 1984, 40(3), p285.
152. Wood P D, Bulent Mutus, and Robert W. Redmond, *Photochem Photobiol*, 1996, 64(3), p518.
153. Barron L B, Waterman K C, Filipiak P, et al., *J Phys Chem A*, 2004, 108(12), p2247.
154. Bucher G, Lu C Y, and Sander W, *ChemPhysChem*, 2005, 6(12), p2607.
155. Manoj V M, Mohan H, Aravind U K, et al., *Free Radical Biol Med*, 2006, 41(8), p1240.
156. Williams D L H, *Org Biomol Chem*, 2003, 1(3), p441.
157. Timerghazin Q K, Peslherbe G H, and English A M, *Org Lett*, 2007, 9(16), p3049.
158. George G N, Gnida M, Bazylinski D A, et al., *J Bacteriol*, 2008, 190(19), p6376.
159. Cavero M, Hobbs A, Madge D, et al., *Bioorg Med Chem Lett*, 2000, 10(7), p641.
160. Petzold H and Sadler P J, *Chem Comm*, 2008(37), p4413.
161. Percec V, Kim H J, and Barboiu B, *Macromol*, 1997, 30(26), p8526.
162. Percec V, Barboiu B, and Kim H J, *J Am Chem Soc*, 1998, 120(2), p305.
163. Braunecker W A and Matyjaszewski K, *Prog Polym Sci*, 2007, 32, p93.
164. Fischer H, *Chem Rev*, 2001, 101(12), p3581.
165. Kharasch M S and Zavist A F, *J Am Chem Soc*, 1951, 73(3), p964.
166. Orochov A, Asscher M, and Vofsi D, *J Chem Soc B Phys Org*, 1969(3), p255.
167. Correa C M M and Waters W A, *J Chem Soc C-Org*, 1968(15), p1874.
168. Asscher M and Vofsi D, *J Chem Soc*, 1964(DEC), p4962.
169. Asscher J S a M, *J Chem Soc Perkin Trans 1*, 1972, p1543
170. Akabayov B, Doonan C J, Pickering I J, et al., *J Synch Rad*, 2005, 12, p392.
171. Triguero L, Pettersson L G M, and Agren H, *J Phys Chem A*, 1998, 102(52), p10599.
172. Herron J T, *Thermochemistry of sulfoxides and sulfones*, in *The Chemistry of Sulphones and Sulphoxides*, S. Patai, Z. Rappoport, and C.J.M. Stirling, Editors. 1988, John Wiley & Sons Ltd.: New York. p. 95.
173. Chatgililoglu C, Griller D, Kanabus-Kaminska J M, et al., *J Chem Soc Perkin Trans 2*, 1994(2), p357.
174. Korth H G, Neville A G, and Luszyk J, *J Phys Chem*, 1990, 94(25), p8835.
175. Brunvoll J and Hargittai I, *J Mol Struct*, 1976, 30, p361.

176. Nakai H and Kawai M, *J Chem Phys*, 2000, 113(6), p2168.
177. Rao C N R, Goldman G K, and Balasubramanian A, *Can J Chem*, 1960, 38, p2508.
178. Wladislaw B, Viertler H, Olivato P R, et al., *J Chem Soc Perkin Trans 2*, 1980(3), p453.
179. Hai D, Ru-Chun Amy F, Junzhong L, et al., *Photochem Photobiol*, 1998, 68(2), p141.
180. Chatgililoglu C, Gilbert B C, and Norman R, *J Chem Soc Perkin Trans 2*, 1979, p770.
181. Sriskandakumar T, Petzold H, Bruijnincx P, et al., *J Am Chem Soc*, (submitted 2009).

Appendix 1: ADF Input Files

A1.1 ADF input file for ground state and time-dependent DFT calculations on CH₃SH.

```
UNITS
    length Angstrom
    angle Degree
END
```

```
ATOMS
1 C x1 y1 z1
2 H x2 y2 z2
3 H x3 y3 z3
4 H x4 y4 z4
5 S x5 y5 z5
6 H x6 y6 z6
END
```

```
GEOVAR
x1 -0.9323645165
y1 0.7538453976
z1 -0.2554338150
x2 -1.358906052
y2 1.765267821
z2 -0.2847699841
x3 -0.1640953568
y3 0.7242029073
z3 0.5300502049
x4 -1.707025428
y4 0.1481577134E-01
z4 -0.1134618763E-01
x5 -0.7743971035E-01
y5 0.3446657011
z5 -1.785980422
x6 -1.154233121
y6 0.4311598236
z6 -2.607633668
END
```

```
XC
GGA Becke Perdew
END
```

```
SYMMETRY NOSYM tol=0.001
```

```
SAVE TAPE21 TAPE13
```

```
EXCITATION
Davidson
lowest 50
END
```

```
SCF
iterations 50
converge 1.0e-6 1.0e-3
mixing 0.2
lshift 0.0
diis n=10 ok=0.5 cyc=5 cx=5.0 cxx=10.0
END
```

```
INTEGRATION 4 7 7
```

AlFIT 10.0

ModifyExcitations
 UseOccupied
 A 1
 SubEnd
End

Fragments
H t21.H
S t21.S
C t21.C
End

A1.2 ADF input file for ground state and time-dependent DFT calculations on CH₃S[•] radical.

UNITS
 length Angstrom
 angle Degree
END

ATOMS
1 C x1 y1 z1
2 H x2 y2 z2
3 H x3 y3 z3
4 H x4 y4 z4
5 S x5 y5 z5
END

GEOVAR
x1 -0.8955097192
y1 0.7461104821
z1 -0.2655950654
x2 -1.354738363
y2 1.747210887
z2 -0.3146675968
x3 -0.1716129346
y3 0.7262054524
z3 0.5651110213
x4 -1.692308581
y4 0.1402182236E-01
z4 -0.5039963098E-01
x5 -0.1075872236
y5 0.3483459909
z5 -1.799000867
END

XC
GGA Becke Perdew
END

CHARGE 0 1

UNRESTRICTED
SYMMETRY NOSYM tol=0.001

SAVE TAPE21 TAPE13

EXCITATION

Davidson

lowest 50

END

SCF

iterations 50

converge 1.0e-6 1.0e-3

mixing 0.2

lshift 0.0

diis n=10 ok=0.5 cyc=5 cx=5.0 cxx=10.0

END

INTEGRATION 4 7 7

ALFIT 10.0

ModifyExcitations

UseOccupied

A 1

SubEnd

End

Fragments

H t21.H

S t21.S

C t21.C

End

A1.3 ADF input file for ground state and time-dependent DFT calculations on CH₃SS[•] radical.

UNITS

length Angstrom

angle Degree

END

ATOMS

1 C x1 y1 z1

2 H x2 y2 z2

3 H x3 y3 z3

4 H x4 y4 z4

5 S x5 y5 z5

6 S x6 y6 z6

END

GEOVAR

x1 -0.8166129615

y1 0.7670805715

z1 -0.2042560278E-01

x2 -1.256955743

y2 1.771247152

z2 -0.9940988876E-01

x3 -0.7116845060E-01

y3 0.7416107139

z3 0.7891296540

x4 -1.608232053

```

y4 0.2820444077E-01
z4 0.1690125105
x5 0.2966549980E-01
y5 0.3608788083
z5 -1.548454032
x6 -1.314040181
y6 0.4088199419
z6 -2.953060041
END

XC
GGA Becke Perdew
END

CHARGE 0.0 1

UNRESTRICTED
SYMMETRY NOSYM tol=0.001
SAVE TAPE21 TAPE13

EXCITATION
Davidson
lowest 40
END

QTENS

ESR
END
SCF
iterations 50
converge 1.0e-6 1.0e-3
mixing 0.2
lshift 0.0
diis n=10 ok=0.5 cyc=5 cx=5.0 cxx=10.0
END

INTEGRATION 4 7 7
AlFIT 10.0

ModifyExcitations
UseOccupied
A 1
SubEnd
End

Fragments
H t21.H
S t21.S
C t21.C
End

```


A1.4 ADF input file for ground state and time-dependent DFT calculations of CH₃CH₂SNO.

```
# =====  
# The Molecule  
# =====
```

```
"$ADFBIN/adf" <<eor  
ModifyExcitations  
  UseOccupied  
    A 1  
  SubEnd  
End
```

```
UNITS  
  length Angstrom  
  angle Degree  
END
```

```
ATOMS  
1 C      0.093299330556      0.376389670055      -0.070212789684  
2 S      1.801870998890     -0.249839100900     -0.035836671374  
3 N      2.564608078090      1.463353251410     -0.011760165370  
4 O      3.750776088010      1.529149793600     -0.030834631742  
5 C     -0.541415135994      0.331366484092     -1.458391795540  
6 H     -1.580659823740      0.688033224536     -1.411767390600  
7 H      0.010874680875      0.971075028574     -2.158717739280  
8 H     -0.548506825515     -0.689497465788     -1.862015876210  
9 H     -0.475693154085     -0.217296736284      0.656435439622  
10 H      0.157575073270      1.407803333340      0.310912848049  
END
```

```
GUIBONDS  
1 2 1 1.0  
2 3 2 1.0  
3 4 3 1.0  
4 6 5 1.0  
5 7 5 1.0  
6 8 5 1.0  
7 5 1 1.0  
8 9 1 1.0  
9 10 1 1.0  
END
```

```
CHARGE 0.0
```

```
SYMMETRY NOSYM tol=0.001
```

```
BASIS  
type TZ2P  
core None  
END
```

```
XC  
GGA Becke Perdew  
END
```

```
SAVE TAPE21 TAPE13
```

```

EXCITATION
Davidson
ONLYSING
lowest 10
END

SCF
iterations 50
converge 1.0e-6 1.0e-3
mixing 0.2
lshift 0.0
diis n=10 ok=0.5 cyc=5 cx=5.0 cxx=10.0
END

INTEGRATION 6 6 6

AlFIT 10.0

eor

mkdir tapes
mv -f TAPE* tapes 2>/dev/null

# =====
# DENSF
# =====

cp tapes/TAPE21 TAPE21
"$ADFBIN/densf" <<eor
Density fit trans
Potential coul trans
eor

mv TAPE41 tapes/TAPE41
rm -f TAPE*

mv -f tapes/TAPE* .

```

A1.5 ADF input file for ground state and time-dependent DFT calculations of CH₃SSCH₃.

```

# =====
# The Molecule
# =====

"$ADFBIN/adf" <<eor
TITLE Methyl Disulfide SP SK

UNITS
    length Angstrom
    angle Degree
END

ATOMS
1 C x1 y1 z1

```

2 H x2 y2 z2
3 H x3 y3 z3
4 H x4 y4 z4
5 S x5 y5 z5
6 S x6 y6 z6
7 C x7 y7 z7
8 H x8 y8 z8
9 H x9 y9 z9
10 H x10 y10 z10
END

GEOVAR

x1 -0.4008420982
y1 0.3905396080
z1 -0.2322155253
x2 -0.5126493230E-01
y2 0.4627550644
z2 -1.268344630
x3 -0.4137836966E-01
y3 -0.5403383933
z3 0.2217839358
x4 -1.494155479
y4 0.4149537687
z4 -0.2059453443
x5 0.2480197890
y5 1.801338869
z5 0.7591664997
x6 -1.313268316
y6 3.138545139
z6 0.7997379556
x7 -2.222534719
y7 2.734816620
z7 2.344050187
x8 -2.188392019
y8 1.654074759
z8 2.524988378
x9 -3.264016048
y9 3.045193457
z9 2.193798612
x10 -1.790446556
y10 3.276290285
z10 3.194541593
END

BASIS

type TZ2P
core None
END

XC

GGA Becke Perdew
END

SYMMETRY NOSYM tol=0.001

SAVE TAPE21 TAPE13

EXCITATION

Davidson

```

lowest 20
END

SCF
iterations 50
converge 1.0e-6 1.0e-3
mixing 0.2
lshift 0.0
diis n=10 ok=0.5 cyc=5 cx=5.0 cxx=10.0
END

```

```

INTEGRATION 4.0 7 7

```

```

AlFIT 10.0

```

```

ModifyExcitations
  UseOccupied
  A 1
  SubEnd
End

```

```

eor

```

```

mkdir -p tapes
mv TAPE* tapes
mv logfile tapes

```

```

# =====
# DENSF
# =====

```

```

mv tapes/TAPE21 TAPE21
"$ADFBIN/densf" <<eor
Grid Coarse
Density fit trans
Potential coul trans
UNITS
  length Angstrom
  angle Degree
END

```

```

eor

```

```

mv TAPE* tapes
cat logfile >> tapes/logfile
rm -f logfile

```

A1.6 ADF input file for ground state and time-dependent DFT calculations of **1a**, p-toluene sulfonyl chloride.

```

"$ADFBIN/adf" <<eor
TITLE TosCL single point and sk

UNITS
  length Angstrom
  angle Degree

```

END

ATOMS

1 C x1 y1 z1
2 C x2 y2 z2
3 C x3 y3 z3
4 C x4 y4 z4
5 C x5 y5 z5
6 C x6 y6 z6
7 C x7 y7 z7
8 H x8 y8 z8
9 H x9 y9 z9
10 H x10 y10 z10
11 H x11 y11 z11
12 H x12 y12 z12
13 H x13 y13 z13
14 H x14 y14 z14
15 S x15 y15 z15
16 O x16 y16 z16
17 O x17 y17 z17
18 Cl x18 y18 z18
END

GEOVAR

x1 0.1141778918E-01
y1 0.2690993112E-01
z1 0.4771961314
x2 1.040237918
y2 0.8898401606
z2 0.8450727617
x3 1.022392460
y3 2.245161138
z3 0.4759391283
x4 -0.6220365915E-01
y4 2.719205769
z4 -0.2787173114
x5 -1.095097361
y5 1.870436110
z5 -0.6733444893
x6 -1.045910623
y6 0.5298535632
z6 -0.2850767436
x7 2.150115108
y7 3.167377753
z7 0.8648172890
x8 -0.1031918753
y8 3.771661991
z8 -0.5613356177
x9 -1.937014151
y9 2.236837923
z9 -1.256491308
x10 1.775365573
y10 4.157813289
z10 1.152487137
x11 2.731914682
y11 2.761188912
z11 1.700244921
x12 2.839207410
y12 3.313146034
z12 0.1942246661E-01

x13 1.870581833
y13 0.5053014545
z13 1.437374330
x14 0.2301057166E-01
y14 -1.019022097
z14 0.7796858473
x15 -2.394325646
y15 -0.5434618682
z15 -0.7173188957
x16 -3.414582372
y16 0.2173973014
z16 -1.405283391
x17 -2.702866410
y17 -1.411087197
z17 0.3984018889
x18 -1.503222788
y18 -1.793094903
z18 -2.168454350
END

BASIS
type TZ2P
core None
END

XC
GGA Becke Perdew
END

SYMMETRY NOSYM tol=0.001

SAVE TAPE21 TAPE13

EXCITATION
Davidson
lowest 40
END

QTENS

ESR
END
SCF
iterations 50
converge 1.0e-6 1.0e-3
mixing 0.2
lshift 0.0
diis n=10 ok=0.5 cyc=5 cx=5.0 cxx=10.0
END

INTEGRATION 4 7 7

AlFIT 10.0

ModifyExcitations
UseOccupied
A 2

SubEnd
End

A1.7 ADF input file for ground state and time-dependent DFT calculations on 2a, toluene sulfonic acid.

TITLE TosOH

UNITS
length Angstrom
angle Degree
END

ModifyExcitations
UseOccupied
A 1
SubEnd
End

ATOMS

1 C	0.061224810000	0.049058130000	0.471369870000
2 C	1.081284720000	0.923871870000	0.857320420000
3 C	1.037479710000	2.267291990000	0.472526260000
4 C	-0.046414630000	2.741469300000	-0.280452020000
5 C	-1.071099420000	1.866526730000	-0.668321440000
6 C	-1.023243530000	0.523363600000	-0.275673950000
7 C	2.190910880000	3.211706140000	0.873950130000
8 H	-0.093306460000	3.785070040000	-0.562655630000
9 H	-1.898206170000	2.228471400000	-1.264700250000
10 H	1.788561680000	4.170745050000	1.165946210000
11 H	2.729706760000	2.781108080000	1.707014720000
12 H	2.862575740000	3.339415560000	0.040980180000
13 H	1.903204030000	0.557946880000	1.454616190000
14 H	0.103904940000	-0.991976200000	0.751537950000
15 S	-2.339174880000	-0.631943340000	-0.736751500000
16 O	-3.596823160000	0.172111760000	-1.548604770000
17 O	-2.945342060000	-1.370258650000	0.670000590000
18 O	-1.686522570000	-1.821075810000	-1.758960180000
19 H	-2.371345840000	-2.445797750000	-2.010584760000

END

GUIBONDS

1	1	2	1.5
2	2	3	1.5
3	3	4	1.5
4	4	5	1.5
5	5	6	1.5
6	6	1	1.5
7	3	7	1.0
8	4	8	1.0
9	5	9	1.0
10	7	10	1.0
11	7	11	1.0
12	7	12	1.0
13	2	13	1.0
14	1	14	1.0
15	6	15	1.0

```

16 15 16 1.0
17 15 17 1.0
18 15 18 1.0
19 18 19 1.0
END

CHARGE 0

SYMMETRY NOSYM tol=0.001

BASIS
type TZ2P
core None
END

XC
GGA Becke Perdew
END

SAVE TAPE21 TAPE13

EXCITATION
Davidson
lowest 20
END

SCF
iterations 50
converge 1.0e-6 1.0e-3
mixing 0.2
lshift 0.0
diis n=10 ok=0.5 cyc=5 cx=5.0 cxx=10.0
END

INTEGRATION 4.0 7 7

AlFIT 10.0

```

A1.8 ADF input file for ground state and time-dependent DFT calculations on 3a, ethyl phenyl sulfone.

```

TITLE TOSET LT

UNITS
    length Angstrom
    angle Degree
END

ModifyExcitations
    UseOccupied
    A 1
    SubEnd
End

ATOMS ZMATRIX
1 C      0      0      0      0.000000000000      0.000000000000      0.000000000000
2 S      1      0      0      1.816278885140      0.000000000000      0.000000000000

```


3	C	2	1	0	1.803204634640	106.899856501000	0.000000000000
4	C	3	2	1	1.397354088510	124.006129744000	z4
5	C	3	2	4	1.400777567820	115.271556776000	180.131305356000
6	C	5	3	2	1.393574909180	119.412787694000	180.265759188000
7	C	6	5	3	1.398925676020	120.251289779000	359.676685818000
8	C	7	6	5	1.395128365020	119.986133910000	0.103609510658
9	H	5	3	2	1.088838482220	119.857998085000	0.038623816230
10	H	6	5	3	1.089368547890	119.580933997000	179.663108224000
11	H	7	6	5	1.089516467600	120.034098705000	180.049979527000
12	H	8	7	6	1.089224660170	120.255700276000	180.003485166000
13	H	4	3	2	1.088369531690	121.239580671000	0.304966833300
14	O	2	1	3	1.459896803570	108.344152765000	243.861518702000
15	O	2	1	14	1.460016297510	106.519271414000	230.512938086000
16	H	1	2	3	1.097665587900	106.785596764000	309.937580338000
17	H	1	2	16	1.099819709170	100.583213043000	248.295464965000
18	C	1	2	17	1.525074627330	115.165721573000	239.721362093000
19	H	18	1	2	1.096505050370	110.337319935000	54.089810678900
20	H	18	1	19	1.098590747870	109.571867685000	119.408268473000
21	H	18	1	20	1.097122054340	112.272659792000	120.160925607000

END

GUIBONDS

1 3 5 1.5
2 5 6 1.5
3 6 7 1.5
4 7 8 1.5
5 8 4 1.5
6 4 3 1.5
7 9 5 1.0
8 10 6 1.0
9 11 7 1.0
10 12 8 1.0
11 13 4 1.0
12 2 3 1.0
13 14 2 2.0
14 15 2 2.0
15 1 18 1.0
16 1 16 1.0
17 1 17 1.0
18 18 19 1.0
19 18 20 1.0
20 18 21 1.0
21 1 2 1.0

END

CHARGE 0.0

GEOVAR

z4 270 360
END

SYMMETRY NOSYM tol=0.001

BASIS

type TZ2P
core None
END

XC

GGA Becke Perdew
END

```

GEOMETRY
  lineartransit 7
  iterations 30
  optim All Internal
  step rad=0.15 angle=10.0
  hessupd BFGS
  converge e=1.0e-3 grad=1.0e-2 rad=1.0e-2 angle=0.5
END

SAVE  TAPE21 TAPE13

EXCITATION
Davidson
lowest 20
END

SCF
iterations 50
converge 1.0e-6 1.0e-3
mixing 0.2
lshift 0.0
diis n=10 ok=0.5 cyc=5 cx=5.0 cxx=10.0
END

INTEGRATION 4 7 7

A1FIT 10.0

```

A1.9 ADF input file for ground state and time-dependent DFT calculations on **1b, methane sulfonyl chloride.**

```

TITLE MESO2CL S-K edge

UNITS
  length Angstrom
  angle Degree
END

ATOMS
1 C x1 y1 z1
2 H x2 y2 z2
3 H x3 y3 z3
4 H x4 y4 z4
5 S x5 y5 z5
6 O x6 y6 z6
7 O x7 y7 z7
8 Cl x8 y8 z8
END

GEOVAR
x1 0.1262384994
y1 0.3387232576
z1 0.1027941566
x2 -0.5022336713E-01
y2 -0.7203779344
z2 -0.1223752814
x3 1.136879736
y3 0.6417103710

```

z3 -0.1854172113
x4 -0.6408014542
y4 0.9725787169
z4 -0.3512016347
x5 -0.1444290617E-01
y5 0.4759333329
z5 1.887679646
x6 1.092015671
y6 -0.2175129557
z6 2.505788982
x7 -1.384380827
y7 0.2318915910
z7 2.276125538
x8 0.3374298739
y8 2.534150464
z8 2.119821050
END

BASIS
type TZ2P
core None
END

XC
GGA Becke Perdew
END

SYMMETRY NOSYM tol=0.001

SAVE TAPE21 TAPE13

EXCITATION
Davidson
lowest 20
END

SCF
iterations 50
converge 1.0e-6 1.0e-3
mixing 0.2
lshift 0.0
diis n=10 ok=0.5 cyc=5 cx=5.0 cxx=10.0
END

INTEGRATION 4 7 7

AlFIT 10.0

ModifyExcitations
UseOccupied
A 2
SubEnd
End

A1.10 ADF input file for ground state and time-dependent DFT calculations on 2b, methane sulfonate.

TITLE MESO2oh S k-edge

ModifyExcitations

UseOccupied

A 1

SubEnd

End

UNITS

length Angstrom

angle Degree

END

ATOMS

1 C	0.003598347641	0.257529142080	0.031130043395
2 H	-0.107523086699	-0.831662249905	-0.022514917387
3 H	0.929680712750	0.578373563993	-0.456644480656
4 H	-0.871516986985	0.754746954421	-0.400080180944
5 S	0.084634418404	0.670027403716	1.770385545970
6 O	1.353420691120	0.224627580814	2.316662331780
7 O	-1.176559210820	0.317825950051	2.376036994920
8 O	0.138569281350	2.303618960260	1.690173254830
9 H	1.029709048170	2.562385026450	2.000187685390

END

GUIBONDS

1 1 2 1.0

2 1 3 1.0

3 1 4 1.0

4 1 5 1.0

5 5 6 2.0

6 5 7 2.0

7 5 8 1.0

8 8 9 1.0

END

CHARGE 0.0

SYMMETRY NOSYM tol=0.001

BASIS

type TZ2P

core None

END

XC

GGA Becke Perdew

END

SAVE TAPE21 TAPE13

EXCITATION

Davidson

lowest 20

END

```
SCF
iterations 50
converge 1.0e-6 1.0e-3
mixing 0.2
lshift 0.0
diis n=10 ok=0.5 cyc=5 cx=5.0 cxx=10.0
END
```

```
INTEGRATION 5 7 5
```

```
AlFIT 10.0
```

A1.11 ADF input file for ground state and time-dependent DFT calculations on model for **3b, dimethyl sulfone.**

```
TITLE MESO2ME
```

```
UNITS
    length Angstrom
    angle Degree
END
```

```
ATOMS
1 C x1 y1 z1
2 H x2 y2 z2
3 H x3 y3 z3
4 H x4 y4 z4
5 S x5 y5 z5
6 C x6 y6 z6
7 H x7 y7 z7
8 H x8 y8 z8
9 H x9 y9 z9
10 O x10 y10 z10
11 O x11 y11 z11
END
```

```
GEOVAR
x1 0.2044050125E-01
y1 -0.9974534674E-01
z1 0.1700119418E-01
x2 0.9474393788E-01
y2 -0.9907425984
z2 -0.6171230463
x3 0.2855590129
y3 -0.3163664456
z3 1.058590674
x4 -0.9905850021
y4 0.3205604226
z4 -0.3825563074E-01
x5 1.107101128
y5 1.186052739
z5 -0.6261950291
x6 2.747257732
y6 0.4456510507
z6 -0.5275515740
x7 3.428762148
y7 1.192506370
```

z7 -0.9527077002
x8 2.999641240
y8 0.2546875808
z8 0.5220608037
x9 2.770874092
y9 -0.4718597335
z9 -1.126793044
x10 1.067924023
y10 2.309656506
z10 0.3023560416
x11 0.7877457037
y11 1.372914110
z11 -2.036584888
END

BASIS
type TZ2P
core None
END

XC
GGA Becke Perdew
END

SYMMETRY NOSYM tol=0.001

SAVE TAPE21 TAPE13

EXCITATION
Davidson
lowest 20
END

SCF
iterations 50
converge 1.0e-6 1.0e-3
mixing 0.2
lshift 0.0
diis n=10 ok=0.5 cyc=5 cx=5.0 cxx=10.0
END

INTEGRATION 4 7 7

ALFIT 10.0

ModifyExcitations
UseOccupied
A 1
SubEnd
End

A1.12 Example of ADF input file for Δ SCF calculations on 1a, p-toluene sulfonyl chloride. The same parameters and geometry was used as for the TD-DFT simulated XAS spectra (A1.6 – A1.11).

TITLE TosCL single point and sk

UNITS

length Angstrom

angle Degree

END

Occupations

A 2 1.5 94 0.5 0 0 0 0 0 0 0 0 0 0

End

ATOMS ZMATRIX

1	Cl	0	0	0	0.000000000000	0.000000000000	0.000000000000
2	S	1	0	0	2.351742143770	0.000000000000	0.000000000000
3	C	2	1	0	1.789042803590	106.496853068000	0.000000000000
4	C	3	2	1	1.393041039510	118.557279801000	270.000000000000
5	C	4	3	2	1.394084742420	117.874299902000	178.725610588000
6	C	5	4	3	1.404468707820	121.352353616000	359.074761896000
7	C	6	5	4	1.405926490160	118.587827208000	0.374721592606
8	C	7	6	5	1.392476689840	121.377518051000	359.630027239000
9	C	6	5	4	1.507409500710	120.876021882000	181.516526858000
10	H	7	6	5	1.090577182850	119.608032709000	179.311819726000
11	H	8	7	6	1.087468068080	121.505638841000	179.485630372000
12	H	9	6	5	1.097114288210	111.392730897000	216.941805491000
13	H	9	6	12	1.096117323840	111.560459348000	121.386500522000
14	H	9	6	13	1.100510952110	110.467356737000	119.548767898000
15	H	5	4	3	1.090285259870	119.050343813000	178.717365091000
16	H	4	3	2	1.087382310450	120.544307863000	357.343771086000
17	O	2	1	3	1.456461412990	107.426265138000	114.941385738000
18	O	2	1	17	1.456298745440	107.675809576000	129.994024837000

END

GUIBONDS

1 4 5 1.5
 2 5 6 1.5
 3 6 7 1.5
 4 7 8 1.5
 5 8 3 1.5
 6 3 4 1.5
 7 6 9 1.0
 8 7 10 1.0
 9 8 11 1.0
 10 9 12 1.0
 11 9 13 1.0
 12 9 14 1.0
 13 5 15 1.0
 14 4 16 1.0
 15 3 2 1.0
 16 2 17 2.0
 17 2 18 2.0
 18 2 1 1.0
 END

CHARGE 0.0

SYMMETRY NOSYM tol=0.001

```

BASIS
type TZ2P
core None
END

XC
GGA Becke Perdew
END

SAVE TAPE21 TAPE13

SCF
iterations 50
converge 1.0e-6 1.0e-3
mixing 0.2
lshift 0.0
diis n=10 ok=0.5 cyc=5 cx=5.0 cxx=10.0
END

INTEGRATION 5 7 7

A1FIT 10.0

```

A1.13 Example of ADF input file for fragment analysis calculations on **1a**, p-toluene sulfonyl chloride. The same geometry was used as for the TD-DFT simulated XAS spectra (A1.6 – A1.11)

```

# dependency: /home/kennepohl/vlad/fatoscl2b.cl fatoscl2b.cl.t21
# dependency: /home/kennepohl/vlad/fatoscl2b.so2 fatoscl2b.so2.t21
# dependency: /home/kennepohl/vlad/fatoscl2b.tolu fatoscl2b.tolu.t21
#! /bin/sh

# =====
# The Molecule
# =====

"$ADFBIN/adf" <<eor

ModifyExcitations
  UseOccupied
  A 2
  SubEnd
End

TITLE TosCL single point and sk

UNITS
  length Angstrom
  angle Degree
END

ATOMS
1 C      -0.000530877574      0.051525045458      0.442496070463 f=tolu
2 C      1.028289251250      0.914455274938      0.810372700763 f=tolu

```


3 C	1.010443793250	2.269776252340	0.441239067363 f=tolu
4 C	-0.074152325904	2.743820883340	-0.313417372337 f=tolu
5 C	-1.107046027750	1.895051224340	-0.708044550237 f=tolu
6 C	-1.057859289750	0.554468677538	-0.319776804537 f=tolu
7 C	2.138166441250	3.191992867340	0.830117228063 f=tolu
8 H	-0.115140542054	3.796277105340	-0.596035678637 f=tolu
9 H	-1.937350825500	2.260164784870	-1.281690789420 f=tolu
10 H	1.763416906250	4.182428403340	1.117787076060 f=tolu
11 H	2.719966015250	2.785804026340	1.665544860060 f=tolu
12 H	2.827258743250	3.337761148340	-0.015277594327 f=tolu
13 H	1.858633166250	0.529916568838	1.402674269060 f=tolu
14 H	0.011061904906	-0.994406982662	0.744985786363 f=tolu
15 S	-2.435499990920	-0.570881729301	-0.675445186853 f=so2
16 O	-3.492687950070	0.179634794787	-1.317476475650 f=so2
17 O	-2.693599655520	-1.481187979180	0.418872444354 f=so2
18 Cl	-1.480078122500	-1.789108297530	-2.181365072020 f=cl

END

GUIBONDS

1 1 2 1.5
2 2 3 1.5
3 3 4 1.5
4 4 5 1.5
5 5 6 1.5
6 6 1 1.5
7 3 7 1.0
8 4 8 1.0
9 5 9 1.0
10 7 10 1.0
11 7 11 1.0
12 7 12 1.0
13 2 13 1.0
14 1 14 1.0
15 6 15 1.0
16 15 16 2.0
17 15 17 2.0
18 15 18 1.0
END

CHARGE 0.0

SYMMETRY NOSYM tol=0.001

BASIS

type TZ2P
core None
END

XC

GGA Becke Perdew
END

Fragments

cl fatoscl2b.cl.t21
so2 fatoscl2b.so2.t21
tolu fatoscl2b.tolu.t21
end
SAVE TAPE21 TAPE13

SCF

```

iterations 50
converge 1.0e-6 1.0e-3
mixing 0.2
lshift 0.0
diis n=10 ok=0.5 cyc=5 cx=5.0 cxx=10.0
END

```

```

INTEGRATION 4.0 4.0 4.0

```

```

AlFIT 10.0

```

```

eor

```

A1.14 ADF input file for linear transit calculation of 1a, p-toluene sulfonyl chloride.

```

TITLE TosCL single point and sk
UNITS
    length Angstrom
    angle Degree
END

```

```

ModifyExcitations
    UseOccupied
    A 2
    SubEnd
End

```

```

ATOMS ZMATRIX
1 Cl    0    0    0    0.000000000000    0.000000000000    0.000000000000
2 S     1    0    0    2.112212378510    0.000000000000    0.000000000000
3 C     2    1    0    1.776812417670    101.791283537000    0.000000000000
4 C     3    2    1    1.397124047540    119.314039695000    0.000000000000
5 C     4    3    2    1.392283251910    118.703047905000    182.041504214000
6 C     5    4    3    1.404803563300    121.275067833000    0.642281384535
7 C     6    5    4    1.403771133710    118.481451871000    359.979719236000
8 C     7    6    5    1.393918915470    121.271228463000    359.183344159000
9 C     6    5    4    1.507802400740    120.851499036000    180.770071385000
10 H    7    6    5    1.090512375050    119.621769687000    178.992673533000
11 H    8    7    6    1.087719808600    121.346627364000    179.882358502000
12 H    9    6    5    1.097339376130    111.360452967000    219.215075202000
13 H    9    6    12    1.096092809560    111.525362136000    121.260757225000
14 H    9    6    13    1.100358577080    110.564242778000    119.670736484000
15 H    5    4    3    1.090028523240    119.197779723000    180.173793042000
16 H    4    3    2    1.088856385520    120.359365501000    1.708737756580
17 O    2    1    3    1.446763840340    106.376924592000    114.588104452000
18 O    2    1    17    1.446652682370    105.367852768000    130.961738470000
END

```

```

GUIBONDS
1 4 5 1.5
2 5 6 1.5
3 6 7 1.5
4 7 8 1.5
5 8 3 1.5
6 3 4 1.5
7 6 9 1.0
8 7 10 1.0
9 8 11 1.0
10 9 12 1.0
11 9 13 1.0

```

12 9 14 1.0
13 5 15 1.0
14 4 16 1.0
15 3 2 1.0
16 2 17 2.0
17 2 18 2.0
18 2 1 1.0
END

CHARGE 0.0

GEOVAR
z4 270 360
END

SYMMETRY NOSYM tol=0.001

BASIS
type TZ2P
core None
END

XC
GGA Becke Perdew
END

GEOMETRY
smooth conservepoints
lineartransit 7
iterations 30
optim All Internal
step rad=0.15 angle=10.0
hessupd BFGS
converge e=1.0e-3 grad=1.0e-2 rad=1.0e-2 angle=0.5
END

SAVE TAPE21 TAPE13

EXCITATION
Davidson
lowest 20
END

SCF
iterations 50
converge 1.0e-6 1.0e-3
mixing 0.2
lshift 0.0
diis n=10 ok=0.5 cyc=5 cx=5.0 cxx=10.0
END

INTEGRATION 3.0 7 7
AlFIT 10.0